Hybrid quadrupole excitons and polaritons in cuprous oxide

by

Oleksiy Roslyak

A dissertation submitted to the Graduate Faculty in Physics in partial fulfillment of the requirements for the degree of Doctor of Philosophy, The City University of New York.

2007

This manuscript has been read and accepted for the Graduate Faculty in Physics in satisfaction of the dissertation requirements for the degree of Doctor of Philosophy.

Prof. Joseph L. Birman

Date

Chair of Examining Committee

Prof. Catto Sultan

Date

Executive Officer

Prof. Ramzi Khuri

Prof. Jonathan Huntley

Prof. David Lieberman

Prof. Catto Sultan

Supervisory Committee

THE CITY UNIVERSITY OF NEW YORK

Abstract

Hybrid quadrupole excitons and polaritons in cuprous oxide

by

Oleksiy Roslyak

Advisor: Prof. Joseph L. Birman

In this thesis I consider novel type of materials such as hybrid organic/inorganic heteoro-structures and polystyrene micro-spheres/inorganic composites. The organic/inorganic compound is presented by DCM2:CA:PS / cuprous oxide material. Using "solid state solvent" mechanism I propose to bring the Frenkel exciton (FE) of the DCM2 into resonance with $1S$ quadrupole Wanier-Mott exciton (WE) in cuprous oxide. This two types of the excitons form new type of *quadrupole-dipole hybrid* exciton. This hybrid is characterized by long lifetime and big oscillator strength inherited from the organic FE. In the part I of the thesis I investigate the enhancement of the quadrupole properties generic to cuprous oxide exciton by means of such resonant hybridization. I consider enhancement of photo-thermal bi-stability and second harmonic generation. The second part is devoted to the problems

of light-matter interaction in cuprous oxide crystals such as weak interaction with LA phonons and whispering gallery modes (WGM) in adjacent layer of polystyrene micro-spheres. While the first effect is likely to impeded BEC of the polaritons, the second mechanism provides necessary temporal coherence. It is possible by trapping the light part of the polariton into resonant WGM through big gradient of the evanescent tail which provides big lifetime of such *evanescent polariton*. Due to big gradient of the evanescent field it couples "naturally" to the quadrupole WE in cuprous oxide.

Acknowledgments

I would like to acknowledge Ms. Upali Aparajita for useful comments and discussion on the manuscript. I also would like to thank Prof. Lev Deych for the work presented in the last chapter. This project was supported in part by PCS-CUNY.

Preface

Nanometer-sized organic and inorganic semiconductor structures have recently been attracting much attention. In these low-dimensional systems, there are pronounced quantum confinement effects on the electronic and optical properties. Synthesizing composite organic/inorganic semiconductors is of major importance not only in the development of novel nano-structure materials for electronics, optics and transport applications, as well as biomedical; but also for basic understanding of their size-dependent physical properties. Recently, a new type of elementary state which can be generated by optical excitation was introduced by Agranovich [1]. This is a hybrid exciton which can be obtained from the resonant mixing of Frenkel(FE) and Wannier-Mott(WE) excitons in organic-inorganic quantum wells by means of dipole-dipole interaction across the interface. Many properties of this hybrid were predicted. Other realizations for the hybrid have been proposed. Examples are hybrid excitons in an inorganic semi-conducting quantum dot

covered by an organic layer[2] and the quantum dot-dendrimer system [3]. The energy of the hybrid exciton as well as the Green's function matrix elements for different quantum dot-dendrimer systems has been calculated.

In the model of Agranovich et. al. the decisive role in implementing the formation of the hybrid state is played by the dipole-dipole coupling between the semiconductor WE and organic FE. It is assumed that there is no direct wave function overlap between the excitons on each side of the well. The interaction energy takes the form of $P(\mathbf{r}) \cdot E(\mathbf{r})$ where $P(\mathbf{r})$ is the polarization field due to the organic dipoles of the FE interacting with the electric field $E(\mathbf{r})$ in the semiconductor from WE. In the work reported here I modified this model to consider the quadrupole exciton "yellow" $1S$ level in cuprous oxide. This immediately puts my attention on a different interaction term, which is now $\vec{\vec{Q}} \cdot \nabla \vec{E} = Q_{i,j} \frac{\partial}{\partial x_i} E_{j,\mathbf{k}}$. Here the quadrupole field couples to a spatially varying (or $\mathbf{k}$ dependent) electric field. This coupling is the basis of the present work.

In Chapter 1 of this thesis I discuss resonant hybridization of the $1S$ quadrupole WE in a Cu_2O quantum well with the dipole FE in an adjacent layer of organic DCM2:CA:PA. The coupling between excitons is due to interaction between the gradient of the electric field induced by DCM2 FE and the quadrupole moment of the $1S$ transition in the cuprous oxide.

The specific choice of the organic allows use of the mechanism of "solid state solvation" (See work of Bulovic [4] for more details) to dynamically tune the WE and FE into resonance during a time $\approx 3.3\ ns$ (comparable with the big life time of the WE) of the "slow" phase of the solvation. The quadrupole-dipole hybrid utilizes the big oscillator strength of the FE along with the big lifetime of the dipole forbidden quadrupole exciton, unlike dipole-dipole hybrid exciton which utilizes the big oscillator strength of the FE and big radius of the dipole allowed WE. Due to strong spatial dispersion and big mass of the quadrupole WE the hybridization is not masked by the kinetic energy or the radiative broadening of the exciton. The lower branch of the hybrid dispersion exhibits a pronounced minimum and may be used in applications. Also I investigate and report noticeable change in the coupling due to a induced "Stark effect" from the strong local electric field of the FE. I investigate the quadrupole exciton energy fine structure of the quantum well confined ortho and para-excitons in cuprous oxide.

In Chapter 2 I demonstrated formation of multiple bi-stability regions in the temperature pattern on the interface between cuprous oxide quantum well and DCM2:CA:PS organic compound. The quadrupole-dipole hybrid excitons are thermalized with the surrounding helium. This leads to higher non-linear temperature dependence on the laser field detuning from

the quadrupole exciton energy band which is associated with the temperature induced red shift of the WE energy. Numerical up and down laser frequency scan around $1S$ quadrupole resonance reveals hysteresis-like temperature distribution. The multiple bi-stability regions are at least three orders of magnitude bigger (meV) then experimentally observed bi-stability in the bulk cuprous oxide (μeV) without the hybridization. The effective absorption shape exhibits high asymmetrical behavior for the Frenkel-like [1] and Wannier-like [2] branches of the hybrid.

In Chapter 3 I report substantial enhancement of the optical second harmonic generation (SHG) generic to the cuprous oxide crystals by resonant hybridization with appropriate organic material (DCM2:CA:PS "solid-state solvent"). The quadrupole origin of the inorganic part of the quadrupole-dipole hybrid provides inversion symmetry breaking and the organic part contributes to the oscillator strength of the hybrid. I show that the enhancement of the SHG, compared to the bulk cuprous oxide crystal, is proportional to the ratio of the DCM2 dipole moment and the effective dipole moment of the quadrupole transitions in the cuprous oxide. It is also inversely proportional to the line-width of the hybrid and bulk excitons. The enhancement

[1] for the frequencies *below* the resonance
[2] for the frequencies *above* the resonance

may be regulated by "concentration tuning" of the organic blend (mutual concentration of the DCM2 and CA part of the solvent) and choosing appropriate pumping conditions [3].

In Chapter 4 I present a comparative analysis of a "conventional" phonoriton [4] and a polariton [5] "weakly" coupled to the LA-phonons bath. Depending on the duration of the pumping laser field, the phonon-induced decoherence results in two distinct types of excitation. Long (ms) laser pumping pulses form an "equilibrium" polariton. The generic feature here is a pronounced photo-thermal bi-stability. i.e. formation of four distinct branches. Transitions between branches can be achieved by excitation energy fluctuations as small as 200 neV. It is suggested that this may impede BEC of the para-excitons. Short (μs) laser pulses create a "quasi-equilibrium" polariton. In the latter case, for some critical intensity of the laser field I demonstrate possibility of strong luminicence from a highly unstable localized state on the lower polariton branch.

In Chapter 5 I demonstrate formation of a new type of polariton on the interface between a cuprous oxide slab and a polystyrene micro-sphere placed on the slab. The evanescent field of the resonant whispering gallery mode

[3] varying the angle of incidence in case of optical pumping or populating the minimum of the lower branch of the hybrid in case of electrical pumping

[4] coherent superposition of exciton-photon-phonon

[5] coherent exciton-photon superposition

(WGM) has a substantial spacial gradient, and therefore effectively couples with the quadrupole $1S$ excitons in cuprous oxide. This "evanescent" polariton has long life-time ($1.7ns$), which is determined only by its excitonic component. The polariton lower branch has well pronounced minimum. Hence it is suggested here that this can be readily utilized for BEC. The spatial coherence of the polariton can be improved by assembling the micro-spheres into a linear chain.

Therefore in Chapter 7 I consider the one-dimensional chain of identical spheres optically coupled by means of their WGM overlap. The band structure of these new excitations depends significantly on the type of modes involved in the inter-mixing between nearby spheres. I develop a general theory of the photonic band structure of these excitations taking these effects into account. This is applied to several cases of recent experimental interest. In the case of bands originating from WQMs with angular quantum number of the same parity, the calculated dispersion laws are in good qualitative agreement with recent experiment results. Bands resulting from hybridization of excitations resulting from whispering gallery modes with different parity of their angular momentum exhibits anomalous dispersion properties characterized by a gap in the allowed values of the size parameter and divergence of the group velocity.

In the last Chapter 6 some unsolved problems are presented. These can be directions for the future work on the QDH and "evanescent" polariton.

Contents

List of Figures

Part I

Excitons

Chapter 1

Hybrid quadrupole-dipole exciton

In the following section 1.1 I will generalize the Agranovich-Bassani work [6] on dipole-dipole hybrid excitons, formed in adjacent layers of organic-inorganic hetero-structures. The system I will analyze in this paper makes use of the dipole forbidden, quadrupole allowed $1S$ exciton in Cu_2O (WE) coupled to a suitable organic Frenkel exciton (FE). Due to the strong spatial dispersion of the quadrupole transitions I anticipate strong wave vector and polarization dependence of the dispersion for the hybrid. Concrete results will be given below for realistic configuration and values of parameters for particular organic materials.

Note that while there has been experimental work on bulk cuprous oxide , very little experimental and theoretical work (or none) has been reported on films or heterojunctions. In the remainder of this thesis experimental values

of the parameters will be taken from established results on bulk systems. In a few cases it is modified for lower dimensions as noted. Therefore in section 1.2 I present theoretical examination of confinement effects which are essential due to the rather small Bohr radius of $1S$ exciton; especially the "central cell" and local field effects on the exciton dispersion.

In section 1.3 I discuss the problem of the choice of some proper organic materials to assure resonance between FE and WE in the quantum wells. We are going to show that layers of PS:CA:DCM2 [4] give an excellent match to the quadrupole "yellow" $1S$ exciton of cuprous oxide. I have chosen this organic compound due to three main factors:

1. the extremely big oscillator strength of the organic FE formed on DCM2 molecules;

2. unlike the conventional organic materials [1] with short emission lifetime, the dynamic "solid state solvation" mechanism discovered in such a compound by Bulovici et. al. [7]. It would allow the hybrid to live through the phase of "slow" solvation ($\approx 3\,ns$). This is comparable to the lifetime of the quadrupole exciton;

3. the ability to tune into resonance the energy of the singlet FE simply

[1] such as tetracene, antracene and some other

by means of changing concentration of the CA.

The strong local electric field induced by the organic FE penetrates into the cuprous oxide layer and results in an induced "confined Stark effect". The relative shift of the electron and hole gives rise to induced polarization and thus reduces the hybridization effect. This will be discussed in detail in section 1.4 of this chapter.

Hybridization requires coupling between the two excitons, and I will estimate the coupling coefficient in section 1.5. The coupling between FE and WE in the case of quadrupole active $1S$ WE is due to *gradient* of the field induced by the FE in the DCM2 organic. In the dipole-dipole hybrid exciton previously analysed one utilizes big oscillator strength of the FE and big Bohr radius of the WE. In contrast, in case of *quadrupole-dipole* exciton one utilizes the *big oscillator strength* of the FE and *long life time* of the WE along with enhanced spatial dispersion of the coupling parameter.

In the final section 1.6 I will discuss the specifics of the quadrupole-dipole hybridization dispersion and briefly propose possible experimental evidences of such a hybridization. I look forward to experimental tests of our results, by means of new types of high precision spectroscopy which were invented recently [8].

1.1 The QDH exciton configuration

A proposed configuration of an experiment for obtaining the hybrid exciton is shown in the following diagram (see Fig. 1.1). In this simplified model a mono-layer of width $L_w \approx$ size of a unit cell 4.6 $\mathring{A}$ quantum well of Cu_2O (gap energy $E_g = 2.17\ eV$ [8]) is placed upon a thin film of the PS:CA:DCM2 organic (with the gap energy much bigger than that of the cuprous oxide). Obliquely incident [2] photons excite WE in the cuprous oxide and the FE in DCM2. I consider DCM2 exciton as a 2D lattice of dipoles $\mu_x = 20\ D$ [3] at discrete sites $\mathbf{n}$, placed at $z' \approx L_w/2$.

I treat the interaction of cuprous oxide quadrupole excitations only with DCM2 organic molecules in the quadrupole approximation, since at the pumping laser frequency only dipole forbidden transitions are allowed. Due to the small concentration of the DCM2 molecules there is a "buffer" of PS between Cu_2O and DCM2 so that one may neglect the exciton-exciton wave function overlap and assume perfect 2D invariance of the system in direction transverse to growth. Further on I neglect the kinetic energy of the WE. Indeed, as will be shown in detail in the next paragraph, due to fluctuations of the inorganic quantum well (IQW) width, strong confinement of the exciton

[2] to assure x component of the exciton wave vector
[3] D stands for Debye

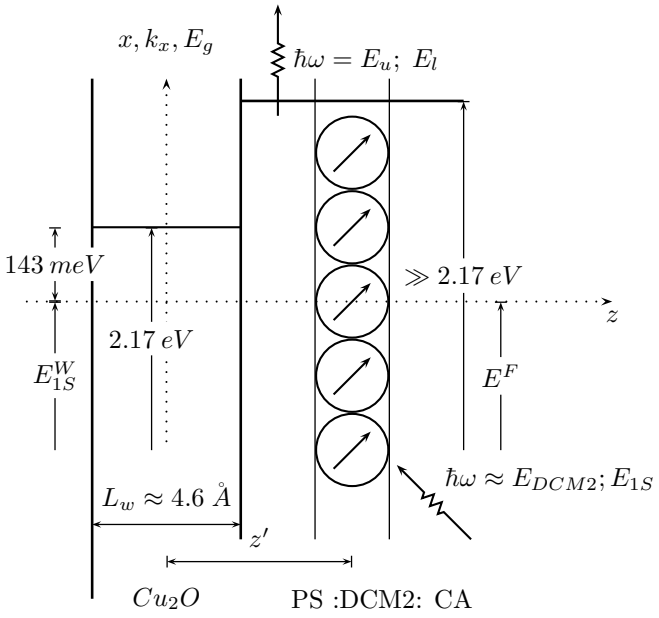

Figure 1.1: Schematic representation of a possible experimental set-up to produce quadrupole-dipole excitons. Here the inorganic Cu_2O quantum well provides the $1S$ quadrupole WE with the binding energy 143 meV (for details see section 1.2). Two pumping photons $\hbar\omega \approx E_{DCM2}, E_{1S}$ generate the hybrid signal from the upper E_u and lower E_l branches. The DCM2 part of the organic "solid state solute" provides dipole allowed FE; the PS host prevents wave function overlapping between organic and inorganic excitons; CA under proper concentration allows tuning of the excitons into the resonance. Due to comparable lifetimes of both types of exciton the system utilizes strong spacial dispersion of the quadrupole exciton and big oscillator strength of the organic.

occurs [4] compared to the kinetic energy for small wave vectors. This results in hopping motion of the exciton between sites of localization.

I seek new quadrupole-dipole hybrid (QDH) eigenstates for the upper (u) and lower (l) branches in the usual linear combination form:

$$|u,\mathbf{k}\rangle = A_u\,|F,\mathbf{k}\rangle + B_u\,|W,\mathbf{k}\rangle\,,\ |l,\mathbf{k}\rangle = A_l\,|F,\mathbf{k}\rangle + B_l\,|W,\mathbf{k}\rangle$$

Here the weighting coefficients for small $\mathbf{k}$ are given by [1]: $A_{u,l}^2 = B_{u,l}^2 = 1/2$.

After the usual diagonalization of the coupled WE/FE Hamiltonian, $H = H_{WE} + H_{FE} + H_{int}$, the energies of the resulting upper and lower branches are given by:

$$E_{u,l} = E^{W(F)} \pm \Gamma_{\mathbf{k}}$$

Here I have introduced the quadrupole-dipole interaction Hamiltonian and corresponding off-diagonal hybridization coupling parameter:

$$\Gamma\left(\mathbf{k}\right) \equiv \left|\langle W,\mathbf{k}|\,\hat{H}_{int}\,|F,\mathbf{k}\rangle\right|$$

In the subsequent sections I will derive expressions for the energies of the exciton and the necessary conditions for the resonance hybridization. Also as a main result of the chapter I will derive an analytical expression for the

[4] Let us consider smallest possible fluctuation of the IQW width, i.e. it changes from L_w to $2L_w$ and decrease of the exciton energy is approximately 20 meV which is big comparing to the rather small kinetic energy of the exciton for it has rather big mass of free exciton

hybridization parameter and dispersion. This will be followed by quantitative and qualitative comparison of systems with conventional dipole-dipole hybridization [1].

1.2 Quasi 2-D exciton in cuprous oxide

As far as I am aware there is no experimental data or theoretical description for cuprous oxide film systems; contrary to the extensive literature for the bulk case. Because of the small size Cu_2O quadrupole exciton one can not consider a strong confinement effect, which requires the width of the IQW much less than the Bohr radius of the exciton a_b. Even if modern epitaxy methods allows one to manufacture a molecular mono-layer for the quantum well thickness, one would have $L_w/a_b \approx 1/2$ which is not enough for consideration of pure 2D WE. Two and more mono layers in one quantum well will give the case of weak confinement and result in much weaker coupling (see below). Thus I start from the well described case of bulk "yellow" exciton and then theoretically estimate the main properties in case of strong confinement.

Cuprous oxide condenses in a cubic structure, where the copper ions form a face-centered sub lattice, while the oxygen ions form a body-centered sub lattice. The arrangement of both sub lattices is such that a copper ion is

found centered between two neighboring oxygen ions (O_h symmetry) with the lattice constant $a \approx 4.26$ $\mathring{A}$. From the lattice structure I now turn to the band structure of this crystal [9]. There is a direct band gap, where the valence band is formed by the Cu $3d$ orbitals and the conduction band arises from Cu $4s$ and (possible) oxygen orbitals. In the presence of the cubic crystal field, the five $3d$ states of the valence band split further into three states of type ${}^3\Gamma_5^+$ and a twofold ${}^2\Gamma_3^+$ level. Taking also spin-orbit interaction into account, the state splits further into a twofold level ${}^2\Gamma_7^+$ and a fourfold degenerate ${}^4\Gamma_8^+$ level. The exciton representation is obtained from the direct product of electron and hole $\Gamma_{ex} = \Gamma_{envelop} \otimes \Gamma_e \otimes \Gamma_h$.

For S-excitons : ${}^1\Gamma_1^+ \otimes {}^2\Gamma_7^+ \otimes \Gamma_6^+ = {}^3\Gamma_5^+ + {}^1\Gamma_2^+$. The threefold degenerate ${}^3\Gamma_5^+$ state and single ${}^1\Gamma_2^+$ state are termed ortho-exciton and para-exciton respectively. The para-exciton is optically forbidden in bulk. The ortho-exciton is dipole $\left({}^3\Gamma_4^-\right)$ forbidden from the ground state of symmetry $\left({}^1\Gamma_1^+\right)$, because $\left\langle {}^1\Gamma_1^+ \middle| {}^3\Gamma_4^- \middle| {}^3\Gamma_5^+ \right\rangle = 0$ and couples to the light in lowest order via quadruple interaction of symmetry $\left({}^3\Gamma_5^+\right)$, $\left\langle {}^1\Gamma_1^+ \middle| {}^3\Gamma_5^+ \middle| {}^3\Gamma_5^+ \right\rangle \neq 0$.

Unlike the dipole operator, the quadrupole operator depends on the direction of the light wave vector $\mathbf{k}$ relative to the lattice and the radiation polarization vector $\mathbf{e}$. Because of the $\mathbf{k}$ dependence the transition is anisotropic even in a cubic crystal. The amplitudes of the ortho-exciton

quadruple transitions are given by the symmetric vector product of $\mathbf{k}$ and $\mathbf{e}$: $\sim \mathbf{e}_i\mathbf{k}_j + \mathbf{e}_j\mathbf{k}_i,\ i \neq j$, see for example [9]. The three components correspond to the Cartesian representations: ${}^3\Gamma^+_{5xz}, {}^3\Gamma^+_{5yz}, {}^3\Gamma^+_{5xy}$.

The measured [10] oscillator strength of the quadrupole transition in bulk Cu_2O is low $f_{[110]} \simeq 3.9{\cdot}10^{-9}$, which is about four orders of magnitude smaller than the value found for the dipole alowed transitions of the P-excitons of the same "yellow" series. Even though the coupling to the light is extremely weak, it can not be disregarded. The binding energy is about 153 meV and Bohr radius of the exciton is given by $a_b = 2\pi\varepsilon_0/E_b \approx 7\ \mathring{A}$.

Because of the unidirectional confinement in the IQW, the exciton is discretized in this direction (z-direction). And so the symmetry group O_h is reduced to D_{4h}. As a result the three fold degenerate ortho-exciton ${}^3\Gamma^+_5$ is split into two fold degenerate ${}^2\Gamma^+_5$ and non degenerate ${}^1\Gamma^+_4$ ortho-exciton levels, which I am going to refer to as "heavy" and "light hole exciton" in analogy with the well known case of dipole allowed exciton. Another remarkable result of the confinement is that the para-exciton ${}^1\Gamma^+_2$ changes its symmetry to ${}^1\Gamma^+_3$. And due to the fact that the quadrupole operator ${}^3\Gamma^+_5$ also reduces its symmetry to ${}^2\Gamma^+_5$ and ${}^1\Gamma^+_3$ the para-exciton is no longer forbidden in the IQW. Note that roughness of the interface due to the small width of the IQW leads to further reduction of the symmetry to D_{2h}. The details of

the selection rules and dependence upon polarization can be found in the Table 1.1, 1.2 (See Appendix).

Now let us consider the effect of confinement on the energy spectrum of the quadrupole active exciton. I study only the ortho-exciton (the generalization to the case of para-exciton is trivial) and neglect spin-dependent exchange interaction and related spin-orbit effects. The energy of the $1S$ quadrupole exciton confined in a IQW can be written as:

$$H_{WE} = H_e(z_e) + H_h(z_h) + \frac{p^2}{2\tilde{\mu}} + \frac{P^2}{2M} - \frac{e^2}{\varepsilon\sqrt{\rho^2 + (z_e - z_h)^2}}$$

Here ρ is the relative electron e - hole h position, p is the relative momentum, P is center of mass quasi momentum which is to be considered in $x, y-$ plane. $\tilde{\mu}$ and M are reduced mass and total mass of the exciton respectively.

The quadrupole exciton confined in the infinite IQW has a smaller Bohr radius than in case of bulk and as a result one must take into account so called "central cell" corrections (CCC) [11] in determining the dispersion [5] (See Fig.1.2).

Aside from the non-parabolicity of the bands [12], the electron-hole interaction in this case is the bare Coulomb interaction modified by the **k** dependent dielectric function. This is mainly due to virtual LO-phonon as-

[5] wave vector dependence of the hybrid exciton energy

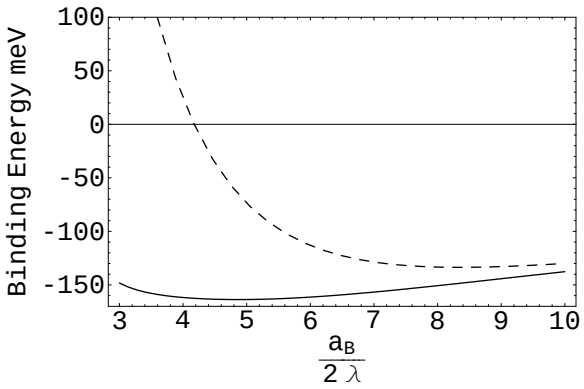

Figure 1.2: The solid line shows the modified energy of the $1S$ exciton as a function of the Bohr radius ($\mathring{A}$) and variational parameter λ due to the confinement effect; the dotted line shows the same function with the central cell correction not taken into account.

sisted valence electron transition into the highest conduction bands (${}^4\Gamma_8^-$ split by the confinement). Here I have to assume that the energy of the LO-phonon modes exceeds 87 meV [13], when the dielectric constant drops from $\varepsilon_0 = 7.5 \mp 0.2$ to $\varepsilon_\infty = 6.46$. In this case it can be shown [11] that for small values of the exciton wave number k, $\varepsilon(k) \approx \varepsilon_\infty - 0.18\,(ka)^2$.

In my model due to the comparable sizes of the exciton radius and IQW width, one can consider the confinement as a small perturbation upon the pure 2D exciton energy. To explicitly show the perturbation part it is convenient to introduce a small variational parameter λ ranging from 1 for pure 2D to 1/2 for pure bulk cases, so that the confined exciton energy can be

re-written as:

$$H_{WE} = H^0_{WE} + H^1_{WE} + H^2_{WE} \tag{1.1}$$

Here I separated the analytically solvable part:

$$H^0_{WE} = H_e\left(z_e\right) + H_h\left(z_h\right) + \frac{p^2}{2\tilde{\mu}} + \frac{P^2}{2M} - \frac{\lambda e^2}{\varepsilon\rho} \tag{1.2}$$

and small perturbation parts which are due to the weak confinement:

$$H^1_{WE} = \frac{\lambda e^2}{\varepsilon\rho} - \frac{e^2}{\varepsilon\sqrt{\rho^2 + \left(z_e - z_h\right)^2}} \tag{1.3}$$

$$H^2_{WE} = \frac{p^4 a^2}{24\hbar^2\mu'} - \frac{p^2 P^2 a^2}{4\hbar^2 M'} \tag{1.4}$$

These terms (1.3, 1.4) come from second order corrections in the tight-binding model and are due to non-parabolicity of the bands with $1/\mu' = C_e/m_e + C_h/m_h$ and $M' = m_e/C_e + m_h/C_h$. The second term in (1.4) couples the relative motion of the electron and hole with the motion of their center of mass and modifies the total exciton mass. The fourth term in (1.2) and second term in (1.2) yields the free exciton dispersion relation for the center of mass motion [11]:

$$E_{\mathbf{k}} = \frac{\hbar^2 k^2}{2M}\left(1 - \frac{2\lambda^2 M a^2}{M' a_b^2}\frac{I_4\left(\frac{k_D a_b}{2\lambda}\right)}{I_2\left(\frac{k_D a_b}{2\lambda}\right)}\right) \tag{1.5}$$

Here k_D is the Debye wave vector, i.e. the radius of a sphere with volume equal to that of the first Brillouin zone and $I_n\left(x\right) = \int\limits_0^x \frac{y^n dy}{\left(1+y^2\right)^4}$. Kouvalkis

et. al.[11] estimated the order of magnitude of the constants C_e, C_h using $\mathbf{k}\cdot\mathbf{p}$ perturbation theory. Mixing of bands with different parities modifies the bare electron and hole masses. In addition including the coupling to LO modes gives $C_e \approx C_h \approx 1$.

In my work I am going to use a simplified approach instead of the $\mathbf{k}\cdot\mathbf{p}$ perturbation theory and estimate this correction from the fact that the exciton becomes localized as the Bohr radius approaches the lattice constant: $\lim_{a_b\to a} E_{\mathbf{k}} = 0$. This yields the following expression $C = 2I_2(\pi)/I_4(\pi)$. The correction to the potential energy due to the first term in (1.4) is given by its expectation value in momentum space.

$$-\frac{\hbar^2 a^2}{24\mu'}\left(\sum_{q<k_D}|\Psi_{\mathbf{q}}|^2 q^4\right)\left(\sum_{q<k_D}|\Psi_{\mathbf{q}}|^2\right)^{-1} = -\frac{\hbar^2 a^2 C}{24\mu}\frac{I_6\left(\frac{k_D a_b}{2\lambda}\right)}{I_2\left(\frac{k_D a_b}{2\lambda}\right)}$$

Here the relative electron e - hole h motion wave function $\Psi_{\mathbf{q}} = \frac{8\sqrt{\pi a_b^2}}{\left(1+(qa_b)^2\right)^2}$ is strongly peaked in momentum space. The last term in H^0_{WE} describes the effective interaction between an electron and hole at momentum transfer q with the same approximation for the $\mathbf{k}$ dependent dielectric function as above:

$$V(q) = \frac{4\pi e^2}{q^2\varepsilon(q)} \approx \frac{4\pi e^2}{q^2\varepsilon_\infty} + \frac{4\pi e^2}{\varepsilon_\infty}a^2\cdot 0.18.$$

If one truncates the $1S$ trial wave function outside the first Brillouin zone I

find the correction due to the small Bohr radius of the exciton in the form:

$$-\frac{0.36\lambda^3 e^2 a^2}{\pi\varepsilon_\infty^2 a_b^3}\frac{\left[I_2'\left(\frac{k_D a_b}{2\lambda}\right)\right]^2}{I_2\left(\frac{k_D a_b}{2\lambda}\right)}$$

In the above expression the contribution of LO phonons to the dielectric function has been employed, where the main contribution comes from virtual transitions between the higher Γ_8^- conduction band and the highest Γ_7^+ valence band. Now treating H_{WE}^1 as perturbation in the lowest order and neglecting momentum dependence of the screening and approximating $H_e(z_e)+H_h(z_h)+\frac{P^2}{2M}$ by $\frac{\hbar^2\lambda^2}{\tilde{\mu}a_b^2}$ one can find the total WE energy in the IQW as the minimum of the total exciton energy with respect to the Bohr radius:

$$\begin{aligned} E_{WE}^{total}(\lambda, a_b) = \frac{\hbar^2\lambda^2}{\tilde{\mu}a_b^2} - \frac{2\lambda e^2}{\varepsilon_\infty a_b} - \\ -\frac{\hbar^2 a^2 C}{24\mu}\frac{I_6\left(\frac{k_D a_b}{2\lambda}\right)}{I_2\left(\frac{k_D a_b}{2\lambda}\right)} - \frac{0.36\lambda^3 e^2 a^2}{\pi\varepsilon_\infty^2 a_b^3}\frac{\left[I_2'\left(\frac{k_D a_b}{2\lambda}\right)\right]^2}{I_2\left(\frac{k_D a_b}{2\lambda}\right)} \end{aligned} \tag{1.6}$$

To find the variational parameter λ we use an additional restriction determined by requiring that the first order energy shift vanishes [14]:

$$\langle\Psi_\lambda| H_{WE}^1 |\Psi_\lambda\rangle = 0 \tag{1.7}$$

$$\Psi_\lambda = \chi_e(z)\chi_h(z)\frac{(2\lambda)^{3/2}\exp(-\frac{2\lambda\rho}{a_b})}{\sqrt{\pi a_b^3}}e^{-i\mathbf{k}\mathbf{r}_\parallel} \tag{1.8}$$

Here Ψ_λ is the unperturbed eigenfunction of H_{WE}^0. The envelope functions for the confined electron and hole are denoted as χ_e and χ_h correspondingly and for $k=0$ given by equation (ISE:9). The numerical calculations

(See Fig.1.2 and Fig.1.3) show that for a mono-layer of the cuprous oxide $\lambda \approx 0.881$, $a_b \approx a = 4.6$ $\mathring{A}$, i.e. in this case one can consider the $1S$ quadrupole exciton to be "Frenkel-like" localized exciton with k dependent oscillator strength. Without central cell corrections the value of the binding

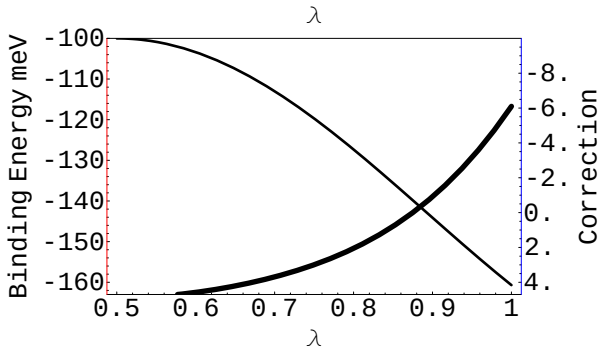

Figure 1.3: (Color online) For numerical estimation of the confined quadrupole Bohr radius as an approximation I took a_b to be the bulk Bohr radius 5.1 $\mathring{A}$. So the "correction" equation (1.7) becomes function of only one parameter λ and so does the binding energy (1.6).

energy is 124 meV (minimum of the dashed curve on Fig.1.2). With CCC it is lowered to 154 meV and corresponds to the minimum on the lower solid curve of Fig.1.2. Now in the weak confinement of the IQW there is a restriction on the value of the parameter λ given by equation (1.7). So the standard binding energy (second term in the total energy (1.6)) slightly grows with the increasing parameter λ [6]. But the CCC decreases with increasing con-

[6] $\lambda = 1/2$ for the bulk, and $\lambda = 1$ for the maximum of the confinement (strong confinement regime)

finement λ. This results in binding energy for weak confinement bigger than bulk case without CCC but slightly smaller than for the bulk case with CCC. This unusual behavior is entirely attributed to the confinement dependent CCC.

The confinement in the IQW increases the overlap of the electron and hole wave functions, which in turn increases the oscillator strength of the "yellow" transition. I am only able to estimate the oscillator strength in case of quantum confinement. I consider a non radiative interface exciton, which refers to the states outside the photon cone, $k \geq \frac{\omega\sqrt{\varepsilon}}{\hbar c}$. WE propagating in the plane are trapped and accompanied by the light field which is evanescent in the direction perpendicular to the interface. In the strictly two-dimensional limit, the oscillator strength of the lowest state scales as $f^{2D}/Sa_b \sim (\lambda_k)^{-3}/a_b^3$. The oscillator strength per unit volume scales as $f^{3D}/V \sim 1/a_b^3$. The maximum enhancement of the oscillator strength in IQW with respect to the bulk case is eight times and results in giving $f^{2D} \approx 8 \cdot 3.7 \times 10^{-9}$. In general, due to the interaction with the FE f^{2D} will have a weak dependence on the wave vector. Also the exciton resonance broadens due to imperfections of the IQW. In my case, the IQW is rather thin, which gives rise to interface roughness and thickness fluctuations. Therefore the exciton mode should show a line width of about $1\,\mu eV$ (the lifetime $\approx 1.7\,ns$).

The results for the confined quadrupole excitons in cuprous oxide obtained in this section are going to be used in the rest of the chapter. Note that the main reason to have the WE energy shift due to the confinement is that it is of the same order of magnitude as the coupling parameter itself.

1.3 PS:CA:DCM2 as an organic part of the hybrid

As it was already discussed, for the best manifestation of the hybridization effect one has to be able to tune the energy of the Frenkel and Wannier-Mott excitons into resonance. Also the Frenkel exciton lifetime should be comparable to the lifetime of the 1S quadrupole exciton, otherwise the hybrid would not live long enough to utilize properties of the quadrupole part. So I decided to use in our model the Frenkel exciton formed in a recently reported amorphous organic thin film doped with the red laser dye: [2-methyl-6-2-(2,3,6,7-tetrahydro-1H, 5H - benzo[i,j] - quinolizin - 9 - yl) - ethenyl] - 4H - pyran - 4 - ylidene] propane dinitritle (DCM2) [7], which has an electric dipole moment of 11 D in the ground state. To achieve a red spectral shift of DCM2 into the resonance with the 1S quadrupole exciton I propose to use a low DCM2 dopant concentration in a two component host consisting of polystyerine (PS) and the polar small molecule camorphic anhydride (CA).

Because DCM2 and CA (dipole moment $\approx 6\ D$) are highly polar molecules, and PS is a nearly non-polar (less than 1 D), one can "tune" the spectral shift by means of adjusting the relative concentration of the DCM2 and CA molecules. Increasing the DCM2 concentration one increases the strength of the local electric fields present in the film. In my case I will keep the DCM2 concentration constant and low (0.05%), to avoid possible overlapp of the organic and inorganic excitons, and limiting DCM2 aggregation effects. At the same time, the dielectric properties of the film are modified by changing the concentraton of CA, which has a large ground state dipole moment relative to its molecular weight and is opticaly inactive in the relevant region of the DCM2 photoluminiscence. According to the work of Bulovic [7], the dielectric permitivity increases with increasing CA concentration linearly:

$$\tilde{\epsilon} = 2.44 + 0.13\,(CA\%) \tag{1.9}$$

In contrast, the index of refraction of the film at yellow light frequency is nearly constant $n \approx 1.55$. The PS provides a transparent, non polar host matrix. Such a mechanism for the spectral shift was termed "solid state solvation", as the solvation mechanism underlying "solvatochromism" of organic molecules in liquids [15].

The theory of "solvatochromism" relates the experimentally observed

changes in emission and absorption spectra of a solute (DCM2) to the dielectric permitivity of a solvent (PS:CA). An electronic transition in the solute (due to photon absorption) produces a corresponding change in the solute charge distribution, which causes the surrounding solvent molecules to respond to this new field in two ways:

1. through electronic cloud reorganization (polarizability) which is referred to as 'fast' solvation which occurs during 0.16 fs judging from the relaxation spectrum of the DCM2 (line width $\approx 0.25\ eV$);

2. through gross spatial movement due to physical translation and rotation ("slow" solvation). During this phase the radiative recombination from the FE is prohibited and allows the FE exciton to live 3.3 ns. In my proposed scheme, the actual hybridization with 1S quadrupole exciton occurs during this time interval as it is comparable to the life time of the quantum confined quadrupole exciton, while the lifetime of the DCM2 in vacuum is determined by FC effect which is much faster;

This is apart from the Frank-Condon (FC) shift due to solute nuclear reorganization. A schematic of the dynamical tuning of the FE and WE energy levels is presented on Fig.1.4. See the caption for more detailed explanation. Once the FE energy falls into the vicinity of the coupling parameter with

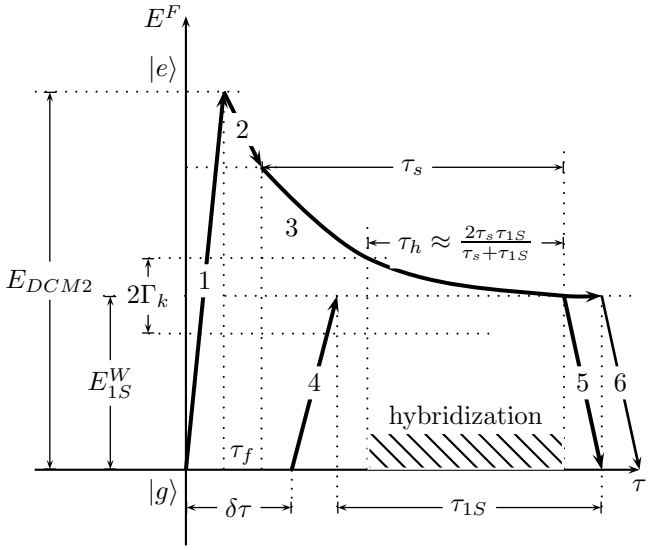

Figure 1.4: Schematic of dynamic tuning of FE and $1S$ quadrupole WE by means of "solid state solvation" (SSS) red shift effect. Following photon absorption (1) in DCM2 there are distinct dynamic phases: (2) fast adjustment of the electronic configuration in DCM2 due to interaction with polar CA molecules within the time frame of pico seconds τ_f; (3) slow self-adjustment of DCM2 and CA molecules $\tau_s \approx 3.3\,ns$; (4) second "yellow" photon delayed by $\delta\tau \approx \tau_s - \tau_{1S}$ is absorbed by Cu_2O confined $1S$ quadrupole exciton with lifetime $\tau_{1S} \approx 1.7\ ns$; hybridization occurs when detuning between this two types of exciton becomes smaller than the $\mathbf{k}$ dependent coupling parameter, lifetime of the hybrid is defined by τ_s and τ_{1S}; (5) phosphorescence due to the hybrid exciton recombination. (6) shows possible recombination of non-interacting excitons.

the quadrupole exciton (resonance condition) the hybridization occurs. The detailed dynamics of the hybrid is the subject of our future work. Presently I assume that the effective lifetime of the hybrid is $\frac{\tau_s \tau_{1S}}{\tau_s + \tau_{1S}}$ and requires two photons to populate both branches of the hybrid exciton. I performed calculations for the energy of the FE under the "continuum" approximation, in which the surrounding molecules of the solvent are replaced by a continues dielectric. The molecules of the solute are described by a spherical cavity of radius a_F of the DCM2 molecules and the corresponding charge distribution is reduced to the dominant dipole moment [16]. Then the total emission energy including the solvation effect can be written as:

$$E = E_0 + \Delta E_{solv} \tag{1.10}$$

Here E_0 is the emission energy in vacuum including the FC shift; and $E_{solv} = -\frac{1}{a_F^3}(\mu_g - \mu_e)(\Lambda\mu_e + \Lambda_{op}\mu_g)$, here I introduced μ_e and μ_g to be solute excited and ground states dipoles, respectively; and

$$\Lambda = \frac{2(\tilde{\epsilon} - 1)}{2\tilde{\epsilon} + 1},\ \Lambda_{op} = \frac{2(n^2 - 1)}{2n^2 + 1}$$

associated with "slow" and "fast" relaxation processes described above, respectively.

The equations (1.9, 1.10) along with experimental fitting for $-\frac{1}{a_F^3}(\mu_g - \mu_e)\mu_e = 0.57$ yields the concentration of the CA $\approx 22\%$ corresponding to the

resonance with the confined $1S$ quadrupole energy 2.05 eV.

There is one sensitive point I make in my work, namely the necessity of the second delayed photon. One photon does allow hybridization once the energy of the FE exciton is close enough. However only one branch of the hybrid is going to be populated. Because one approaches the resonant energy from above, the upper branch is the one to be populated. The lower branch may be populated by multi acoustical phonon process. But I do not know how long it takes to populate from the maximum of the upper branch to the minimum of the lower branch. For the temperature of 1.7 K it takes approximately 26 of such phonon processes without the Stark effect (See section 1.4) or 7 of them with the Stark effect. Even though such transitions are allowed, it may take more time than the life time of the hybrid. For example the lifetime of the $1S$ ortho-exciton itself is determined by the acoustical phonon assisted transformation to the para-exciton which involves change in energy of 12 meV. This is comparable to the doubled coupling parameter: $2\Gamma_k$.

Hence, I assume that the second photon is absorbed in order to assure both branches are populated regardless of the initial conditions. When both photons are in resonance with the WE exciton $\hbar\omega \approx E_{1S}$, the second photon

provides conservation of energy:

$$\hbar\omega + \hbar\omega = (E_{1S} + \Gamma_k) + (E_{1S} - \Gamma_k)$$

Conclusively, it this section I derived necessary concentration of the solvent (CA) to provide resonance between WE and FE. Also I estimated the life time of the formed hybrid.

1.4 Induced Stark effect

In this section I investigate a new effect which plays a rather significant role in forming any hybrid exciton. Let us refer to it as an induced quantum confined Stark effect. The main idea is the following. There is an evanescent potential in the z - direction and corresponding $\mathbf{k}$ - dependent electric field due to the FE, penetrating into the inorganic quantum well (see Fig.1.1). This field induces some polarization of the bound electron-hole pairs of the WE. This polarization leads to an effective screening of the electric field and results in reducing the coupling.

I consider the FE as a polarization wave [1] $\mathbf{P}(\mathbf{r})$ confined to a perfectly 2D organic quantum well (OQW) placed at position $z' \approx \frac{L_w}{2}$ (See Fig.1.1). Neglecting the constant phase of the wave $e^{-i\frac{\mathbf{k}\mathbf{L}_w}{2}}$ the polarization per unit

area S is given as:

$$\mathbf{P}_i(\mathbf{r}) = a_F \mu^F \mathbf{e}_i \frac{e^{-i\mathbf{k}\mathbf{n}_\parallel}}{\sqrt{S}} \delta\left(z - \frac{L_w}{2}\right)$$

Here μ^F is the dipole moment associated with the FE. Now one can move from discrete set of FE to a continuous distribution and take into account that

$$\sum_{\mathbf{n}} e^{-i\mathbf{k}\mathbf{n}_\parallel} = \frac{1}{a_F^2} \int e^{-i\mathbf{k}\mathbf{r}_\parallel} d\mathbf{r}_\parallel$$

In this continuous approximation one gets the final result for the polarization created by the FE exciton propagation along the interface:

$$\mathbf{P}_i(\mathbf{r}) = \mu^F \mathbf{e}_i \frac{e^{-i\mathbf{k}\mathbf{r}_\parallel}}{a_F\sqrt{S}} \delta\left(z - \frac{L_w}{2}\right) + c.c$$

The potential due to this polarization wave is given by [1]:

$$\varphi_{\mathbf{k}}(\mathbf{r}) = G\left(\mathbf{r}, \mathbf{n}_\parallel, \mathbf{k}\right) \nabla \mathbf{P} = -\nabla_i G\left(\mathbf{r}, \mathbf{n}_\parallel, \mathbf{k}\right) \mathbf{P}_i$$

The standard Green's function for $z < z'$ is given by:

$$G(z, z', \mathbf{k}) = \frac{4\pi}{\varepsilon(\mathbf{k}) + \tilde{\varepsilon}} \frac{e^{k(z-z')}}{k}$$

It gives rise to the potential of the form:

$$\varphi_{\mathbf{k}}(\mathbf{r}) = \sum_i \left[k\delta_{i,z} + ik\right] G(\mathbf{k}, z', z) \mathbf{P}_i(\mathbf{r}) = \mu^F \frac{e^{-i\mathbf{k}\mathbf{r}_\parallel}}{a_F\sqrt{S}} \frac{4\pi}{\varepsilon + \tilde{\varepsilon}} e^{k(z-z')} \quad (1.11)$$

Here I utilized the fact that the complex conjugate part cancels out the imaginary part of the above expression. The electric field creates an additional

polarization in the IQW, which I am going to estimate by its effect upon the coupling parameter. Effectively this polarization manifests itself by giving an envelope function equation in the IQW for the electron and hole. Following a standard procedure (Bastard [17]), the equations governing the electron (hole) envelope function in the IQW:

$$\left(-\frac{\hbar^2}{2m_e}\frac{d^2}{dz^2} - eF_{\mathbf{k}}z\right)\chi^e_{\mathbf{k}}(z) = (E - E_c)\,\chi^e_{\mathbf{k}}(z)$$
$$\left(-\frac{\hbar^2}{2m_h}\frac{d^2}{dz^2} + eF_{\mathbf{k}}z\right)\chi^h_{\mathbf{k}}(z) = (E_v - E)\,\chi^h_{\mathbf{k}}(z)$$

Here I used the long wave approximation for the potential namely taking the effective electric field in the form: $F_k \simeq k\varphi_{\mathbf{k}}(z = z')$. The total energy shift due to the induced field is negligible for small difference in the electron and hole masses and small width of the IQW. The envelope functions are subject to zero boundary conditions at both sides of the IQW. Here one comes across some difficulties. Although this system has an exact solution the standard approach with Airy functions Ai and Bi will lead us to a rather complicated but exact result:

$$\chi^n_k(z) = C_{1,n,k}Ai\left(\frac{eF_kz - \zeta_{n,k}}{\zeta_{0,k}}\right) + C_{2,n,k}Bi\left(\frac{eF_kz - \zeta_{n,k}}{\zeta_{0,k}}\right) \tag{1.12}$$

In the last expression I introduced the following notation for the electron

(hole) energy change due to the confinement and FE induced polarization:

$$\zeta_{0,k} = \left(\frac{\left(eF_k\hbar\right)^2}{2m} \right)^{1/3}$$
$$\zeta_{n,k} = E_n - E_0 - e\varphi_{\mathbf{k}}(0)$$

With $E_0 = 0$ for the electron and $E_0 = -E_g$ for the hole (I also omitted indexes e, h for simplicity). The normalization constants are connected as:

$$C_{1,n,k} = Ai\left(\frac{eF_k\frac{L_w}{2} - \zeta_{n,k}}{\zeta_{0,k}} \right) / Bi\left(\frac{eF_k\frac{L_w}{2} - \zeta_{n,k}}{\zeta_{0,k}} \right)$$

Therefore, the energy levels can be found by taking boundary conditions as discrete solutions for the following nonlinear equation:

$$\begin{aligned} &Ai\left(\frac{eF_k\frac{L_w}{2} - \zeta_{n,k}}{\zeta_{0,k}} \right) Bi\left(\frac{-\zeta_{n,k} - eF_k\frac{L_w}{2}}{\zeta_{0,k}} \right) - \\ &-Bi\left(\frac{eF_k\frac{L_w}{2} - \zeta_{n,k}}{\zeta_{0,k}} \right) Ai\left(\frac{-\zeta_{n,k} - eF_k\frac{L_w}{2}}{\zeta_{0,k}} \right) = 0 \end{aligned} \tag{1.13}$$

For the hole one has to change $e \to -e$. Although equations (1.12) and (1.13) exhibit the exact solution, they are rather complicated for further analytical description of the hybrid exciton states.

There are some approximate ways to treat the problem of the electron and hole wave functions relative shift in the induced field. First, let me treat the electric field F_k using a perturbation theory. In this approach I can explicitly see the term due to induced polarization. This perturbation

approach is applicable if the energy difference between unperturbed ground and first exited state is much bigger than the perturbing potential at the average position of the particle $z = 0$. For the case of a mono-layer of cuprous oxide it is applicable only for the very small wave vector region. But it may be used as a correction in the dipole-dipole hybridization. In the first order there will be *no change* in total energy proportional to the square of the FE induced electric field. But the wave functions will be changed to the following expression:

$$\chi_k^e(z) = \sqrt{\frac{2}{L_w}} \cos\left(\frac{\pi z}{L_w}\right) - \frac{32 F_k L_w^3 em}{27\pi^2\hbar^2} \sqrt{\frac{1}{L_w}} \sin\left(\frac{2\pi z}{L_w}\right) \tag{1.14}$$

Because the above expression (1.14) is still rather complicated, I consider only the lowest energy levels transitions so it is possible to consider instead of infinite IQW, an "equivalent" parabolic profile defined through its lowest energy level as

$$\frac{1}{2}\hbar\omega_0^2 = \frac{(\pi\hbar)^2}{2mL_w}$$

Hence, I am able to consider $\mathbf{k}, L_w$ values in the region where perturbation theory is not applicable. The reduced parabolic problem has an exact solution with the same energy as was given by perturbation theory for the lowest transition. The envelope function normalized inside the given IQW has a

Gaussian form [7]:

$$\chi_{\mathbf{k}}^{e,h}(z) = \frac{(2\pi)^{1/4}}{\sqrt{erf\left(\pi/\sqrt{2}\right) L_w}} \exp\left(-\frac{(z - z_{e,h})^2}{R_0^2}\right) \tag{1.15}$$

In the above equation (1.15) the dimension R_0 of the parabolic IQW is taken to be the same for the electrons and holes:

$$R_0 = \sqrt{\frac{\hbar}{m_e \omega_0}} = \frac{L_w}{\pi}$$

The shifted average electron and hole positions are given by:

$$z_{e,h} = \pm \frac{eF_k^2}{2m\omega_0^2} = \pm \frac{eF_k^2 m L_w^4}{2\pi^4 \hbar^2}$$

In the next section I am going to use these envelope functions to calculate the coupling parameter.

1.5 The coupling parameter and dispersion

The energy of interaction between the organic dipole and inorganic $1S$ quadrupolar excitons can be written as [18]:

$$\hat{H}_{int} = -\frac{1}{6} \sum_{\alpha} \sum_{\beta} \hat{Q}_{\alpha\beta} \frac{\partial}{\partial x_\alpha} \hat{F}_\beta = -\frac{1}{6} \hat{Q}_{\alpha,\beta} |0\rangle D_{i,\alpha,\beta}\left(\mathbf{n} - \mathbf{r}_{\parallel}, z', z\right) \langle 0| \hat{d}_i^F$$

Here $\hat{Q}_{\alpha\beta}$ is the quadrupole transition operator; the electric field operator $\hat{F}_\beta$ is due to the FE as given by the equation (1.11); $D_{i,\alpha,\beta}$ is the Green's

[7] I assume $m_e = m_h$

function in momentum space. The interaction parameter is given by the following transition matrix element:

$$\Gamma_{\mathbf{k}} = \langle W, \mathbf{k}| H_{int} |F, \mathbf{k}\rangle = \sum_{\alpha,\beta,i} \sum_{\mathbf{n}} \int dz d\mathbf{r}_{\parallel} \langle W, \mathbf{k}| \hat{H}_{int} |F, \mathbf{k}\rangle$$

The quadrupole transition matrix element may be obtained by using the relation $\frac{1}{S}\sum_{\mathbf{q}} \varphi_{1S}(\mathbf{q}) = \varphi_{1S}(\mathbf{r}_e - \mathbf{r}_h = 0)$ between the wave function of the relative electron-hole motion of the $1S$ exciton φ_{1S} (normalized to the unit area S) and its momentum representation $\varphi_{1S,\mathbf{q}}$. Hence, the Fourier component of the quadrupole exciton transition from the ground state of the crystal [19] is given as:

$$\langle W, \mathbf{k}| \hat{Q}_{\alpha,\beta} |0\rangle = \frac{e^{i\mathbf{k}\mathbf{r}_{\parallel}}}{\sqrt{S}} \sum_{\mathbf{q}} \varphi_{1S}(\mathbf{q}) Q_{\alpha,\beta}(\mathbf{q}) = \sqrt{\frac{2}{\pi}} \frac{\lambda Q_{\alpha,\beta}}{a_b} \frac{e^{i\mathbf{k}\mathbf{r}_{\parallel}}}{\sqrt{S}} \chi_k^e(z) \chi_k^h(z)$$

Considering the weak dependence of the conduction $u_{c,q}$ and valence $u_{\upsilon,q}$ Bloch functions on the wave vector $\mathbf{q}$, the quadrupole moment of the interband transition may be written as:

$$Q_{\alpha,\beta} \approx Q_{\alpha,\beta}(\mathbf{q} = \mathbf{0}) = \frac{1}{\upsilon_0} \int_{\upsilon_0} \mathrm{d}\mathbf{s} u_{c\mathbf{q}}^*(\mathbf{s}) x_\alpha x_\beta u_{\upsilon\mathbf{q}}(\mathbf{s})$$

with the integration taken over the unit cell of the cuprous oxide υ_0. The expectation value of the FE exciton dipole transition operator is given as:

$$\langle 0| \hat{\mu}_i^F(\mathbf{n}) |F, \mathbf{k}\rangle = \sqrt{\frac{\pi}{S}} a_F \mu_i^F e^{-i\mathbf{k}\mathbf{n}}$$

The Green's function in momentum space for the given geometry is given by

$$D_{i,\alpha,\beta}\left(\mathbf{k}, z', z\right) = \frac{4\pi}{\varepsilon + \tilde{\varepsilon}} k^2 e^{k(z-z')} \left(\frac{ik_i}{k} + \delta_{i,z}\right) \left(\frac{ik_\beta}{k} + \delta_{\beta,z}\right) \left(\frac{ik_\alpha}{k} + \delta_{\alpha,z}\right) \tag{1.16}$$

For the selection rules based upon the specific geometry of the problem and the corresponding Green's function see Table 1.7 of the Appendix. Without loss of generality one may take the wave vector along the x - axis. From the Green's function (1.16), polarization selection rules [20], my specific type of interaction energy and the requirement of having real eigenvalues one can conclude that the only possible direction of the wave vector and dipole orientation is given by nonzero components μ_x^F and $Q_{x,z}$ respectively.

I would like to note here that there is another possible approach to the problem of resonant interaction between these two types of exciton. If one modifies the results of Moskalenko [19] for my case and introduces an effective polarization due to quadrupole transitions via a $\mathbf{k}$ dependent inter-band dipole element

$$\mu_{ij,\mathbf{k}}^W \sim |Q_{ij}| \left(\mathbf{e}_i \mathbf{k}_j + \mathbf{e}_j \mathbf{k}_i\right) \tag{1.17}$$

Then one uses the corresponding interband polarization, this would coincide with a case of 'dipole-dipole' transitions, when the electric field created by the set of WE dipoles will interact with the dipoles in the organic. In this

way one could directly use the results of Agranovich [1]. Due to an additional requirement for the Hamiltonian to be hermitian, it would give us the following result for the coupling constant:

$$\Gamma_{i\neq j}\left(\mathbf{k}\right) \sim Re\left(\mu^{W}_{ij,\mathbf{k}} D_{j\alpha} \mu^{F}_{\alpha}\right) \sim \left|Q_{x,j}\right| \mu^{F}_{x} k_{x} \mathbf{e}_{j} \mathbf{e}_{x}$$

Here I used the fact that the wave vector has only an x component. And so this coupling parameter vanishes in this approximation as $j \neq x$. For that reason in this thesis I study interaction of the cuprous oxide quadrupole with the gradient of the electric field created by organic FE placed near the interface between the organic $PS:CA$ and inorganic Cu_2O.

Calculating the integral of the coupling parameter and summing over the dipoles for the case when a perturbation approach is applicable yields:

$$\Gamma\left(\mathbf{k}\right) = \Gamma_{1}\left(\mathbf{k}\right) + \Gamma_{2}\left(\mathbf{k}\right)$$

Here $\Gamma_{1}\left(\mathbf{k}\right)$- corresponds to the unperturbed coupling parameter, and the last term is due to the perturbation.

$$\Gamma_{1}\left(\mathbf{k}\right) = \frac{8\sqrt{2\pi}}{6\left(\varepsilon\left(k\right)+\tilde{\varepsilon}\right)L_{w}} \frac{k e^{-kz'} sinh\left(\frac{L_{w}k}{2}\right)}{\left(1+\left(\frac{kL_{w}}{2\pi}\right)^{2}\right)} \frac{Q_{xz}\mu^{F}_{z}}{a_{F}a_{b}L_{w}} \tag{1.18}$$

To increase this coupling term one may consider the organic host PS:CA with DCM2 organized in a multi-layered structure [8]. The same approach can be

[8] not shown on Fig.1.1

generalized for the case of multi-layered organic with distance between the layers to be equal to twice the radius of the FE (compact composition). It can be shown that one has to multiply (1.18) by $2e^{2ka_F}/\left(e^{2ka_F}-1\right)$. The factor of two in the last expression indicates that the organic is placed on both sides of my IQW and one must consider the symmetrical Green's function in the interaction.

Another term in the total coupling parameter is due to the induced Stark effect [9] and has the form:

$$\Gamma_2(\mathbf{k}) \sim -\frac{512}{27}\frac{L_w^4 k F_{\mathbf{k}} \cdot C \cdot M}{\pi^2\hbar^2}\frac{e\cdot\cosh\left(\frac{kL_w}{2}\right)}{k^4L_w^4+10\pi^2k^2L_w^2+9\pi^4}$$

Here $F_{\mathbf{k}}$ is the electric field induced by the organic layer of dipoles. The terms proportional to L_w^6 have been omitted.

For the region of wave vector and width of the IQW where one can not use perturbation theory another form of the coupling parameter must be developed. In this case it is convenient to use the effective parabolic potential and the envelope functions in the form (1.15). Therefore, the coupling parameter acquires the form:

$$\begin{aligned}\Gamma(k) \sim k^2 e^{-kz'}\frac{\sqrt{2}}{4}\exp\left(-\frac{16z_e^2-R_0^4k^2}{8R_0^2}\right)\times \\ \times\left(erf\left(\frac{\sqrt{2}}{4}(2\pi+kR_0)\right)+erf\left(\frac{\sqrt{2}}{4}(2\pi-kR_0)\right)\right)\end{aligned} \tag{1.19}$$

[9] There is no induced Stark effect in multi-layered case due to the corresponding symmetry of the organic

Here for simplicity I put $z_e \approx -z_h$, or in another words $m_e \approx m_h$. For numerical estimation of the quadrupole matrix elements I used the well known [19] result for corresponding oscillator strength:

$$f_{xz,\mathbf{k}_0} = \frac{4\pi m_0 E_g}{3e^2\hbar^2}\left(\frac{a_b}{2\lambda a}\right)^3 \mathbf{e}_z \cdot \mathbf{k}_{0,x} \cdot Q_{x,z}$$

Where λ represents affect of quantum confinement, and $|\mathbf{k}_0| = 2.62 \cdot 10^5 cm^{-1}$.

The dispersion of the hybrid state in case of negligibly small detuning of 1S exciton with the DCM2 transitions (resonance) is presented on Fig.1.5. The first (1) dashed lines correspond to the coupling parameter when the Stark effect is neglected. So it corresponds to to the upper part of the dispersion in this approximation. To show the effect of the 'parabolic' approximation on the coupling I drew the second dashed line (2). And the third dashed line (3) is when the Stark effect is small enough to be taken as a perturbation without applying the 'parabolic' approximation.

Note that I consider the quadrupole-dipole interaction only between cuprous oxide and DCM2 excitons and neglect the coupling with PS:CA host transitions. This is because it has the much smaller oscillator strength of the corresponding inter-band dipole moments for the transitions which are off resonance with the inorganic. Neglecting the Stark effect, from this numerical estimation it is easy to see that for the values of $kR_0 \ll 1$ the expressions

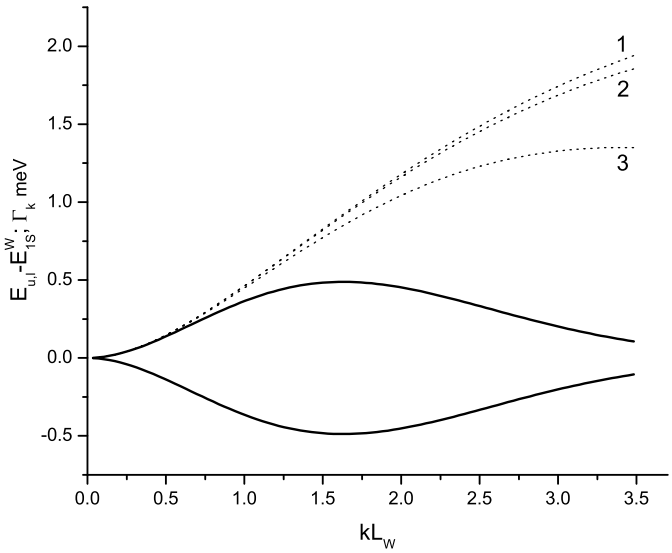

Figure 1.5: The solid lines represent upper and lower branches of the quadrupole-dipole hybrid dispersion when the coupling is calculated in the parabolic approximation and the induced Stark effect is taken into account; the dashed lines correspond to the coupling parameter for different approximations: (1) - infinite IQW and the induced Stark effect is neglected, (2) - parabolic approximation, (3) - infinite IQW with the induced Stark effect treated as a perturbation

(1.18) and (1.19) are equivalent.

1.6 Numerical results and discussion

Although the oscillator strength of the $1S$ quadrupole exciton is three orders of magnitude smaller than for the nearest dipole allowed exciton, strong spatial dispersion [10] makes the maximum of the coupling parameter comparable with those for the dipole-dipole case.

The $1S$ quadrupole exciton has a rather big mass of the ($\approx 3m_0$) and so is comparable to the mass of the FE ($\geq 5m_0$). Also one has to take into account a significant effect of the IQW width fluctuation. Indeed, the effect of the width fluctuation is energy change between confined and the bulk cases, which corresponds to energy drop of $E_{1S,binding}(\lambda = 1) - E_{1S,binding}(\lambda = 0.881) = 17\ meV$ (See Fig.1.3). Hence, due to both of this effects I neglected the kinetic energy of the confined quadrupole $1S$ exciton. The motion occurs via site to site hopping in a FE-like way. Thus the quadrupole-dipole hybridization effect is more pronounced than the dipole-dipole hybridization because it is not masked by the kinetic energy of the exciton [1].

Also the hybridization effect is not masked by the large radiative decay

[10] factor of k in equation (1.18) resulted from the quadrupole nature of the $1S$ transition in the cuprous oxide

rate of the FE. Instead of the classical spontaneous radiative rate of the organic I use the "solid state solvation" process to obtain a different relaxation mechanism. Namely, one has the dynamical red shift of the DCM2 FE during the "slow" phase of the solvation process, when the energy of the photon excited DCM2 molecules is partially transfered to the polar CA molecules by non-radiative dipole-dipole electro magnetic interaction followed by immediate fast [11] radiative decay. To compare the radiative decay rate (life time) with the hybridization parameter I simplify the dynamics to the following statement. The FE has fixed resonant energy with the $1S$ quadrupole WE but has an "effective" lifetime equal to τ_s. So if one omits all the possible non-radiative channels of decoherence except the radiative decay, the radiative decay rate from the hybrid to the ground state is calculated using Fermi's golden rule:

$$\hbar\gamma_{hybrid}\left(u,l;k\right)=2\pi\left|\left\langle g\right|H_{\text{int}}\left|u,l;k\right\rangle\right|^{2}\delta\left(\hbar\omega_{k}-E_{u,l}\right)=\frac{A_{l,u}^{2}\hbar}{\tau_{s}}+\frac{B_{l,u}^{2}\hbar}{\tau_{1S}}=$$
$$=\frac{\hbar}{2}\frac{\tau_{s}+\tau_{1S}}{\tau_{s}\tau_{1S}}\approx 0.29\,\mu eV$$

The above line-width of the QDH corresponds to 1.1 ns of the hybrid lifetime.

Note that much better results for the decay rate of the hybrid may be obtained from a solution of the kinetic equations governing the dynamics of solvation and hybridization. This is a subject for my future work and will

[11] compared to the τ_s

be reported elsewhere

From this estimation the ratio of the hybrid radiative rate to the maximum of the coupling parameter is 0.0006 which is two orders of magnitude smaller than predicted [2] value 0.09 for the dipole-dipole hybrid in a quantum dot. We have not derived the dependence of the damping on the confinement and Bohr radius of the quadrupole-dipole hybrid. So I used the work of Engelman [2] on the fully confined quantum dot hybrid. And also work of V. Agranovich [1] on the less confined quantum wire dipole-dipole confinement. This complies with my strategy of making comparative analysis between quadrupole-dipole and dipole-dipole hybrid cases. Indeed it was shown in case of fully localized quantum dot dipole-dipole hybridization that the ratio of the hybrid exciton damping parameter to the coupling is proportional to $i\hbar\gamma_{hybrid}/\Gamma_k \propto \sqrt{a_b^3}$ ($\sqrt{a_b}$ - in case of quantum wires [1]). Thus, the *quadrupole-dipole hybridization* takes advantage of the *small radius* of the $1S$ quadrupole. Also the fact of *comparable life time* of the organic and $1S$ quadrupole exciton significantly influences this ratio.

A noteworthy feature of the resulting upper (u) and lower (l) branch dispersion in Fig.1.5 is the well pronounced minimum on the lower branch. This minimum of the hybrid dispersion can be populated by pump-probe experiment. Consequently, it may be possible to have *finite* BEC critical

temperature in case of quasi 2D excitons, due to the fact of non parabolic dispersion of the lower branch of the hybrid. This can provide a good basis for searching for BEC in such a hybrid. A new type of an interface polariton is also expected. It is a subject of my current research.

Note that I mentioned the possible BEC as a *possibility* only. Judging from the fact of the big saturation density of the hybrid and minimum of the energy on the lower branch. this minimum would make the hybrid exciton strongly localized and many dissipative processes (such as Auger heating [21]) are expected to be suppressed. Also the non-parabolic dispersion allows the system to have a finite condensation temperature contrary to the case of $2D$ excitons with parabolic dispersion. But the main question about the life time of the hybrid is still a subject of my current research. So I do not make a concrete statement about the BEC of the hybrid but rather make an educated guess on that.

In Part II of this thesis I propose rather different and at the same time similar approach for BEC search in cuprous oxide. The evanescent polariton described there is also characterized by the small radius and long life time. But instead of the hybridization with highly localized FE I propose to use Mie resonances of a sphere in contact with cuprous oxide film. Due to controllable parameters of such a sphere it can be designed to have a whispering gallery

mode (WGM) in resonance with the WE. The main advantage of such a hybrid over the organic-inorganic scheme is that the life time of the WGM is dominating over the lifetime of the WE. But it also has it's drawback. The evanescent polariton is formed only in close vicinity near the sphere and so the spacial coherence of possible BEC is small. Using linear chain of spheres improves the spacial coherence, but at the same time reduces the life-time of the polariton. Therefore, only an experiment can show which scheme provides better conditions for BEC of the hybrid.

1.7 Appendix I

O_h					
Symmetry		Electric dipole operator	Electric quadrupole operator		Basis
		$^3\Gamma_4^-$	$^3\Gamma_5^+$	$^2\Gamma_3^+$	
Paraexciton	$^1\Gamma_2^+$	F	F	F	x^2-y^2 y^2-z^2 z^2-x^2
Orthoexciton	$^3\Gamma_5^+$	F	A	F	$xy; yz; zx$
Basis		$x; y; z$	$xy; yz; zx$	$2z^2-x^2-y^2$; $\sqrt{3}(x^2-y^2)$	

Table 1.1: Selection rules for the excitons in bulk Cu_2O. F-forbidden; A-allowed transition

D_{4h}								
Symmetry		Electric dipole operator		Electric quadrupole operator				Basis
		${}^1\Gamma_2^-$	${}^2\Gamma_5^-$	${}^2\Gamma_5^+$	${}^1\Gamma_3^+$	${}^1\Gamma_4^+$	${}^1\Gamma_1^+$	
Paraexciton	${}^1\Gamma_3^+$	F	F	F	F	F	A	(x^2-y^2)
Orthoexciton	${}^1\Gamma_4^+$	F	F	F	F	A	F	xy
	${}^2\Gamma_5^+$	F	F	A	F	F	F	$yz; zx$
Basis		$z; x$	z	$yz; zx$	x^2-y^2	xy	R	

Table 1.2: Selection rules for the exciton in a Cu_2O quantum well. F-forbidden; A-allowed transition

	Q_{xy}	Q_{xz}	Q_{yz}
$\mathbf{k}_{[1,0,0]}$	$D_{xxy}=0$ $D_{yxy}=0$ $D_{zxy}=0$	$D_{xxz}=-\frac{4\pi}{\varepsilon+\tilde{\varepsilon}}k^2e^{k(z-z')}, d_x$ $D_{yxz}=0$ $D_{zxz}=i\frac{4\pi}{\varepsilon+\tilde{\varepsilon}}k^2e^{k(z-z')}, d_z$	$D_{xyz}=0$ $D_{yyz}=0$ $D_{zyz}=0$
$\mathbf{k}_{[0,1,0]}$	$D_{xxy}=0$ $D_{yxy}=0$ $D_{zxy}=0$	$D_{xxz}=0$ $D_{yxz}=0$ $D_{zxz}=0$	$D_{xyz}=0$ $D_{yyz}=-\frac{4\pi}{\varepsilon+\tilde{\varepsilon}}k^2e^{k(z-z')}, d_y$ $D_{zyz}=i\frac{4\pi}{\varepsilon+\tilde{\varepsilon}}k^2e^{k(z-z')}, d_z$
$\mathbf{k}_{[0,0,1]}$	$D_{xxy}=0$ $D_{yxy}=0$ $D_{zxy}=0$	$D_{xxz}=0$ $D_{yxz}=0$ $D_{zxz}=0$	$D_{xyz}=0$ $D_{yyz}=0$ $D_{zyz}=0$

Table 1.3: Green's function selection rules

Chapter 2

Enhanced photo-thermal bi-stability

The proposed enhancement of nonlinear optical response from the quantum confined WE by means of resonant hybridization with organic FE was first stated in the works of Agranovich [1, 22, 23]. The dipole-dipole hybrid (DDH) is an appropriate coherent linear combination of large radius a_B [1] *dipole allowed* WE and small radius but big oscillator strength *dipole allowed* f^F FE. The new hybrid is characterized by big oscillator strength and small saturation density (strong coupling regime). The expected hybrid optical nonlinearities are large because the ideal bosonic approximation starts to break down at the density of the hybrid close to the saturation density. Close to the saturation, due to overlapping between exciton wave functions, they exhibit rather strong exchange interaction and space filling factor. Compared

[1] small saturation density $\propto 1/a_B^2$ of the order of $10^{12}\ cm^{-2}$

to the bare WE nonlinear response, the hybrid response is enhanced roughly by the factor of the ratio of the FE and WE oscillator strength f^F/f^{WE}.

In Chapter 1 I demonstrated formation of a new type of the hybrid [24]. It occurs between dipole forbidden but quadrupole allowed $1S$ exciton in cuprous oxide quantum well and FE in DCM2:CA:PS [4, 7]. The latter is brought dynamically into the resonance with the exciton in the quantum well by means of "solid state solvation" [15] mechanism. The quadrupole-dipole hybridization (QDH) is of the same order of magnitude (meV) as that of the DDH. Because of the small oscillator strength of the $1S$ quadrupole exciton [10] is compensated by its strong spacial dispersion. This QDH exhibits the key features of big oscillator strength and narrow line width.

In the present work I utilize the properties of the hybrid to enhance and modify nonlinear effects associated with the WE part of the hybrid. Due to the small radius of the $1S$ quadrupole $\approx 7\mathring{A}$ the hybrid may achieve Bose condensation before it reaches the critical bulk density [2]. Therefore, density dependent optical non-linearities which were important in the DDH case are negligibly small for the QDH. Hence, I focus my attention on another nonlinear optical phenomena generic to the cuprous oxide, namely, the photo-

[2] I leave aside many questions about the ability for actual condensation of the hybrid for my future work

thermal bi-stability effect.

The photo-thermal bi-stability effect [25, 26] manifest itself for the density of the pumping laser as small as $P_{ex} = 1\ mWt$. Due to "weak" interaction with acoustic phonons the energy of the WE will experience a red shift linear with the temperature [27, 28, 29]. Also see Chapter 4 for more details. The laser heating is balanced by the surrounding helium cooling. Hence, the resulting temperature on the interface is described by a nonlinear equation with more than one solution for some values of the laser detuning from the resonant energy level. This results in a hysteresis-like pattern for the temperature and absorption.

I am going to show that the fact of hybridization with the organic enlarges the bi-stability region from 200 neV for the bulk cuprous oxide to the order of meV for the hybrid due due to its large oscillator strength. Another remarkable effect of the hybridization is that the QDH exciton induces multiple highly asymmetrical photo-thermal bi-stability effects associated with two dispersion branches of the hybrid. The effective absorption maximum for the lower branch of the QDH exciton experiences a red shift of the order of meV and strongly depends on the pumping intensity.

In the next sections I propose a nonlinear absorption experiment and give an appropriate mathematical model to observe the hybrid bi-stabilty. The

last section of this chapter is devoted to discussion of the numerical results following from my model, and comparison with reported results for the bulk cuprous oxide.

2.1 Nonlinear absorption by the hybrid

The proposed configuration is shown in the following diagram (see Fig.1.1). For the nonlinear absorption experiment let us consider a mono-layer of cuprous oxide placed upon a thin film of an organic compound. The organic I propose is an "solid state solvation" of the red laser dye DCM2 embedded in a transparent host of polystyrene (PS) doped with the polar small molecule camorphic anhydride (CA) (See Chapter 1 for details). One stationary laser (probe) is tuned around the $1S$ quadrupole transitions in the cuprous oxide $\hbar\omega \approx E_{1S} = 2.05\ eV$ (WE). The pumping laser pulses of intensity P_{ex} and energy $\hbar\omega = E_{DCM2}$ allow DCM2 molecular excitations. As it was done in the Chapter 1 I consider the this molecular excitations as the FE. Therefore it can be viewed as a 2D lattice of dipoles placed at $z' \approx L_w/2$. After the pumping pulse the FE experience a red shift linear with the CA concentration due to non-resonant Förster energy transitions to the CA molecules (see Fig.1.3).

As it was shown in the previous chapter, to achieve the red spectral shift

of the FE into the resonance with the quantum confined WE, one has to adjust the CA concentration to $\approx 22\%$ [24]. To avoid complicated problems of the dynamics of the hybridizaton I assume that the FE and WE are in exact resonance once the DCM2 energy is in close proximity to the WE energy $E_{DCM2} - E_{1S} \leq \Gamma_{\mathbf{k}}$. The maximum value of the coupling parameter is about 2 meV (See Fig. 1.5) and is of the same order of magnitude as the dissipative width of the hybrid $\gamma\hbar$. Therefore, the hybridization is well pronounced.

In this Chapter I assume that the cuprous oxide has purity of 99.99% with the reported line-width of $\hbar\gamma_{1S} = 0.1\ meV$ i.e. pico-second lifetime [30] while the FE life-time is of the order of ns. In this case the hybrid life-time is dominated by its inorganic part $\hbar\gamma \approx \hbar\gamma_{1S}$.

The hybridization will strongly affect the absorption of the probe laser and consequently, it will also modify the photo-thermal bi-stability characteristics of the cuprous oxide. To study this effect, let me place the whole system into helium bath with the temperature $T_{bath} = 1.7\ K$. The temperature of the exciton gas T at the interface between the organic and inorganic is determined by the balance between the photo-thermal heating due to the exciton absorption and the cooling by the helium bath.

I also assume that the exciton gas is in equilibrium with the helium bath

(thermalization) [3]. For thermalized excitons one can treat the temperature T as just another parameter of the system.

The rate of helium cooling is given by the following linear term:

$$-C\left(T - T_{bath}\right)$$

The helium thermo-conductivity is denoted as: $C = 2.8 \times 10^3\ s^{-1}$ [26]. To find the heating term I derive below a semi-classical expression for the photo-thermal absorption of the hybrid.

The Hamiltonian of the system can be written in the rotating wave approximation [4] as following:

$$\tilde{H} = \delta b^{\dagger}_{\mathbf{k}} b_{\mathbf{k}} + \Delta b^{\dagger}_{1S,\mathbf{k}} b_{1S,\mathbf{k}} + \Gamma_{\mathbf{k}} \left(b^{\dagger}_{1S,\mathbf{k}} b_{\mathbf{k}} + b_{1S,\mathbf{k}} b^{\dagger}_{\mathbf{k}} \right) + \sqrt{N}\mu^F \left(E b^{\dagger}_{\mathbf{k}} + E b_{\mathbf{k}} \right) \quad (2.1)$$

Here $\delta = E_{DCM2} - \hbar\omega$ and $\Delta = E_{1S} - \hbar\omega$ are the detunings of the laser frequency from the FE and WE respectively; N is the number of unit cells in the organic; E is the electric field of the incoming light; $b_{1S,\mathbf{k}}$ and $b_{\mathbf{k}}$ are annihilation operators for WE and FE respectively. The commutative algebra for this operators is listed in the Appendix.

Because the frequency of the laser pulses is much smaller than ω, one

[3] To assure thermalization of the hybrid excitons I propose to pump the sample with successive laser pulses coming one after another withing the hybrid life-time.

[4] The rotating-wave approximation has been invoked by eliminating the anti resonant terms of the interaction with light; this approximation limits the calculation only to the resonant features of the response.

can consider the laser field turned on adiabatically. Then, the equations of motion for any operator can be solved in a very straightforward manner. Apply to that operator the unitary transformation that diagonalizes (2.1) and then introduce an imaginary part to all detunings, positive for creation operators and negative for annihilation operators. Since the Hamiltonian involves only Bose operators and is quadratic, the unitary transformations that diagonalizes it can be obtained in analytic form. The diagonalization procedure can be written as:

$$U^{-1}\tilde{H}U = e^{-S_2}\left(e^{-S_1}\tilde{H}e^{S_1}\right)e^{S_2}$$

where $S_1 = \left(x_{\mathbf{k}}b^{\dagger}_{\mathbf{k}} - x^{*}_{\mathbf{k}}b_{\mathbf{k}}\right) + \left(y_{\mathbf{k}}b^{\dagger}_{1S,\mathbf{k}} - y^{*}_{\mathbf{k}}b_{1S,\mathbf{k}}\right)$ eliminates the linear terms in $\left(b^{\dagger}_{\mathbf{k}} + b_{\mathbf{k}}\right)$. The transformation coefficients age given by

$$x_{\mathbf{k}} = \sqrt{N}\frac{\left(\mu^F E\right)\Delta}{\Delta\delta - \Gamma^2_{\mathbf{k}}},\ y_{\mathbf{k}} = \sqrt{N}\frac{\left(\mu^F E\right)\Gamma_{\mathbf{k}}}{\Delta\delta - \Gamma^2_{\mathbf{k}}}$$

The bilinear cross term $b^{\dagger}_{1S,\mathbf{k}}b_{\mathbf{k}} + b_{1S,\mathbf{k}}b^{\dagger}_{\mathbf{k}}$ can be diagonalized away through a rotation by $\phi_{\mathbf{k}}$ in Frenkel-Wannier-Mott exciton coordinate space [31] of the form:

$$S_2 = \phi_{\mathbf{k}}b_{1S,\mathbf{k}}b^{\dagger}_{\mathbf{k}} - \phi_{\mathbf{k}}b^{\dagger}_{1S,\mathbf{k}}b_{\mathbf{k}}$$

$$\tan\left(2\phi_{\mathbf{k}}\right) = \frac{2\Gamma_{\mathbf{k}}}{\delta - \Delta}$$

The overall diagonalized Hamiltonian has the form:

$$\begin{aligned}\left\{\frac{\delta+\Delta}{2}+\sqrt{\left(\frac{\delta-\Delta}{2}\right)^2+4\Gamma_{\mathbf{k}}^2}\right\}b_{1S,\mathbf{k}}^{\dagger}b_{1S,\mathbf{k}}+\\+\left\{\frac{\delta+\Delta}{2}-\sqrt{\left(\frac{\delta-\Delta}{2}\right)^2+4\Gamma_{\mathbf{k}}^2}\right\}b_{\mathbf{k}}^{\dagger}b_{\mathbf{k}}\end{aligned} \tag{2.2}$$

The factors in front of number operators $b_{1S,\mathbf{k}}^{\dagger}b_{\mathbf{k}}$ ($b_{\mathbf{k}}^{\dagger}b_{\mathbf{k}}$) represent the upper branch and lower branch of the hybrid at exact resonance between FE, WE and the photon $E_{1S}=E^F=\hbar\omega$. The resulting dispersion is illustrated on Fig.1.5 of the previous chapter [24].

Using this unitary transformation, the direct contribution of the exciton transition to the induced polarization per unit area of the interface is

$$P=\langle i|\,U^{-1}\left(\frac{\sqrt{N}}{S}\mu^F\left(b_{\mathbf{k}}+b_{\mathbf{k}}^{\dagger}\right)\right)U\,|i\rangle=\frac{N}{S}\frac{\left(\mu^F\right)^2\Delta}{\Delta\delta-\Gamma_{\mathbf{k}}^2}E \tag{2.3}$$

Here the initial state $|i\rangle$ corresponds to the FE exciton, as I neglected the quadrupole-light interaction. The hybrid life-time is introduced into the expression above through the complex part of the detunings $\delta\rightarrow\delta-i\hbar\gamma,\Delta\rightarrow\Delta-i\hbar\gamma$ as discussed above.

Also, due to the localization of the Frenkel non-resonant excitation, I take the FE into account as corrections to the local field. Assuming the organic to be an isotropic medium, one can write total electric field to be

$$E=E_{laser}+\frac{4\pi}{3}\left(\alpha_{res}+\alpha_{non-res}\right)E_{laser}$$

The second term represent the local field contribution, where $\alpha_{non-res}$ is the background polarizability (defined by non-resonant excitations in the organic) , while α_{res} is the direct exciton contribution to the polarizability corresponding to (2.3). The last equation can be rewritten as:

$$E = \frac{(\tilde{\varepsilon}+2)/3}{1-(4\pi\alpha_{res}/3)(\tilde{\varepsilon}+2)/3} E_{laser}$$

where the Lorentz-Lorenz relationship

$$\frac{4\pi}{3}\alpha_{non-res} = \frac{\tilde{\varepsilon}-1}{\tilde{\varepsilon}+2}$$

has been used. Thus, the local field corrections results in the exciton frequency shift $\delta \to \delta - \frac{4\pi}{3}\frac{N}{S}\left(\mu^F\right)^2\left[\frac{\tilde{\varepsilon}+2}{3}\right]$. The susceptibility is given by:

$$\chi = \frac{N}{S}\frac{\left(\mu^F\right)^2\Delta}{\Delta\delta - \Gamma_{\mathbf{k}}^2}$$

Taking into account that $N/S \approx 1/a_F^2$, the absorption coefficient is given by:

$$\Im\chi = \frac{f^F e^2\gamma\Delta^2\hbar}{2ca_F^2\left(\left(\delta\Delta-\Gamma_{\mathbf{k}}^2\right)^2+\gamma^2\Delta^2\hbar^2\right)\sqrt{\tilde{\varepsilon}}m_0} \tag{2.4}$$

Let me now make an important observation, that this absorption coefficient is fundamentally different from that for the case of the DDH [1]. In case of the QDH, one has $\hbar\gamma_F \gg \hbar\gamma_{hyb} \gg \hbar\gamma_1 S$ while for a dipole-dipole hybridization they are of the same order of magnitude. So, when $\Delta \to 0$ the absorption for the QDH is zero even for a smallest coupling.

For the QDH using the given absorption coefficient (2.4), the transmission through the sample of an arbitrary thickness (See Fig.1.1) can be written as:

$$Tr = 1 - \exp\left(-\frac{(\gamma\hbar\Delta)^2}{(\delta\Delta - \Gamma_{\mathbf{k}}^2)^2 + (\gamma\hbar\Delta)^2}\frac{z'}{l}\right) \tag{2.5}$$

Here z' can be viewed as the width of the narrow strip around the interface where the hybridization occurs and $l = \frac{\gamma\hbar c\sqrt{\epsilon_\infty}}{f^F E_F^2}$ is the hybrid absorption length.

Due to the big oscillator strength and narrow line width of the hybrid the absorption length l is extremely small. This is balanced out by the fact that the hybridization occurs only in a narrow strip around the interface between the organic and inorganic. The rest of the crystal is approximately transparent. So one can assume that the absorbing region is equal to the Bohr radius of the hybrid, i.e. $z' = a_B = 7$ $\mathring{A}$, therefore $z'/l \approx 1$. The value of the wave vector $\mathbf{k}$ is controlled by the oblique angle of incidence for the probe laser.

The "weak" interaction of the WE in the quantum well with the LA phonons leads to a red shift of the semiconductor energy gap and therefore to the red shift of the WE exciton band gap [27, 28, 29] and does not affect the binding energy of the $1S$ exciton [32] (See chapter 4 for more details). Hence, for small deviation of the exciton gas temperature from the helium

bath temperature one can consider the energy shift to be linear [25, 26]:

$$E^W(T) = E_{1S}(0) - \kappa(T - T_{bath}) \tag{2.6}$$

where $\kappa = 0.3\ \frac{\mu eV}{K}$.

The final temperature change given by the laser heating and helium cooling can be written as:

$$\frac{dT}{d\tau} = HP_{ex}[1 - \mathrm{Tr}(\tau, T)] - C[T - T_{bath}] \tag{2.7}$$

Here the phenomenologically introduced constants $H = 5.0 \times 10^6\ Ks^{-1}W^{-1}$ and $C = 2.8 \times 10^3\ s^{-1}$ giving the heating and cooling rate, respectively [26]. The transmission (2.5) depends on the temperature through the detuning $\Delta(T)$ according to the equation (2.6). The equilibrium temperature is given by the stationary solutions of the equation (2.7). This will govern the temperature and absorption bi-stability.

2.2 Numerical results and discussion

The QDH structure offers a more complicated picture of the nonlinear photo-thermal effect then just a slab of cuprous oxide itself. As it will be shown it is not a mere enhancement of the bi-stability effect but the appearance of two or more well pronounced bi-stability regions in temperature and transmission (absorption) spectra. In case of the QDH the photo-thermal rise of the

temperature leads not only to the red shift of the $1S$ exciton energy band but to an effective breaking of the resonance with the FE and reduction of the hybridization effect.

Many properties of the temperature, absorption and effective dispersion of the hybrid system can be obtained even before a numerical solution for the system of equations (2.6, 2.7). The right hand side of the equation (2.7) can be visualized as an implicit function of the temperature and detuning (See Fig.2.1). The actual temperature of the system depends on the way

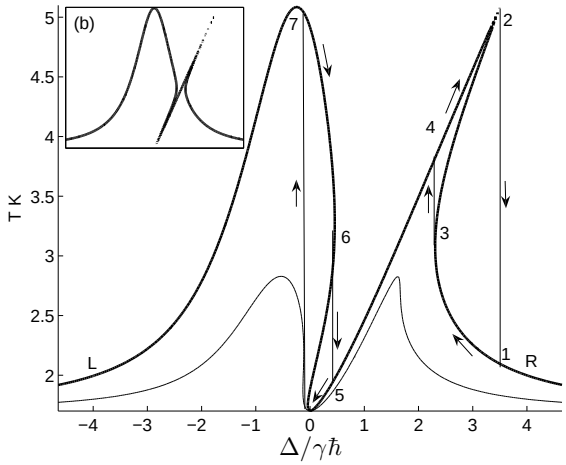

Figure 2.1: The temperature of the sample in K, versus the detuning in units of the hybrid exciton line- width $\gamma\hbar$. The coupling parameter is taken to be equal to the line width of the hybrid and the subplot (b) corresponds to the Stark reduced coupling. The thick solid curve corresponds to the laser intensity $P_{ex} = 3\ mWt$ and maximum temperature 5 K, and another thin curve stands for the intensity $P_{ex} = 1\ mWt$ and maximum temperature 2.5 K

one changes the frequency of the probe laser. If one lowers the frequency starting from the detuning 2 meV (point L on Fig.2.1) off resonance, then the system follows the path $R \to 1 \to 3 \to 4 \to 5 \to 0 \to 7 \to L$ to assure minimum temperature change with the changing detuning. If one increases the frequency starting from the detuning -2 meV (point R on the Fig.2.1), then the system follows the path $L \to 7 \to 6 \to 5 \to 4 \to 2 \to 1 \to R$.

On the other hand one can consider bi-stability as a possibility for the the system (2.6,2.7) to have more then one stationary solution. This non-linearity grows with P_{ex}. To illustrate the concept it is convenient to plot the heating and cooling rate as a function of the temperature. Then the stationary temperature is given as the intercept points (See Fig.2.2).

Now let me focus on the different branches of the hybrid. It is clear from the Fig.2.1 and Fig.2.3 that the response from two branches is asymmetrical. Further on I am going to refer to the lower branch as Wannier-like and to another as Frenkel-like. Both of them are defined by the interplay between the thermo-induced red shift of the WE exciton $\kappa\left(T - T_{bath}\right)$ and the excitation detuning Δ.

Indeed, the maximum of the absorption given by the poles of the expression (2.4):

$$2\delta_{\pm} = \kappa\left(T - T_{bath}\right) \pm \sqrt{\kappa^2\left(T - T_{bath}\right)^2 + 4\Gamma_k^2} \tag{2.8}$$

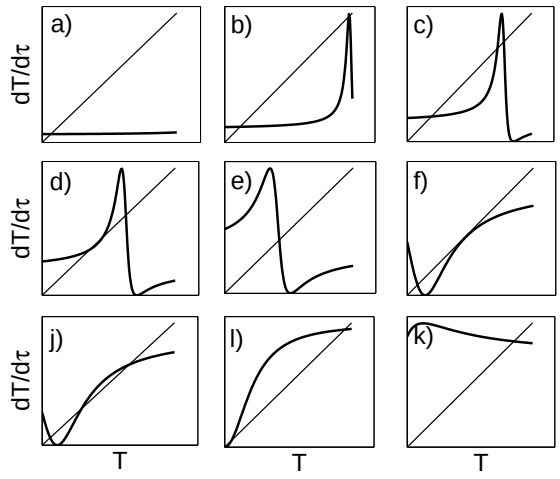

Figure 2.2: The numerical solution of the nonlinear equation (2.7) is given crossing of the cooling (straight line starting from the origin) and the detuning dependent photo-heating. The figure a)-k) correspond to the different laser detuning from the low temperature limit of the $1S$ quadrupole exciton as $\frac{\Delta}{\hbar\gamma} = 5;\ 3.7; ...; -0.8$ in units of the damping parameter.

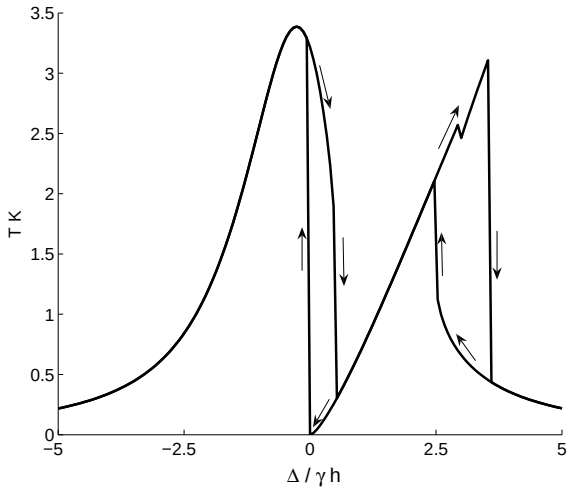

Figure 2.3: The numerical results for the temperature of the sample in K, versus the detuning in meV, $P_{ex} = 3\ mWt$. The coupling parameter is taken to be equal to the line width of the hybrid. The bi-stability is a result of multiple solutions and reveal itself as a sudden drop or raise in the temperature depending on the direction of the scan.

If the coupling between WE and FE is dominant: $\kappa^2 \left(T - T_{bath}\right)^2 \ll 4\Gamma_k^2$ then both branches are symmetrical and the maximum of absorption corresponds to the usual hybrid dispersion $\delta_{\pm} = \pm\Gamma_k$. Otherwise, strong asymmetry reveals itself. The case $\delta_+ \to \kappa \left(T - T_{bath}\right)$ defines the maximum of Wannier-like bi-stability, dominated by the temperature induced red shift. The Frenkel-like bi-stability corresponds to $\delta_- \to 0$ and is dominated by the hybridization effect.

For the up-scanned Wannier-like branch when the excitation energy δ catches up with the escaping exciton resonance δ_+ the actual temperature cut-off (Path $2 \to 1$ on the Fig.2.1 and Fig.2.2,(l)) occurs when the laser heating reaches its maximum $\delta_+ = \Delta$. When the excitation energy increases further the absorption reduces and the sample cools rapidly. On the down-scan the sample is cold even beyond the cut-off energy (the temperature is close to the lower cross-point on Fig.2.2,(l)).

In the same fashion the temperature rises rapidly on the Frenkel-like branch (Path $0 \to 7$ on the Fig.2.1 and Fig.2.2,(b))with a down-scan. The temperature goes down and the detuning between FE and WE reaches its minimum and an abrupt heating occurs. For the up-scan the sample is heated enough (close to the upper cross-point on Fig.2.2,(b)) to maintain large detuning between the FE and WE but drops down rapidly when the

FE and WE detuning reaches its maximum $\delta_{-} = \Delta$ (See Fig.2.2,(d)).

The bi-stability effect and the temperature rise of the hybrid is greatly enhanced (meV) compared to bulk cuprous oxide itself (μeV) mainly due to the fact of gaining oscillator strength from the organic part of the hybrid.

Numerical search for a stationary solution of equation (2.7) reveals a fine structure of the multiple bi-stability (See Fig.2.3, Fig.2.4). For the up-scan regime the distance between the solution branches $4 \rightarrow 2$ and $3 \rightarrow 2$ on the Fig. 2.1 can become smaller then $\kappa\,(T - T_{bath})$ and the temperature drops down on the branch $3 \rightarrow 2$. For the same reason when the intensity is big enough and the coupling between the FE and WE is reduced by the Stark effect fine structure can appear on the branches $5 \rightarrow 0$ and $6 \rightarrow 0$ on the down-scan. The model described above is valid for small temperature raise from the T_{bath} only. But it can be generalized for bigger temperature change by using a more elaborated non-linear temperature dependence of the WE exciton [29] and possible effect of the optical phonons [27]. Although, when one increases P_{ex} to the point when the density of the hybrid is close to the saturation density then other nonlinear effects due to exciton-exciton scattering and possible condensation start to play a considerable role. Such non-linear effects are presently under investigation.

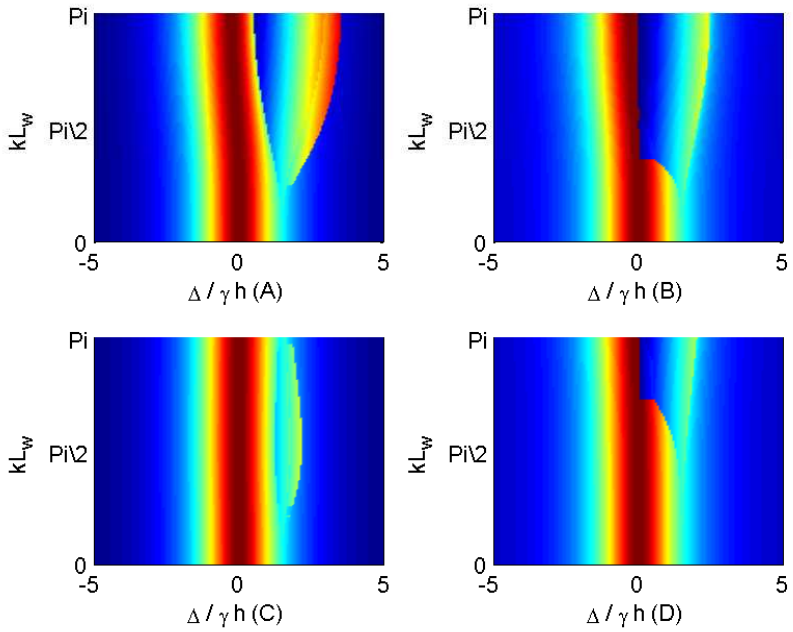

Figure 2.4: The temperature of the interface between organic DCM2:CA:PS and inorganic cuprous oxide QW for different detuning of the laser field from the energy of the $1S$ quadrupole exciton take at $T = T_b$ and different wave vectors k of the hybrid. The blue color corresponds to the temperature of the surrounding helium $1.7K$. The graphs represents the up (A) and down (B) laser scanning. The stark effect is taken into account on the up-scan (C) and down-scan (D) graphs.

Chapter 3

Enhanced second-harmonic generation

Considerable attention has been paid to the relatively strong optical second-harmonic generation (SHG) in thin films (D_{4h} symmetry) and bulk (O_h symmetry) of cuprous oxide crystals [30]. This effect is attributed to the electric-quadrupole $\hbar\omega_{1S} = 2.05\ eV$ exciton effect. The quadrupole exciton has very small oscillator strength but it possess rather narrow line-width $\hbar\gamma_{1S}$. So the effect is well pronounced when the exciting laser energy is close to one $\hbar\omega_{1S} - \hbar\omega \ll \hbar\gamma_{1S}$ or two photon resonance $\hbar\omega_{1S} - 2\hbar\omega \ll \hbar\gamma_{1S}$. In the dipole approximation this effect disappears [33].

In this chaper I propose to amplify the SHG characteristic of the $1S$ quadrupole exciton in cuprous oxide by making a hybrid with an organic FE. The idea of resonant enhancement of some non-linear properties generic to semiconductor dipole-allowed WE was presented in pioneering work of

Agranovich et. al. [1] for the layered organic-inorganic hetrostructures. It was also developed for quantum wires and dots embedded into organics [2, 34, 3, 35].

In previous chapter I demonstrated considerable enhancement of another non-linear effect in cuprous oxide, photo-thermal bi-stability [26, 25]. The calculated enhancement in the hysteresis-like region from μeV for bulk cuprous oxide to meV for the hybrid is due to the large oscillator strength of the hybrid exciton inherited from the organic part and still rather narrow line-width of the same order as the coupling. Analogous enhancement can be expected for the SHG.

3.1 Proposed SHG experimental set-up

The experiment I propose to reveal the enhancement of the SHG is closely related to the non linear absorption experiment described in the previous chapter. But it has a crucial difference in using of the probe signal. To study the bi-stability I made up and down-scan of the probe signal around the $1S$ quadrupole resonance in the cuprous oxide. To study the SHG one has to administer the probe signal to utilize multiple levels of the excitonic band in the cuprous oxide. The direction, polarization and number of required laser pulses is depended on the geometry of the proposed setup. In this chapter

I also adopt the concept of a layered organic-inorganic heterostructure but with some important changes suitable for the SHG. The inorganic component of the hybrid is a mono-layer of Cu_2O placed upon a thin film of the organic composite (See Fig.3.1). I take the width of this inorganic quantum well (L_w) is of the size of the cuprous oxide unit cell $a = 4.6\ \mathring{A}$. To provide

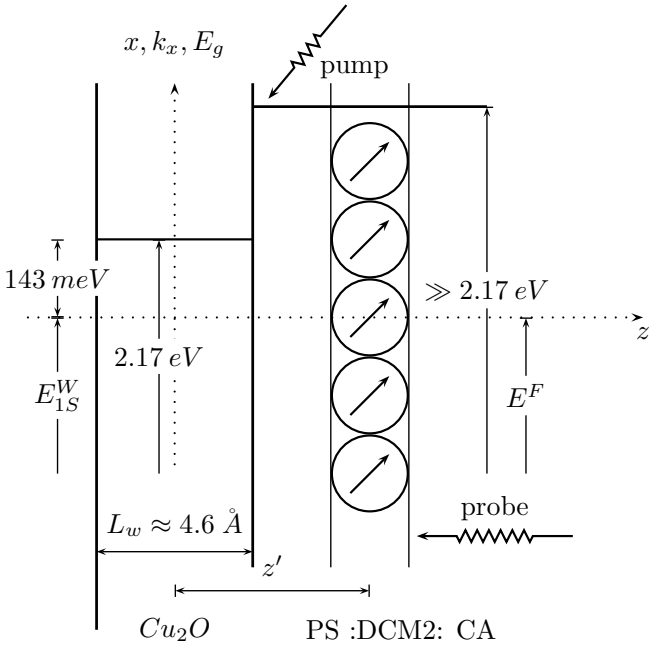

Figure 3.1: Schematic representation and the energy offset of a possible experimental set-up to observe the enhanced SHG by the quadrupole-dipole exciton. Here the inorganic Cu_2O quantum well provides the $1S$ quadrupole WE. The DCM2 part of the organic "solid state solute" provides dipole allowed FE (set of small arrows); the PS host prevents wave function overlapping between organic and inorganic excitons; CA under proper concentration allows tuning of the excitons into the resonance.

resonance between WE in cuprous oxide and FE in the organic, I proposed

utilization of 'solid state solvation' (SSS) of the DCM2 [1] molecules in transparent polystyerine (PS) host doped with camorphic anhydride (CA) as it was described in previous chapters.

The SSS is a type of solvatochromism manifesting itself as some change in the spectral position of the absorption/luminescence band due to change in the polarity of the medium. The Förster dipole-dipole non-resonant interaction between DCM2 and CA modifies the energy structure of the involved molecules.

During the "slow" phase ($\tau_s \approx 3.3\,ns$) the energy of the FE [2] experiences a red shift linear with the CA concentration due to non-resonant dipole-dipole interaction with the CA molecules. The red spectral shift of the FE energy in resonance with the quantum confined 1S quadrupole exciton can be accomplished with corresponding CA concentration.

This resonant coupling gives rise to the upper and lower branches of the quadrupole-dipole hybrid (QDH) dispersion: $\hbar\omega_{u,l} = \hbar\omega_{1S} \pm \Gamma_{\mathbf{k}}$. To populate both of the branches one needs a second pumping photon tuned into resonance with the $1S$ transition.

The radiation field interacts through both dipole and quadrupole part of

[1] [2-methyl-6-2-(2,3,6,7-tetrahydro-1H, 5H - benzo[i,j] - quinolizin - 9 - yl) - ethenyl] - 4H - pyran - 4 - ylidene] propane dinitritle.

[2] in my case I define the FE as DCM2 excitation

the hybrid. The dipole interaction can be utilized to produce linear response signal due to the pumping [25]. By using the non-linear response to the probe signal, the second harmonic can be generated through the quadrupole part of the hybrid. Different SHG regimes can be achieved by changing the timing between pumping and probe signals (See section 3.3 for more details).

According to the selection rules for the quadrupole-dipole hybrid the pumping signals have to run along the organic-inorganic interface of the heterostructure and have linear polarization in the z direction [24]. To maximize second order non-linear response in the cuprous oxide the probe signal has to be perpendicular to the interface with the polarization $\mathbf{e}_i$ along the x direction (See Fig.3.1).

The net polarization is given by a second rank tensor through the following expression:

$$P_z^{(1)} + P_x^{(2)} = \chi_{i,z}^{(1)} E_i + i\chi_{i,j,x}^{(2)} k_x E_i E_j \tag{3.1}$$

Here E_i, E_j are the electric field of the pumping and prob lasers correspondingly. The x component of the probe signal wave vector is taken to be close to zero to avoid possible interference in momentum conservation.

In this chapter I develop both classical and quantum mechanical models, which can be used to find a specific form of the hybrid second order nonlinear susceptibility. In the next section 3.2 I demonstrate that the second order

non linearity generic to the cuprous oxide and introduced through a small parameter $\tilde{\lambda}$ is enhanced due to the QDH with the organic (See (3.4)). In section 3.3 I develop quantum theory of the enhanced SHG. It allows investigation of different regimes of the process. I generalize the concept of the double-sided Feynman diagrams [31] to include non radiative processes of the energy exchange between DCM2 and CA as well as resonant QDH between DCM2 and cuprous oxide.

3.2 Anharmonic coupled oscillators model

Due to the small radius of both the WE and FE exciton part of the hybrid one can neglect the effect of confinement. Likewise, in this classical model I neglect the non-local effects of the linear $\chi^{(1)}_{i,z}$ and non-linear susceptibility $\chi^{(2)}_{i,j,x}$.

Therefore, as a first step, I will use the simplest model to describe the hybrid SHG. Namely, I adopt an extension of the anharmonic oscillator model [36, 31] generalized for the case of resonant coupling between two distinct sets of oscillators. This simplified picture only covers the case when the pumping field excites the FE and WE is probed.

I consider the WE in cuprous oxide as an assembly of the oscillators with the oscillator strength per unit cell given by $f_{xz,k} \propto k$ (See for example

reference [19]). The second set of the oscillators with the oscillator strength given by f^F corresponds to the FE in the organic.

Treating the wave vector k as just another parameter [3], the polarization P^W, P^F due to WE and FE can be written in terms of the effective electron-hole displacements X, Y as:

$$P^W = \frac{N}{a_B S} f_{xz,k} eX \ , \ P^F = \frac{\rho_{DCM2} N}{a_B S} f^F eY \tag{3.2}$$

Here S is the area of the interface. The surface density of the WM and FE excitons are $Nf_{xz,k}/\left(a_B S\right)$ and $\rho_{DCM2} N f^F/\left(a_B S\right)$ correspondingly and N is the total number of the oscillators. Here I also took into account the low density ($\rho_{DCM2} = 0.05\%$) of the DCM2 molecules in the organic to avoid the agregation effect [4].

The terms proportional to γ describe the QDH damping. The terms proportional to $2\omega_{1S}\Gamma_k/\hbar$ describe the quadrupole-dipole coupling. Hence, the eigenvalues of the linearized system of equations (3.3) give both branches of the QDH.

The system is driven dominantly by the light-dipole interaction in the organic and the quadrupole-light interaction is neglected (m is the electron mass).

[3] In the text I am going to omit index k unless I put an emphasis on it

In the timeframe of the hybridization $\tau_s - \tau_h < t < \tau_s$, the system of equations governing the oscillators dynamics can be written in the form:

$$\begin{aligned} \ddot{X} + \omega_{1S}^2 X + \gamma \dot{X} - \frac{2\omega_{1S}\Gamma_k}{\hbar} Y - \omega_{1S}^2 \tilde{\lambda} X^2 = 0 \\ \ddot{Y} + \omega_{1S}^2 Y + \gamma \dot{Y} - \frac{2\omega_{1S}\Gamma_k}{\hbar} X = \frac{e}{m} E_i e^{i\omega t} \end{aligned} \tag{3.3}$$

The nonlinear factor $\omega_{1S}^2 \tilde{\lambda}$ appears due to the probe signal. It is defined such that $\tilde{\lambda}$ has dimensions of reciprocal length and is considered to be small in a sense that it is much less than the reciprocal of the maximum displacement of FE (Y) and WE (X) oscillator. The exact value of λ can be obtained either from an experiment or from the microscopic quantum theory (See next section for more details).

Using standard perturbation theory with respect to the small parameter $\tilde{\lambda}$ in zero order (neglecting the quadratic term) and combining equations (3.1,3.2,3.3) one has the linear response of the hybrid and bulk cuprous oxide given by the following expressions:

$$\chi^{(1)}(\omega) = \frac{\rho_{DCM2} N}{a_B S} \frac{f^F e^2/m \left(\omega_{1S}^2 - \omega^2 + i\omega\gamma\right)}{\left(\omega_{1S}^2 - \omega^2 + i\omega\gamma\right)^2 - \left(2\omega_{1S}\Gamma_k/\hbar\right)^2}$$

$$\chi^{(1)}(\omega) = \frac{N}{a_B S} \frac{f_{xz,k} e^2/m}{\omega_{1S}^2 - \omega^2 + i\gamma}$$

Including the nonlinear term as a source for the SHG to first order in the

perturbation parameter, there is a displacement at 2ω. The SHG response is given by a solution of the following system:

$$\ddot{X} + \omega_{1S}^2 X + \gamma\dot{X} - \frac{2\omega_{1S}\Gamma_k}{\hbar}Y - \omega_{1S}^2\tilde{\lambda}X_{\tilde{\lambda}=0}^2 = 0$$
$$\ddot{Y} + \omega_{1S}^2 Y + \gamma\dot{Y} - \frac{2\omega_{1S}\Gamma_k}{\hbar}X = 0$$

Using the definitions (3.1) and (3.2) one gets the following non-linear second order response function for the hybrid and bulk cuprous oxide correspondingly:

$$\chi^{(2)}(2\omega;\omega,\omega) = \frac{\rho_{DCM2}N}{a_B S} \times$$
$$\frac{f^F e^3/m^2\omega_{1S}^2\tilde{\lambda}\left(2\omega_{1S}\Gamma_k/\hbar\right)\left(\omega_{1S}^2 - \omega^2 + i\omega\gamma\right)^2}{\left(\left(\omega_{1S}^2 - (2\omega)^2 + i2\omega\gamma\right)^2 - \left(2\omega_{1S}\Gamma_k/\hbar\right)^2\right)^2\left(\left(\omega_{1S}^2 - \omega^2 + i\omega\gamma\right)^2 - \left(2\omega_{1S}\Gamma_{\mathbf{k}}/\hbar\right)^2\right)}$$
$$\chi^{(2)}(2\omega;\omega,\omega) =$$
$$= \frac{N}{a_B S}\frac{f_{xz,k}e^3/m^2\omega_{1S}^2\tilde{\lambda}}{\left(\omega_{1S}^2 - (2\omega)^2 + i2\gamma\right)\left(\omega_{1S}^2 - \omega^2 + i\gamma\right)^2}$$

3.3 Quantum theory of the quadrupole-dipole hybrid SHG

Although the system of non-linear susceptibilities above, in principle solves the problem of SHG due to the hybrid it does not clarify the origin of the nonlinearity $\tilde{\lambda}$. Hence, in this section I propose a unified quantum theory of the hybrid SHG.

The linear response of the hybrid is due to dipole transitions from the ground $|g\rangle$ state [4] to the FE $|F\rangle$ in the organic and due to quadrupole transitions to the WE $|1S\rangle$ in the cuprous oxide. The non-linearities are the result of some intermediate inter-band transitions in the cuprous oxide [31].

In cuprous oxide the nearest state in energy to $\hbar\omega_{1S}$ is the $\hbar\omega_{2P}$ dipole allowed excitonic band $|2P\rangle$, $E_g > \hbar\omega_{2P} > \hbar\omega_{1S}$. Hence it plays the main role in formation of the non-linear response and can be excited by the properly tuned probe signal. I neglect all the rest of inter-band and intra-band [5] transitions. Therefore, the states above form a complete basis for the SHG problem:

$$|g\rangle\,,\ |1S\rangle\,,\ |F\rangle\,,\ |2P\rangle \tag{3.4}$$

Inversion symmetry of the DCM2 is also broken by the CA induced local field and the interface effect. Therefore, unlike in classical model, the contribution from the organic to the SHG has to be consider as well. But due to the smallness of the symmetry breaking local field it contributes a little to the SHG enhancement.

Using the basis above let me introduce creation operators for the FE and the $1S$ and the $2P$ WE exciton $b^\dagger = |F\rangle\langle g|$, $B^\dagger_{1S} = |1S\rangle\langle g|$, $B^\dagger_{2P} = |2P\rangle\langle g|$

[4] when no excitations are present in the system
[5] due to small radius of the quadrupole WE

respectively. The commutation algebra of the operators is presented below:

$$\left[B_{1S}^{\dagger}, B_{1S}\right] = -1 + B_{2P}^{\dagger}B_{2P} + b^{\dagger}b \quad \left[B_{1S}^{\dagger}, B_{2P}\right] = B_{1S}^{\dagger}B_{2P} \quad \left[B_{2P}^{\dagger}, B_{1S}\right] = B_{2P}^{\dagger}B_{1S}$$
$$\left[B_{2P}^{\dagger}, B_{2P}\right] = -1 + B_{1S}^{\dagger}B_{1S} + b^{\dagger}b \qquad \left[b^{\dagger}, B_{1S}\right] = b^{\dagger}B_{1S} \qquad \left[b^{\dagger}, B_{2P}\right] = b^{\dagger}B_{2P}$$
$$\left[b^{\dagger}, b\right] = -1 + B_{2P}^{\dagger}B_{2P} + B_{1S}^{\dagger}B_{1S} \qquad \left[B_{1S}^{\dagger}, b\right] = B_{1S}^{\dagger}b \qquad \left[B_{2P}^{\dagger}, b\right] = B_{2P}^{\dagger}b$$

The net polarization of the sample is defined as [31]:

$$\begin{aligned} P = {} & \mu_{1S,k}\left(B_{1S}^{\dagger} + B_{1S}\right) + \mu_{2P}\left(B_{2P}^{\dagger} + B_{2P}\right) \\ & + \mu_{F}\left(b^{\dagger} + b\right) + \mu_{1S,2P}\left(B_{1S}^{\dagger}B_{2P} + B_{1S}B_{2P}^{\dagger}\right) \end{aligned} \tag{3.5}$$

Here $\mu_{1S,k} = \mathbf{e}_i \cdot \mathbf{k}_x \cdot Q_{x,z} = 3 \cdot 10^{-5}(k_x/k_{0,x})\ D$ [6] is an effective dipole moment [19, 24] due to the quadrupole transitions associated with the oscillator strength; $k_0 = 2.62 \times 10^5\ cm^{-1}$ is the resonant wave vector for bulk cuprous oxide; the unit vector of the *pumping* field polarization is $\mathbf{e}_i$. The dipole moment of the transitions from $|1S\rangle$ to $\langle 2P|$ is defined by [37, 9]:

$$\mu_{1S,2P}^2 = \frac{Ne^2\hbar^2 f_{2P}}{Sa_B 2mE_{2P}}\left(\mathbf{e}_j \times \mathbf{k}_{0,x}/k_{0,x}\right)^2 = 6 \cdot 10^{-3}\ D^2$$

Here $\mathbf{e}_i$ is the unit vector of the *probe* field polarization Finally, the DCM2 dipole moment of the transition from $|g\rangle$ to $\langle F|$ per unit area of the interface is given by [38]:

$$\mu_F^2 = \frac{\rho_{DCM2}Ne^2\hbar^2 f^F}{Sa_B 2m\hbar\omega_{1S}} = 0.2\ D^2$$

[6] D stands for Debye

Using equation (3.5) the total Hamiltonian can be written as:

$$H = E^F b^\dagger b + \hbar\omega_{1S} B_{1S}^\dagger B_{1S} + E_{2P} B_{2P}^\dagger B_{2P} + \Gamma_{\mathbf{k}} \left(B_{1S}^\dagger b + B_{1S} b^\dagger \right) + \\ + \mu^F \left(b^\dagger E_i^\dagger + b E_i \right) + \mu_{1S,k} \left(B_{1S}^\dagger E_i^\dagger + B_{1S} E_i \right) + \mu_{2P} \left(B_{2P}^\dagger E_i^\dagger + B_{2P} E_i \right) + \\ + \mu_{1S,2P} \left(B_{1S}^\dagger B_{2P} E_j^\dagger + B_{1S} B_{2P}^\dagger E_j \right) \tag{3.6}$$

The corresponding Hysenberg equations up to the second order in the creation and annihilation operators are:

$$\begin{aligned}
i\hbar \frac{dB_{1S}^\dagger}{dt} &= \hbar\omega_{1S} B_{1S}^\dagger + \Gamma_k b^\dagger - \mu^F E_i B_{1S}^\dagger b + \mu_{1S,k} E_i \left(1 - B_{2P}^\dagger B_{2P} - b^\dagger b \right) \\
&\quad - \mu_{2P} E_i B_{1S}^\dagger B_{2P} + \mu_{1S,2P} E_j B_{2P}^\dagger \\
i\hbar \frac{dB_{1S}}{dt} &= -\hbar\omega_{1S} B_{1S} - \Gamma_k b + \mu^F E_i^\star b^\dagger B_{1S} - \mu_{1S,k} E_i^\star \left(1 - B_{2P}^\dagger B_{2P} - b^\dagger b \right) \\
&\quad + \mu_{2P} E_i^\star B_{2P}^\dagger B_{1S} - \mu_{1S,2P} E_j^\star B_{2P} \\
i\hbar \frac{dB_{2P}^\dagger}{dt} &= \hbar\omega_{2P} B_{2P}^\dagger - \mu^F E_i B_{2P}^\dagger b - \mu_{1S,k} E_i B_{2P}^\dagger B_{1S} + \\
&\quad \mu_{2P} E_i \left(1 - B_{1S}^\dagger B_{1S} - b^\dagger b \right) + \mu_{1S,2P} E_j B_{1S}^\dagger \\
i\hbar \frac{dB_{2P}}{dt} &= -\hbar\omega_{2P} B_{2P} + \mu^F E_i^\star b^\dagger B_{2P} + \mu_{1S,k} E_i^\star B_{1S}^\dagger B_{2P} - \\
&\quad \mu_{2P} E_i^\star \left(1 - B_{1S}^\dagger B_{1S} - b^\dagger b \right) - \mu_{1S,2P} E_j^\star B_{1S} \\
i\hbar \frac{db^\dagger}{dt} &= E^F b^\dagger + \Gamma_k B_{1S}^\dagger + \mu^F E_i \left(1 - B_{1S}^\dagger B_{1S} - B_{2P}^\dagger B_{2P} \right) \\
&\quad - \mu_{1S,k} E_i b^\dagger B_{1S} - \mu_{2P} E_i b^\dagger B_{2P} \\
i\hbar \frac{db}{dt} &= -E^F b - \Gamma_k B_{1S} - \mu^F E_i^\star \left(1 - B_{1S}^\dagger B_{1S} - B_{2P}^\dagger B_{2P} \right) + \\
&\quad \mu_{1S,k} E_i^\star B_{1S}^\dagger b + \mu_{2P} E_i^\star B_{2P}^\dagger b
\end{aligned}$$

In the exact resonance between FE and WE excitons $\hbar\omega_{1S} = E^F$ the linear approximation is straightforward. The creation operators are proportional to $\propto e^{i\omega t}$ and the system above is reduced to:

$$\begin{aligned}
\hbar\omega B^{\dagger}_{1S,0} &= \left(\hbar\omega_{1S} - i\hbar\gamma\right) B^{\dagger}_{1S,0} + \Gamma_k b^{\dagger}_0 + \mu_{1S,k} E_i \\
-\hbar\omega B_{1S,0} &= -\left(\hbar\omega_{1S} + i\hbar\gamma\right) B_{1S,0} - \Gamma_k b_0 - \mu_{1S,k} E^{\star}_i \\
\hbar\omega B^{\dagger}_{2P,0} &= \hbar\omega_{2P} B^{\dagger}_{2P,0} + \mu_{2P} E_i \\
-\hbar\omega B_{2P,0} &= -\hbar\omega_{2P} B_{2P,0} - \mu_{2P} E^{\star}_i \\
\hbar\omega b^{\dagger}_0 &= \left(\hbar\omega_{1S} - i\hbar\gamma\right) b^{\dagger}_0 + \Gamma_k B^{\dagger}_{1S,0} + \mu^F E_i \\
-\hbar\omega b_0 &= -\left(\hbar\omega_{1S} + i\hbar\gamma\right) b_0 - \Gamma_k B_{1S,0} - \mu^F E^{\star}_i
\end{aligned}$$

The system above has a solution:

$$\begin{aligned}
B^{\dagger}_{2P,0} &= \frac{\mu_{2P} E_i}{\hbar\omega - \hbar\omega_{2P}} \\
B^{\dagger}_{1S,0} &= \frac{\mu_{1S} E_i \left(\hbar\omega - \hbar\omega_{1S} + i\hbar\gamma\right) + \mu^F \Gamma_k E_i}{\left(\hbar\omega - \hbar\omega_{1S} + i\hbar\gamma\right)^2 - \Gamma_k^2} \\
b^{\dagger}_0 &= \frac{\mu^F E_i \left(\hbar\omega - \hbar\omega_{1S} + i\hbar\gamma\right) + \mu_{1S} \Gamma_k E_i}{\left(\hbar\omega - \hbar\omega_{1S} + i\hbar\gamma\right)^2 - \Gamma_k^2}
\end{aligned} \tag{3.7}$$

The linear response from two branches may be observed by pumping the hybrid with two signals $E_j||E_i||z \propto e^{i\omega t}$. The first photon $\hbar\omega = E_{DCM2}$ excites DCM2 molecules. During the time period $\tau_s - \tau_h$ the system relaxes to the FE exciton energy close to $\hbar\omega_{1S}$ thus providing resonance between WE and FE. Then the second pumping photon $\hbar\omega = \hbar\omega_{1S}$ enters and excites quadrupole

WE so that both QDH branches are populated. The QDH exciton lives for τ_h nano-seconds and then both branches of the hybrid relaxes to the ground state emitting photons of the energy $\hbar\omega_{1S} \pm \Gamma_k$.

Generalizing conventional double-sided Feynman diagrams [31] to include the non-radiative processes, the linear response from the QDH can be represented by the following diagram:

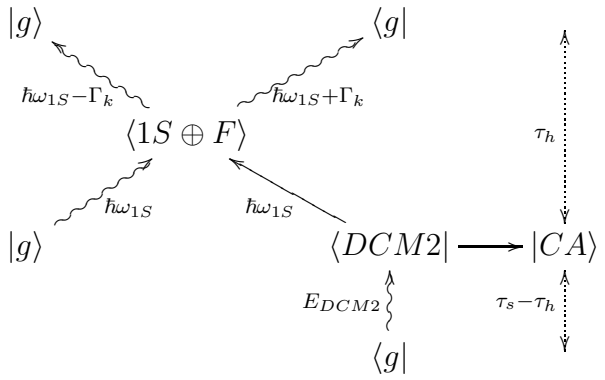

(3.8)

$$\chi_i^{(1)}(\omega) = \frac{\mu_F^2(\hbar\omega - \hbar\omega_{1S} + i\hbar\gamma) + \mu_F\mu_{1S}\Gamma_k}{(\hbar\omega - \hbar\omega_{1S} + i\hbar\gamma)^2 - \Gamma_k^2}$$

On the diagram the wavy lines represent the incoming and outgoing photons; the straight lines stand for the non-radiative transitions. The diagram shows energy exchange between photon-exciton and exciton-exciton as well as the time separation between two pumping signals. Time increases from bottom to the top of the diagram as for the conventional Feynman diagram. The hybrid life time is denoted as $\tau_h = 1/\gamma$ and the hybridization between FE and WE is denoted as $\oplus$.

In the derivation of the linear response $\chi_i^{(1)}(\omega)$ I used equation (3.5) along with linear solutions of the Heisenberg equations of motion (3.7). Formally the linear response can be written in terms of the hybrid Green's functions as:

$$\chi_i^{(1)}(\omega) = \sum_{a,b=\{g,1S,F\}} \mu_{ab}\mu_{ba} I_{ab}(\omega)$$

$$I_{1S,g} = I_{F,g} = \frac{\hbar\omega - \hbar\omega_{1S} + i\hbar\gamma}{(\hbar\omega - \hbar\omega_{1S} + i\hbar\gamma)^2 - \Gamma_k^2}$$

$$I_{1S,F} = \frac{\Gamma_k}{(\hbar\omega - \hbar\omega_{1S} + i\hbar\gamma)^2 - \Gamma_k^2}$$

Here the dipole matrix elements in the corresponding basis (3.4) are given by [7]:

$$\begin{pmatrix} 0 & \mu_{1S} & \mu_F & 0 \\ \mu_{1S} & 0 & \sqrt{\mu_{1S}\mu_F} & 0 \\ \mu_F & \sqrt{\mu_F\mu_{1S}} & 0 & 0 \\ 0 & 0 & 0 & 0 \end{pmatrix}$$

[7] I neglected the non-resonant term associated with the ground state dipole moment of the organic μ_g

The SHG is due to second order response $E_j \perp E_i || z$ is proportional to $\propto e^{i2\omega t}$:

$$
\begin{aligned}
2\hbar\omega B^{\dagger}_{1S,1} &= \left(\hbar\omega_{1S} - i\hbar\gamma\right) B^{\dagger}_{1S,1} + \Gamma_k b^{\dagger}_1 + \mu_{1S,2P} E_j B^{\dagger}_{2P,0} \\
2\hbar\omega B_{1S,1} &= \left(\hbar\omega_{1S} + i\hbar\gamma\right) B_{1S,1} + \Gamma_k b_1 + \mu_{1S,2P} E^{\star}_j B^{\dagger}_{2P,0} \\
2\hbar\omega B^{\dagger}_{2P,1} &= \hbar\omega_{2P} B^{\dagger}_{2P,1} + \mu_{1S,2P} E_j B^{\dagger}_{1S,0} \\
2\hbar\omega B_{2P,1} &= \hbar\omega_{2P} B_{2P,1} + \mu_{1S,2P} E^{\star}_j B^{\dagger}_{1S,0} \\
2\hbar\omega b^{\dagger}_1 &= \left(\hbar\omega_{1S} - i\hbar\gamma\right) b^{\dagger}_1 + \Gamma_k B^{\dagger}_{1S,1} \\
-2\hbar\omega b_1 &= -\left(\hbar\omega_{1S} + i\hbar\gamma\right) b_1 - \Gamma_k B_{1S,1}
\end{aligned}
$$

The system has a solution:

$$
\begin{aligned}
B^{\dagger}_{2P,1} &= \frac{\mu_{1S,2P} E_j B^{\dagger}_{1S,0}}{2\hbar\omega - \hbar\omega_{2P}} \\
B^{\dagger}_{1S,1} &= \frac{\mu_{1S,2P} E_j \left(2\hbar\omega - \hbar\omega_{1S} + i\hbar\gamma\right) B^{\dagger}_{2P,0}}{\left(2\hbar\omega - \hbar\omega_{1S} + i\hbar\gamma\right)^2 - \Gamma_k^2} \\
b^{\dagger}_1 &= \frac{\mu_{1S,2P} E_j \Gamma_k B^{\dagger}_{2P,0}}{\left(2\hbar\omega - \hbar\omega_{1S} + i\hbar\gamma\right)^2 - \Gamma_k^2}
\end{aligned}
\tag{3.9}
$$

The first type of the SHG is formed when the branches of the hybrid interacts with the $|2P\rangle$ level excited by the probe signal. Using all the diagram conventions I adopted above, the diagram for this non linear process is given

below:

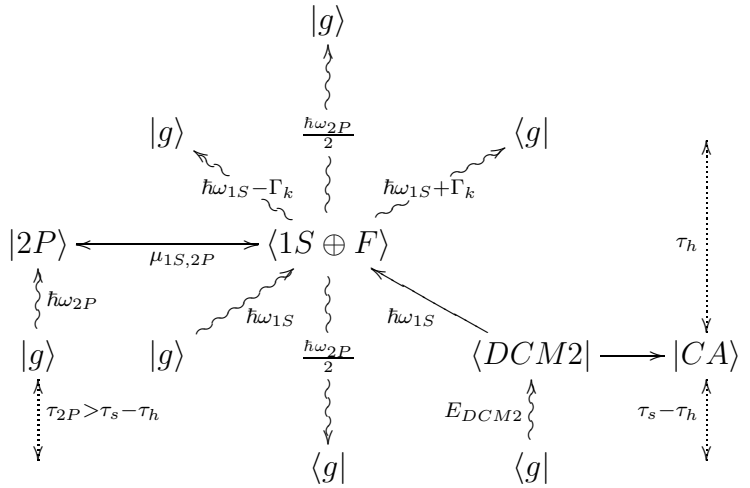

$$\chi^{(2)}_{ij}\left(2\omega;\omega,\omega\right)=\frac{\mu_{2P}\mu_{1S,2P}\left(\mu_{1S}\left(\hbar\omega-\hbar\omega_{1S}+i\hbar\gamma\right)+\mu_F\Gamma_k\right)}{\left(2\hbar\omega-\hbar\omega_{2P}\right)\left(\left(\hbar\omega-\hbar\omega_{1S}+i\hbar\gamma\right)^2-\Gamma_k^2\right)} \tag{3.10}$$

Here the probe signal comes *after* the hybrid is formed: $\tau_{2P} > \tau_s - \tau_h$.

Another second order non linear response can be formed if the probe signal is coming *before* the hybridization $\tau_{2P} < \tau_s - \tau_h$. It can be represented

by the following diagram:

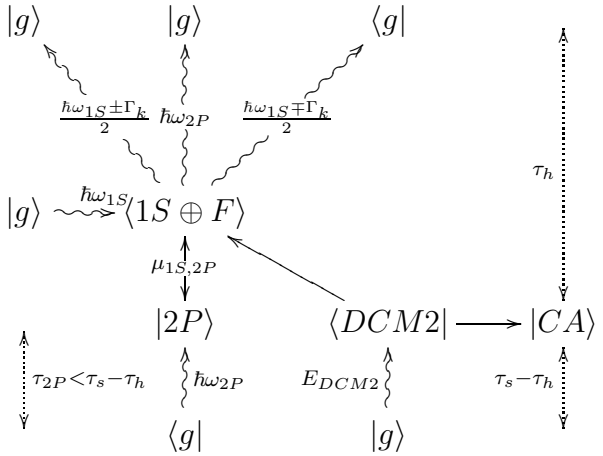

$$\chi_{ij}^{(2)}\left(2\omega;\omega,\omega\right)=\frac{\mu_{2P}\mu_{1S,2P}\left(\mu_{1S}\left(2\hbar\omega-\hbar\omega_{1S}+i\hbar\gamma\right)+\mu_F\Gamma_k\right)}{\left(\hbar\omega-\hbar\omega_{2P}\right)\left(\left(2\hbar\omega-\hbar\omega_{1S}+i\hbar\gamma\right)^2-\Gamma_k^2\right)} \tag{3.11}$$

The Green's function representation of the SHG due to the second order response is given by the following expression:

$$\chi_{ij}^{(2)}\left(2\omega;\omega,\omega\right)=$$

$$\mu_{1S,2P}\sum_{a=\{g,1S,F,2P\}}\mu_{a,1S}\mu_{2P,a}\left[I_{a,1S}\left(\omega\right)I_{a,2P}\left(2\omega\right)+I_{1S,a}\left(2\omega\right)I_{2P,a}\left(\omega\right)\right]$$

$$I_{2P,g}=\frac{1}{\hbar\omega-\hbar\omega_{2P}}$$

The dipole matrix elements on the basis (3.4) are given by:

$$\begin{pmatrix} 0 & \mu_{1S} & \mu_F & \mu_{2P} \\ \mu_{1S} & 0 & \sqrt{\mu_{1S}\mu_F} & \mu_{1S,2P} \\ \mu_F & \sqrt{\mu_F\mu_{1S}} & 0 & 0 \\ \mu_{2P} & \mu_{1S,2P} & 0 & 0 \end{pmatrix}$$

According to the last term in the equation (3.5), the signal at $2\hbar\omega=\hbar\omega_{1S}\pm\Gamma_k$

may generate the signal at $\hbar\omega = \hbar\omega_{1S} \pm \Gamma_k$:

$$\chi_{ij}^{(3)}(\omega; 2\omega, -\omega) = \frac{\mu_{2P}\mu_{1S,2P}^2 (2\hbar\omega - \hbar\omega_{1S} + i\hbar\gamma)}{(\hbar\omega - \hbar\omega_{2P})^2 \left((2\hbar\omega - \hbar\omega_{1S} + i\hbar\gamma)^2 - \Gamma_k^2\right)}$$

This type of signal has been experimentally detected [30] in bulk cuprous oxide ($\Gamma_k = 0$) when the pumping signal was tuned to the wave length between 12285 $\mathring{A}$ and 12195$\mathring{A}$. A strong SH signal was detected at 6096 $\mathring{A}$ which has to be attributed not only to the narrow line-width of the quadrupole exciton but to the fact that $\mu_{1S,2P} \gg \mu_{1S}$ as well. From the last expression it follows that in this case no increment in the outgoing signal can be expected due to the hybridization effect.

The third order nonlinearity is responsible as well for some small contribution to the SHG due to the non-zero ground state dipole moment of the DCM2 molecules [39]. In the local electric field created by the polar CA molecules on the interface $E_{loc}(0)$,the SH signal is due to the third order susceptibility $\chi_{ij}^{(3)}(2\omega; \omega, \omega, 0)$. The exact expression in terms of the corresponding Green's functions is too lengthy to be listed here [31], therefore I provide numerical calculations of the total SHG including the above correction in the next section.

3.4 Numerical results and discussion

In order to make a numerical comparison of the hybrid and bulk SHG the life-time of the hybrid plays a major role. Considering the bi-stability effect in the hybrid [25] I assumed that the cuprous oxide has purity of 99.99% with the reported line-width of $\hbar\gamma_{1S} = 0.1\ meV$ (pico-second lifetime) [30]. Therefore the hybrid life-time is dominated by its inorganic part $\hbar\gamma \approx \hbar\gamma_{1S}$. To compensate for such big line-width I also assumed that the DCM2 is presented as a thin film embeded into PS host close to the interface with the cuprous oxide. For the non-linear absorption experiment described in previous chapter this assumption is justified as it makes the absorption length of the hybrid equal to the narrow region around the interface, of the size of the hybrid itself. But there is a drawback in that model due to possible agregation of the DCM2.

Hence in this chapter I adopted the picture of disordered organic and higher purity of the inorganic crystal. This will bring the line-width and the coupling parameter to the same order. For pure cuprous oxide crystal the life-time of the quadrupole $1S$ exciton is reported to be $\tau_{1S} = 1.7 \ldots 3.0\ ns$ ($\hbar\gamma = 1 \ldots 0.5\ \mu eV$) [26, 8, 9]. Such crystals and thin films are widely used in searching for BEC of excitons.

In this case the life-time of the $1S$ quadrupole exciton is mainly determined by the ortho-para exciton conversion. The life-time of the organic part of the hybrid is determined by the time the excited DCM2 molecule reaches an equilibrium with the bath of polar CA molecules. The life-time for the given concentration of the CA is reported to be 3.3 ns [4, 38]. Because these processes are of the same order, the effective life-time of the hybrid is a non-trivial combination of the effects described above and will be reported elsewhere. Here I assume the simplest case of non-coherent life-time of the hybrid $\hbar\gamma = 0.29\ \mu eV$ [24].

The intensity of the second-harmonic is proportional to $\left|\chi^{(2)}k_x\right|^2$ [40]. Therefore an important measurable quantity is a relative value of nonlinear susceptibility $\left|\chi^{(2)}k_x\right|$ presented in Fig.3.2.

The SHG signal is split according to the response from the lower and upper branch of the hybrid. Asymmetry between this two branches is a result of quantum effects and not present in the classical anharmonic oscillator picture. I also included the corrections due to interface effect in the organic in my numerical simulation.

For the sake of simplicity let me consider two distinct cases. First, the pump laser is perpendicular to the interface. The states up to $ka = k_0 a$ are populated thermally. No hybridization occurs and it is equivalent to the bulk

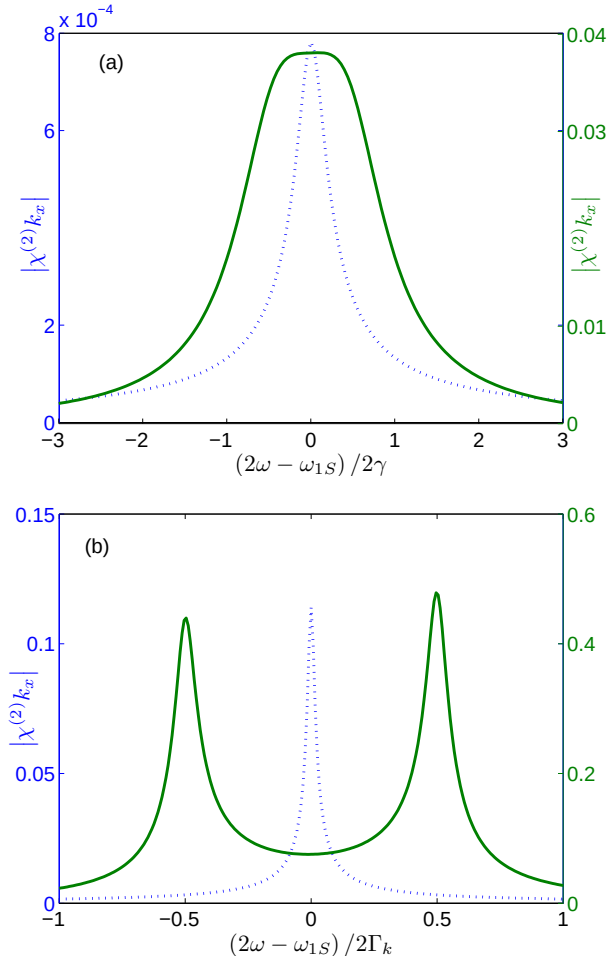

Figure 3.2: (Color on-line) Relative value of the nonlinear susceptibility in case of bulk cuprous oxide (dotted curves) and the quadrupole-dipole hybrid (solid curves). The Fig.3.2a represents moderate coupling $\Gamma_k = \hbar\gamma_{1S} = 0.29\ \mu eV$ and Fig.3.2b corresponds to strong coupling regime $\Gamma_k = 3.5\ \mu eV$. The density of the disordered DCM2 is taken $\rho_{DCM2} = 0.005\%$ while the CA density is $\rho_{CA} = 22\%$.

case SHG (See Fig.3.2 dotted curve). The maximum power generated by the second-harmonic is proportional to the square of the following expression:

$$\left|\chi^{(2)}_{ij,max}\left(2\hbar\omega=\hbar\omega_{1S}\right)k_x\right| = \frac{\mu_{2P}\mu_{1S,2P}}{\hbar\omega-\hbar\omega_{2P}}\frac{\mu_{1S,k}k_x}{\hbar\gamma_{1S}} \tag{3.12}$$

The small relative value of the SHG is due to the narrow QW of the cuprous oxide.

Second, the pump laser incidence angle is reduced to acquire the wave vector $k_0 a \ll ka$. The maximum power generated by the second-harmonic is proportional to the square of the following expression:

$$\left|\chi^{(2)}_{ij,max}\left(2\hbar\omega=\hbar\omega_{1S}\pm\Gamma_k\right)k_x\right| = \frac{\mu_{2P}\mu_{1S,2P}}{\hbar\omega-\hbar\omega_{2P}}\frac{\mu_F k_x}{\alpha_k\hbar\gamma} \tag{3.13}$$

Here the incidence angle dependent coefficient $\alpha_k = \sqrt{5}$ (See Fig.1.2a) for $ka = 0.13$ ($\Gamma_k = \hbar\gamma = 0.29\ \mu eV$) and $\alpha_k = 2$ for maximum value of the coupling $\Gamma_k = 3.5\ \mu eV$ at $ka = 1.57$ (See Fig.1.2b). Finally, comparing the last expression (3.13) to the bulk cuprous oxide (3.12) the second order response of the hybrid is amplified by the factor:

$$\left(\frac{\mu_F}{\mu_{1S}}\frac{\hbar\gamma_{1S}}{\alpha\hbar\gamma}\right)^2$$

Therefore the amplification can be adjusted by manipulating the organic composition (DCM2 and CA densities) or changing the pump laser incidence angle.

In conclusion for this chapter I would like to note that there is another merit in using the hybrid structure for the SHG. Namely the fact that the optical pumping can be replaced by an electrical pumping. For this the hybrid sample has to be placed between Alq3 and a-NPD [38] semiconductor plates. The bond structure and offset of these materials provide electrons and holes to form the hybrid exciton on the interface. Although, in this case one can expect the SHG only from the lower branch of the hybrid as the excions are accumulated in the minimum of the hybrid dispersion [24].

Part II

Polaritons

Chapter 4

Polaritons perturbed by LA-phonons

Cuprous oxide is considered as a probable candidate for BEC of excitons [41, 8, 42, 43]. The extremely small mass of the excitons allows them to condense at temperatures much higher than those of such atomic systems as helium or alkali metals [44]. The lowest excited states of cuprous oxide are classified following the cubic symmetry of the lattice (O_h). This gives the non degenerate ortho-exciton (Γ_5^+,[OE] , binding energy $E_b = 150\ meV$) and triple degenerate para-exciton (Γ_2^+,[PE] , binding energy $E_b = 162\ meV$). Due to even parity OE are quadrupole active, and PE remain optically inactive in one photon absorption experiments. However the PE can be effectively populated from the OE by emitting optical phonons or in two photon experiments. For the samples of high purity (more then 99.99 %) the line-width of OE is very narrow ($\hbar\gamma_{1S} \approx 0.8\ \mu eV$ for $T = 2K$) and detrmined mostly by

OE to PE conversion rate. This narrowness is responsible for the extremely long lifetime and profound (ns) BEC time coherence for the PE [32].

There are two main mechanisms impeding expected BEC in bulk cuprous oxide samples and both have non-statistical origin. First is *Auger heating* [45]. It was demonstrated that although OE run along an adiabat slightly above the condensation curve the PE get condensed. Second impeding mechanism is the relatively strong coupling to photons, so that such polaritons tend to *escape* the crystal before condensation occurs [42]. For such polaritons to experience BEC, there is a criterion of smallness imposed on the exciton-photon coupling. Only PE meet the criteria [8], but as far as I know there is still no conclusive evidence of BEC in the bulk cuprous oxide.

In this chapter I examine another possible mechanism obstructing BEC. Namely, a weak coupling of the polariton branches with long wavelength acoustical phonons and the effective formation of a new type of polariton. For low pumping intensity and in close proximity to the exciton-photon resonance one can consider the "weak" coupling to the LA-phonons [1] and treat the phonons semi-classically by means of some effective temperature dependence of the exciton energy. Namely, in the case of weak (but not negligible) electron-phonon coupling the semiconductor gap energy (and thus the energy

[1]The temperature is low enough to neglect contributions from the optical phonons

of the exciton) decreases. There is experimental evidence of the exciton energy red-shift for various semiconductors [46] as well as for cuprous oxide at helium temperatures [26].

In section 4.1 I compare this weakly perturbed polariton versus the concept of conventional phonoriton as an excitation formed by resonance interaction between the exciton, photon and phonon [47]. The resulting polariton branches strongly depend upon what kind of heating and cooling mechanism dominates.

In section 4.2 I investigate the pumping of a cuprous oxide thin film by short and ultrashort laser pulses (μs). In this regime the heating is a result of "phonon assisted" Auger process [45] and the cooling is provided by LA-phonons. The polaritons come to quasi-equilibrium and due to the temperature dependence of the exciton energy the dispersion is modified. Consequently I show localized states on the lower branch of this new polariton.

In section 4.3 I regard long laser pulses (ms). As a consequence, the temperature is defined by the laser heating and temperature exchange with the surrounding helium. I demonstrate that this results in temperature bistability and splitting of the dispersion curves into four distinct branches.

Numerical estimates of the decoherence effects are performed in the con-

cluding section 4.4 using realistic material parameters. According to my calculations this splitting and phonon induced decoherence may effectively obstruct BEC of the PE in cuprous oxide.

4.1 Perturbed polariton vs. conventional phonoriton

Let me consider a thin film of cuprous oxide ($d_s = 30\ \mu m$) placed in a helium bath at temperature $T_{bath} = 1.7\ K$ and pumped by laser pulses of varying power P_{ex}. The pumping laser field is polarized along $(1\bar{1}0)$ and has the wave vector $\mathbf{k}$ parallel to the (111) direction. The laser is tuned into resonance with dipole forbidden, quadrupole allowed $1S$ exciton ($\hbar\omega_{1S,0} = 2.05\ eV$ for OE and $\hbar\omega_{1S,0} = 2.05 - 0.097\ eV$ for PE). The exciton mass and radius are $M = 3m_0$, $a_B \approx 5.1\ \mathring{A}$. From the selection rules it follows that only the OE $(1/\sqrt{2})\left(\Gamma_{5x}^{+} - \Gamma_{5y}^{+}\right)$ are optically allowed with the oscillator strength of the transition $f_{[111]} = 3.7 \times 10^{-9}$. The PE acquire some oscillator strength $f_p = 4f_o 10^{-3}$ in a magnetic field or under an external stress through spin-orbit interaction.

The conventional phonoriton [48, 49, 47, 50] is a quasilinear mode depending parametrically on the intensity of the pump light (P_{ex}) and characterizes a coherent superposition of exciton, photon and phonon when up-conversion

[2] process is allowed. The laser pulse induces a pump polariton with the exciton wave vector $\mathbf{p}$ and energy $\hbar\omega_{\mathbf{p}}$. The excitonic component of the polariton couples with other excitonic modes $\mathbf{k}$, due to the exciton-LA-phonon interaction. To form the standard phonoriton, the laser intensity should be big enough to have the exciton-LA-phonon coupling:

$$Q_{\mathbf{k}-\mathbf{p}} = D_{ex}\sqrt{\frac{n_o\left|\mathbf{p}-\mathbf{k}\right|}{2\hbar\rho\upsilon_{ph}}} \sim \sqrt{\frac{P_{ex}}{\upsilon_g}} \tag{4.1}$$

comparable with the exciton-photon interaction $\Omega_{rabi} = \sqrt{f_o}E_{1S} \approx 124\ \mu eV$. Here I introduced D_{ex} as the exciton deformation potential; ρ is the mass density; υ_g , n_0 are the group velocity and density respectively of the polariton.

In terms of creation (annihilation) operators, the exciton ($b^{\dagger}_{\mathbf{k}}$) - photon ($c^{\dagger}_{\mathbf{k}-\mathbf{p}}$) - phonon ($\alpha^{\dagger}_{\mathbf{k}}$) Hamiltonian of the cuprous oxide crystal has form:

$$H/\hbar = \left(\omega_{1S,\mathbf{k}} - \omega_{\mathbf{p}}\right) b^{\dagger}_{\mathbf{k}} b_{\mathbf{k}} + \left(\omega^{photon}_{\mathbf{k}} - \omega_{\mathbf{p}}\right)\alpha^{\dagger}_{\mathbf{k}}\alpha_{\mathbf{k}} + \Omega^{phonon}_{\mathbf{p}-\mathbf{k}} c^{\dagger}_{\mathbf{k}-\mathbf{p}} c_{\mathbf{k}-\mathbf{p}} + \\ + \frac{i}{2}\Omega_{rabi,\mathbf{k}}\left(\alpha^{\dagger}_{\mathbf{k}} b_{\mathbf{k}} - b^{\dagger}_{\mathbf{k}}\alpha_{\mathbf{k}}\right) + Q_{\mathbf{k}-\mathbf{p}}\left(b^{\dagger}_{\mathbf{k}} c_{\mathbf{k}-\mathbf{p}} - c^{\dagger}_{\mathbf{k}-\mathbf{p}} b_{\mathbf{k}}\right)$$

Here $\omega^{photon}_{\mathbf{k}} = ck/\sqrt{\epsilon_\infty}$ and $\Omega^{phonon}_{\mathbf{p}-\mathbf{k}} = \upsilon_s\left|\mathbf{k}-\mathbf{p}\right| \approx 155\ \mu eV$ are the photon and phonon dispersion at the exciton-photon resonance $k_0 = 2.62\times10^5\ cm^{-1}$; $\epsilon_\infty = 6.5$ is the background dielectric constant; υ_s is the LA-sound velocity. The eigenvalues of the Hamiltonian above are given by an implicit phonoriton

[2] the phonon bath can serve as a source, not only as a drain for energy exchange processes

dispersion:

$$\begin{gathered}(\omega_{1S,\mathbf{k}}-\omega)\left(\omega_{\mathbf{k}}^{photon}-\omega\right)\left(\omega_{\mathbf{p}}+\Omega_{\mathbf{k}-\mathbf{p}}^{phonon}-\omega\right)- \\ Q_{\mathbf{k}-\mathbf{p}}^{2}\left(\omega_{\mathbf{k}}^{photon}-\omega\right)-\frac{\Omega_{rabi,\mathbf{k}}^{2}}{4}\left(\omega_{\mathbf{p}}+\Omega_{\mathbf{k}-\mathbf{p}}^{phonon}-\omega\right)=0\end{gathered} \tag{4.2}$$

In contrast to the standard picture of phonon-mediated polariton scattering, the dispersion is strongly modified from the polariton dispersion and consists of three dispersion branches. Around the exciton-photon resonance, such coherent polariton-phonon interaction results in an effective "blue" shift of the "polariton-like" branch of the phonoriton.

The key point in the phonoriton picture is the *coherence* between all the particle involved. However for small density of the polaritons the polariton-phonon interaction (4.1) is weak. Therefore, I define the "weak" polariton -phonon coupling as a limiting case of conventional phonoriton when the down-conversion [3] processes are dominant and up-conversion [4] processes are negligible. Therefore, in close proximity to exciton-photon resonance this "weak" interaction with the LA-phonons bath manifests itself by small *de-coherence* between exciton and photon in the polariton.

I propose to treat the LA-phonons semi-classically and use deviation of the polariton gas temperature from the temperature of the helium bath $T - T_{bath}$ as that small decoherence parameter. To estimate the influence of

[3] Polariton → phonon bath
[4] Phonon bath → polariton

the temperature deviation on the polariton dispersion, I adopt the following picture of the exciton-phonon interaction.

The electron and hole of the exciton part of the polariton move in the cloud of LA-phonons [5]. The result is a bigger mass of the exciton and red shift of the *energy gap* between the conduction and valence bands without noticeable effect on the binding energy of the $1S$ exciton [32]. There is experimental evidences for such exciton-phonon interaction. The exciton energy "red" shift has been observed for several types of semiconductor [46] as well as specifically for cuprous oxide at helium temperatures [26].

According to general formulation of the theory [27] this temperature dependence is accurately given by integrals of the form:

$$\omega_{1S,0}\left(T\right)-\omega_{1S,0}\left(T_{bath}\right)=-\frac{1}{2}\int d\omega f\left(\omega\right)\left(\coth\left(\frac{\hbar\omega}{2k_{B}\left(T-T_{bath}\right)}\right)-1\right) \tag{4.3}$$

Here $\coth\left(\frac{\hbar\omega}{2k_B(T-T_{bath})}\right)-1$ represents the average phonon occupancy number and $f(\omega)$ is the relevant electron-phonon spectral function.

Expanding the above equation (4.3) into series around the bath temperature, in linear approximation the dispersion of this perturbed polariton is

[5] I neglect TA phonons, as their contribution to the interaction is much weaker at the given temperature range [45]

given by the following system of equations:

$$\left(\omega_{1S,\mathbf{k}}\left(T\right)-\omega\right)\left(\omega_{\mathbf{k}}^{photon}-\omega\right)-\frac{\Omega_{rabi,\mathbf{k}}^{2}}{4}=0 \tag{4.4}$$

$$\hbar\omega_{1S,\mathbf{k}}\left(T\right)=\hbar\omega_{1S,0}\left(T_{bath}\right)+\frac{\varepsilon_{\infty}\hbar^{2}k^{2}}{2M}+\kappa\left(T-T_{bath}\right)$$

In the last expression the parameter $\kappa = 0.30\ \mu eV\ K^{-1}$ is experimentally determined [26]. The resulting polariton branches are given by the equations above along with a temperature equation which is strongly dependent upon what kind of heating and cooling mechanism prevails (See Fig.4.1). Therefore

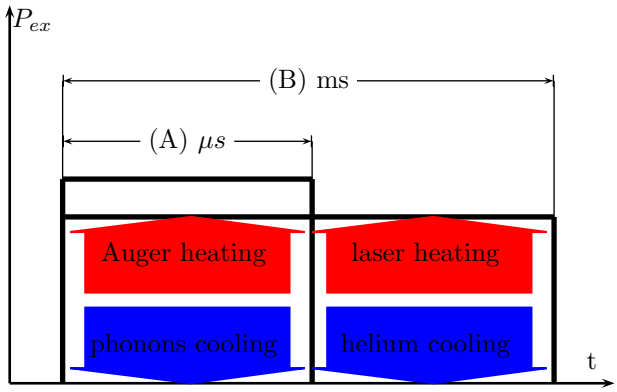

Figure 4.1: (Color on-line) Schematic of different heating (cooling) mechanism in the thin film of cuprous oxide. Different mechanisms create different thermal regime of the sample and result in different polariton dispersions. The case (A) corresponds to short excitation pulses, T is the temperature of the exciton gas, T_{bath} is the temperature of the LA phonons; and the case (B) corresponds to long pulses, T is the temperature of the LA phonons, T_{bath} is the temperature of the surrounding helium.

in the next sections I am going to consider two distinct cases:

(A) Short (μs) laser pulses, where heating is a result of "phonon-assisted"

Auger process [45] and the cooling is caused by LA-phonons. In picosecond dynamics the system comes to quasi-equilibrium, and due to the temperature dependence of the excitonic part of the polariton there is a distinct change in the dispersion.

(B) Long (ms) laser pulses are applied, which leads to the temperature being defined by photo-thermal laser heating and temperature exchange with the surrounding helium. This will result in a photo-thermal bistability effect.

Note that the "polariton-like" branches of the phonoriton given by equation (4.2) can be formally obtained from the system (4.4) by modeling the up-conversion processes with the additional condition $T_{bath} > T$. But the physical meaning of the system (4.4) is rather different. In my treatment the phonons are not mediators for the exciton-exciton interaction but the source of *decoherence* for the pump polariton.

4.2 Short laser pulses

First I consider short laser excitations (See Fig.4.1A). Therefore the system of interacting $1S$ quadrupole excitons, photons and low energy LA phonons can be treated *adiabatically*.

In the equation governing the dynamics of the temperature I neglect all ultra-fast processes [6], such as optical phonon cooling (characteristic time $\tau = 0.2 \times T^{-1/2}\ ns$); radiative decay ($\approx 300\ ns$); ortho-to-para down conversion ($\approx 0.014 \times T^{3/2}\ ns^{-1}$)[45].

The main sources of heating in this adiabatic system are the non radiative direct process and phonon assisted Auger process with the characteristic Auger decay time $\approx 0.1 \times T^{-3/2}\ \mu s$. Because the conduction and valence band share the same parity, the rate of direct Auger process is negligibly small. Hence, one has to consider "phonon-assisted" Auger process which is defined as exciton-exciton recombination into hot electron hole carriers accompanied by emission of a cascade of phonons (See [45] for more complete discussion).

The rate of change of the entropy of the excitons is a balance between the entropy loss due to phonon cooling and heating following Auger annihilation of the excitons. The rate of phonon cooling, which is dominated by emission of acoustic phonons, varies as $-a_1 T^{3/2}\,(T - T_{bath})$. On the other hand, heating of the excitons from the Auger process is proportional to the density of the polaritons $a_2 n_0$ [7]. The ratio of the coefficients a_1/a_2 varies from 4.75×10^{22} to 5.71×10^{22} and rapidly grows with increase in duration

[6] pico and nano second dynamical processes

[7] For the OE it comes close to the condensation line $n_0 \propto T^{3/2}$ at high density of the exciton gas but never crosses. For the PE there is BEC critical temperature given by the cross point.

of the pulses. This emphasizes the fact that for long pulses one can neglect the effect of the Auger heating comparing to the phonon cooling and has to consider direct heating by the laser field. Quantative comparison of the thermal red shift to other high density effects reported so far for the cuprous oxide crystals can be found in the Appendix II.

Consequently, with increasing temperature, the exciton density grows along the "quasi-equilibrium" adiabat:

$$-a_1 T^{3/2}\left(T - T_{bath}\right) + a_2 n = 0 \tag{4.5}$$

$$n\left(\omega, T\right) = \frac{4P_{ext}}{\pi d^2 \hbar\omega_{1S} v_g}$$

$$v_g^{-1} = \frac{\sqrt{\varepsilon_\infty}}{c}\frac{\partial x}{\partial \hbar\omega} \approx \frac{\sqrt{\varepsilon_\infty}}{c}\frac{x - \hbar\omega}{\hbar\omega_{1S,x}\left(T\right) - \hbar\omega}$$

Here $x = \hbar ck/\sqrt{\epsilon_\infty}$ is the energy of the pumping laser field.

The system of equations (4.5, 4.4) has only one solution for the temperature (no bi-stability). Therefore, it can be numerically resolved into the upper and lower branches of the perturbed polariton. To specify the branches for the phonoriton let me put the following conditions for the upper and lower branch correspondingly:

$$\lim_{x\to x_0^+, x\to x_0^-} \frac{\hbar}{x}\frac{\partial\omega}{\partial x} = 1 \tag{4.6}$$

In close proximity to the exciton-photon resonance ($x_0 = \hbar\omega_{1S}$) and for small light intensities, the solution of the nonlinear system (4.5,4.4) can be obtained

by perturbation theory. Therefore, in first order, I set an appropriate (4.6) unperturbed group velocity into the second equation of the system (4.5) and solve the corresponding algebraic system of equations (4.4) for new upper and lower branches of the polariton. The resulting polariton dispersion ($E = \hbar\omega$) as a deviation from the exciton energy ($E_{1S,x} = \hbar\omega_{1S,\mathbf{k}}$) is presented in Fig.4.2.

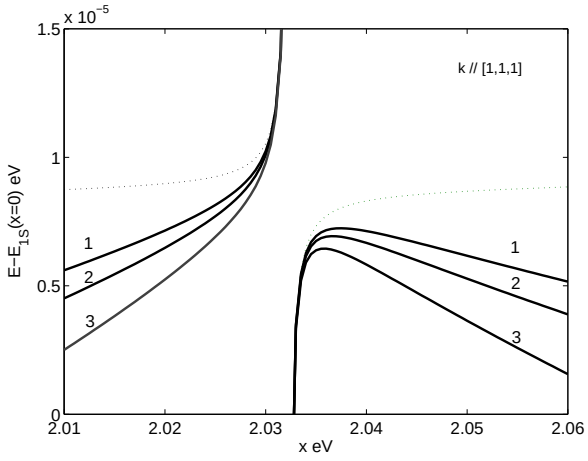

Figure 4.2: Polariton dispersion for short pump laser pulse and quasi-equilibrium of the exciton gas with the phonon bath. The "phonon-assisted" Auger process heats the exciton gas and weak interaction with LA-phonons cools it down. Solid lines represent two polariton branches for varying laser intensity: (1) $P_{ex} = 5\ mW$; (2) $P_{ex} = 10\ mW$; (3) $P_{ex} = 25\ mW$. The dash line corresponds to the unperturbed polariton: $P_{ex} < 5\ mW$.

For high laser intensities ($P_{ex} > 25\ mW$) the first approximation is not enough, and one must carry on with more iterations [8] which reduces the

[8] As an alternative to iterations one can approach the desirable intensity by changing it gradually.

"red" shift effect, as the group velocity grows.

The physics behind different levels of the perturbations can be described as the following. In zero approximation, a short laser pulse of energy close to the resonance x_0 enters the system and creates a polariton wave. The temperature of the system is equal to the $T_{bath} = 1.7\ K$ of the surrounding.

In first approximation, the polariton is relaxed due to polariton-exciton interaction. On the exciton-like part of the polariton (away from x_0) this leads to heating due to Auger process and as a consequence the "red" shift of the exciton energy. The perturbed polaritons accumulate on the lower branch according to the new group velocity. The polariton density build-up ($P_{ex} = 5\ mW$) is illustrated in Fig.4.3.

In the second approximation, this energy change increases the group velocity of the polariton waves and the exciton density is reduced and so is the temperature of the polariton gas. Therefore the polariton branches swing slightly back to the unperturbed polariton dispersion. Presumably, the quasi equilibrium between the Auger heating and LA-phonon cooling is established after some more steps.

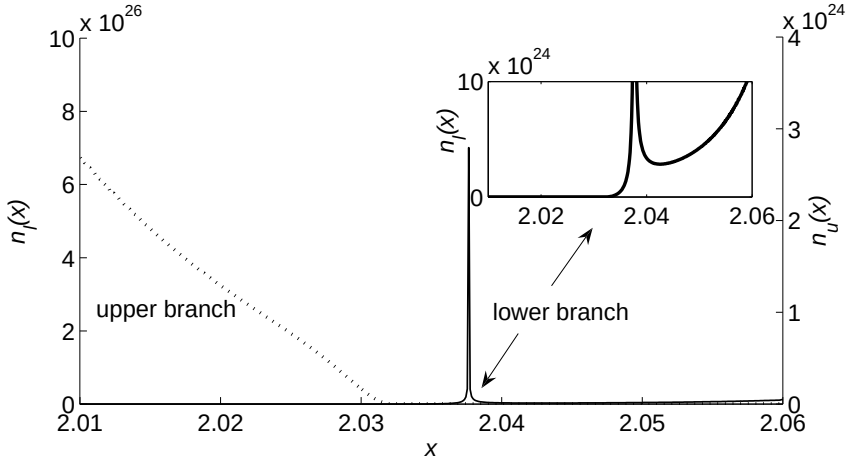

Figure 4.3: Density of polariton upper (n_u) and lower (n_l) branches in first approximation which must be used for the second approximation in the perturbation. The density peak represents the polaritonic build up on the lower branch as the result of high localization ($v_g \to 0$).

4.3 Long laser pulses

Now let us consider the case of long (ms) pumping signals. Contrary to the adiabatic case of short pulses, the heating is due to the laser radiation and cooling is due to surrounding helium (See Fig.4.1B) for the open system. As we are about to demonstrate, it results in bi-stability of the temperature and splitting of the dispersion curves into four different branches.

The bi-stability effect is due to the nonlinear origin of the temperature equation [26]. The heating process is proportional to the absorption inside the semiconductor film and therefore strongly dependent on the polariton

dispersion and proximity to the exciton-photon resonance. Neglecting the reflection, one can define the absorption through the temperature dependent transmission as: $1 - \mathrm{Tr}\,(\mathrm{T})$. Therefore, the equilibrium temperature is given by the stationary solution of the following time τ dependent system of equations:

$$\frac{dT}{d\tau} = HP_{ex}\left[1 - \mathrm{Tr}\left(\hbar\omega, T\right)\right] - C\left[T - T_{bath}\right] \tag{4.7}$$
$$\mathrm{Tr}\left(\hbar\omega, T\right) = \exp\left[-\frac{\Gamma_{1S}^2}{4\left(\hbar\omega_{1S}\left(x, T\right) - \hbar\omega\right)^2 + \Gamma_{1S}^2}\frac{d_s}{l_a}\right]$$

Here the phenomenologically introduced constants $H = 5.0 \times 10^6\ Ks^{-1}W^{-1}$ and $C = 2.8 \times 10^3\ s^{-1}$ giving the heating and cooling rate, respectively; $\Gamma_{1S} = 0.8\ \mu eV$ is the phenomenological line-width; the absorption length is given by:

$$l_a = \frac{\Gamma_{1S}\hbar c\sqrt{\varepsilon_\infty}}{f_o\hbar\omega_{1S,x_0}^2}$$

The factor 1/4 counts single-degenerate OE and triple-degenerate PE.

For a qualitative description of the bi-stability I fix the wave vector at energy $x = \hbar\omega = 2.01\ eV$ slightly off the resonant value x_0 and consider only the upper branch of the perturbed polariton. Then the heating part $HP_{ex}\left[1 - \mathrm{Tr}\left(\hbar\omega, T\right)\right]$ of the temperature equation (4.7) has a Gaussian shape, with the maximum dependent on detuning from the polariton energy. Depending on the value of the detuning it can cross the cooling

line $C\left[T - T_{bath}\right]$ on the phase diagram ($\partial T/\partial \tau$ vs. T) in one, two or three points on the the temperature scale. The last case corresponds to a strong nonlinearity and a hysteresis loop for the temperature in momentum-energy space.

If one moves from higher to lower energy (detuning $\hbar\omega(x) - E^{up} > 0$), temperature increases as the transmission decreases (See Fig.4.4). The shift of the excitonic part of the polariton and low transmission extend to large negative detuning and allows efficient heating. If one starts from negative values for the detuning, the sample is cold even beyond the "cut-off" (ζ) energy. Transmission remains close to unity and photo-thermal heating is inefficient. This means that the equilibrium state for the cold (up-going) scan and already heated (down-going) scan are different. Let us consider the down-going scan. When one closes up to the polariton upper branch energy the transmission decreases, which increases the sample temperature. At some point ("cut-off" energy) the heating becomes dominant over the cooling and we face a rapid temperature drop. The range of bi-stability mainly depends on laser pulses intensity P_{ex}.

For a quantative numerical calculation of the resulting dispersion curves, one has to resolve the nonlinear system of equations (4.4, 4.7) at equilibrium using standard perturbation theory. As a result of nonlinear origin of

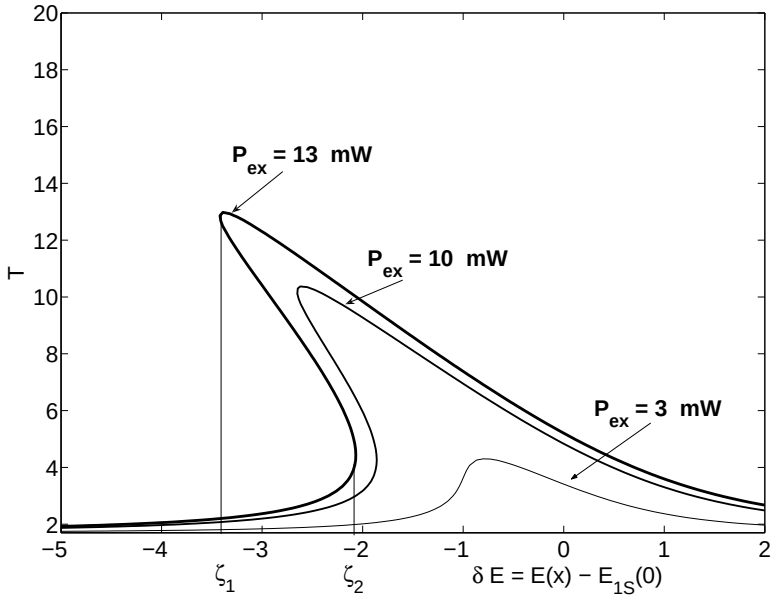

Figure 4.4: The first equation of the system (4.7) is visualized as an inexplicit function of the local sample temperature T and detuning δE from the resonance energy for different excitation intensities P_{ex}. The red shift of the maximum is accompanied by the bi-stability effect.

the temperature equation, there are four different polariton branches corresponding to the up- and down-scan (See Fig.4.5). The "bi-stability" effect manifests itself as abrupt drop in the temperature from red color for a large temperature to blue color for the cold helium.

4.4 Numerical results and discussion

The most important result which emerges from the dispersion curves in case of pumping by short pulses is the existence of a *localized state* on the lower branch of the polariton (Fig.4.4). So on a μs time interval one can observe replicas of these states in the luminescence spectra due to intense polariton build up in this state.

The evidence of such polariton density build-up modes can be demonstrated in the collapse and revival of the quantum beats of the scattered probe signal [**?**]. The luminescence from this highly unstable state can be considered as a signature of the polariton perturbation by the LA-phonons and can be utilized to produce delayed laser pulses. The states on the upper branch have bigger group velocity compared to standard polariton modes, and this can effectively prevent BEC as the polaritons escape the crystal more effectively.

In the case of long pump pulses an even more effective mechanism which

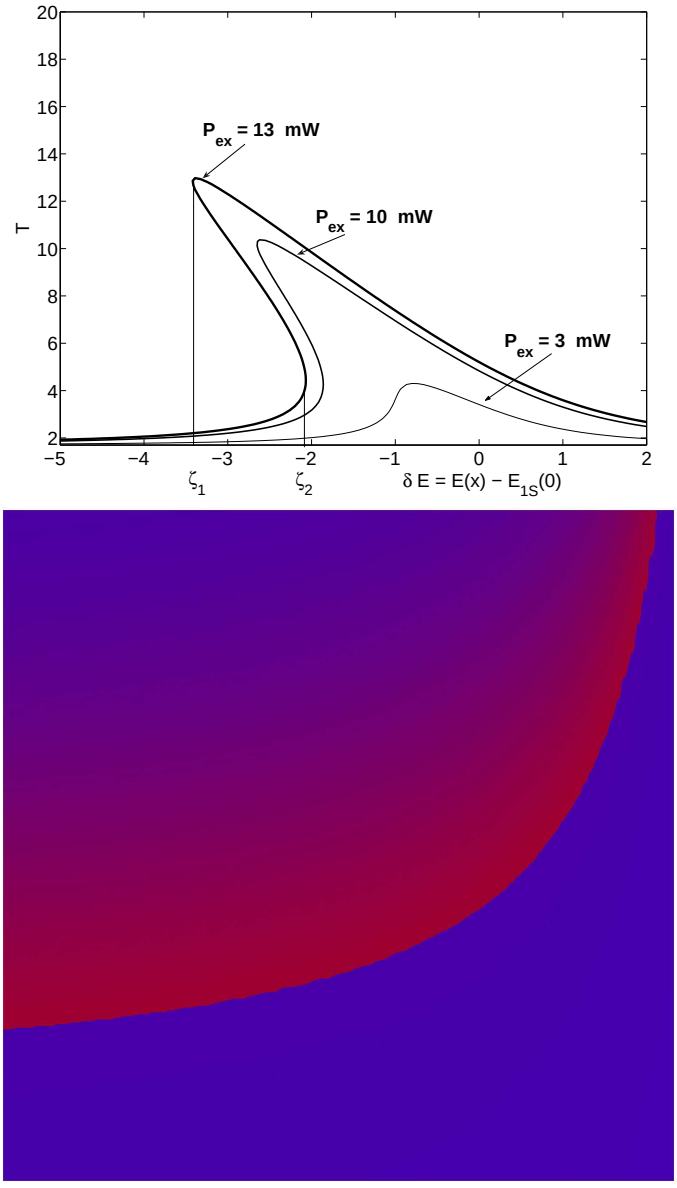

Figure 4.5: (Color on-line) The resulting branches (solid) of the quadrupole-LA phonoriton dispersion and corresponding temperature profile (upper branch only). The dashed lines correspond to noninteracting photon (vertical) and 1S quadrupole exciton (horizontal). The laser intensity is taken to be $P_{ex} = 5mW$. The bi-stability range for the exciton-like part of the phonoriton is approximately $2\mu eV$. Actual population of the branches depends on the initial condition and up or down-going scan. Also in case of big light intensity $P_{ex} > 57mW$ interconversion processes can occur due to optical Γ_{12}^{-} phonons

prevents BEC is provided by the bi-stability effect. Indeed it was demonstrated by Ell [42] that the BEC for excitation of states with sufficiently low oscillator strength is possible only when the kinetic energy of the excitonic part of the pump polariton is bigger than the splitting between the polariton branches at resonance. The latter prevents the polariton from "condensing" outside of the crystal. This condition certainly fails for the OE polaritons, since the kinetic energy is about 9 μeV and the Rabi splitting is 127 μeV. Moreover, the adiabat (4.4) never crosses the condensation line $T_c = n_0^{2/3} \times 10^{-11}$.

However, PE are good candidate for possible BEC and live long enough ($> 10\ ms$) to reach the equilibrium because the Rabi splitting is $\hbar\Omega_p = \hbar\Omega_o\sqrt{f_p/f_o} = 1.1\ \mu eV$ for 1 T magnetic field, which is eight times less then the kinetic energy. For rather large intensity of the pumping laser, according to the results of this paper, the polaritons are perturbed by the "weak" interaction with LA-phonons. Hence, due to the big life time of the para-exciton one has splitting of the upper and lower polariton branches into four new ones due to bi-stability effect. The extremely small oscillator strength for this para-exciton transition $f_p = 4f_o \times 10^{-3}$ supports the condensation condition stated above for the films starting from $d_s > 0.7\ mm$ thickness [51].

The upper and lower PE polariton branches are split into four new ones due to bi-stability effect in close analogy to the OE polariton. Let us estimate the effective splitting between all pairs of the polariton branches. According to the second equation of the system (4.4), to reach the critical condensation density of $n_c \approx (9T_{bath} \times 10^{11})^{3/2} = 1.89 \times 10^{18}\ cm^{-3}$ at the point of resonance with light, one needs intensity of the laser field $P_{ex} = 185\ mW$. In this case the calculated region of bi-stability is about $\zeta_1 - \zeta_2 = 25\ \mu eV$ which is approximately two times bigger than the kinetic energy of the PE. As a result BEC of the PE polaritons may be effectively *suppressed* by the bi-stability effect.

In conclusion for this chapter I would like to briefly outline possible deviations from the linear model of the temperature dependent exciton energy in cuprous oxide crystals which we used. If one has to consider the influence of the bi-stability effect on the possible BEC of the polariton or for high intensity of the pumping laser $P_{ex} > 35mW$ when the temperature growth is bigger than 87 K then the linear approximation for the temperature dependence of the gap energy given by (4.4) is may be not applicable.

Therefore, one has to apply more elaborate expression for the exciton energy $E_{1S}(T, x) \rightarrow E_{1S}(T, x, \rho)$ including a contribution from the optical phonons [27, 46]. The parameter ρ controls the relative contribution of the

long-wavelength acoustic phonons $\rho \rightarrow 1$, on one hand, and those of optical and short-wavelength acoustical phonons, on the other hand $\rho \rightarrow 0$. The dielectric background constant ϵ_∞ becomes a linear function of the wave vector.

Due to the complexity of the full expression it is useful to consider some approximations. When the acoustic phonons dominate, this expression transforms into the familiar Bose-Einstein model proposed by Vina [28]:

$$\hbar\omega_{1S}(T) = \hbar\omega_{1s}(0) - a\left[1 + \frac{2}{exp(\Theta/T) - 1}\right]$$

Here there are two fitting parameters a and Θ. Both emission and absorption of phonons are now considered. For the LA phonons the main contribution to the exciton energy can be fitted with the empirical relation proposed by Varshi [29]:

$$\hbar\omega_{1S}(T) = \hbar\omega_{1s}(0) - \frac{\alpha T^2}{T + \Theta}$$

Experiment [26] shows that for the bulk cuprous oxide $\alpha = 4.8{\times}10^{-7}\, eV/K$.

4.5 Appendix II

The comprehensive review article of Fernandez-Rossier [52] deals with exciton high density effects as the density approaches saturation. Here I apply their

theory to bulk cuprous oxide. The $1S$ exciton energy experiences "blue" shift due to exchange interaction between electrons and holes and red shift due to increased screening:

$$\Delta E^{blue} = \frac{13\pi}{3}\hbar\omega_{1S,0}na_B^3$$

$$\Delta E^{red} = f_o(\omega)\,\hbar\omega_{1S,0}\pi na_B^3$$

The screening spectral function is given by the following expression:

$$f(\varpi) = \frac{\varpi\left(32+63\varpi+44\varpi^2+11\varpi^3\right)}{(1+\varpi)^4} - \frac{8\varpi\,(4+3\varpi)}{(1+\varpi)^2}$$

and $\varpi^2 = (1+m_h/m_e)^2/(4m_h/m_e)$. These effects partially compensate each other.

To estimate the net shift let us take for example the following numerical vales: $P_{ext} = 5\ mW$ is the laser field intensity; $d = 1\times10^{-6}\ m$ is the diameter of the focused laser beam; $\upsilon_g = 4\times10^4\ m/s$ represents the group velocity of the pump polariton, and the factor 4 indicates the fact that we excite both OE and PE; $m_e = 0.69m_0$ and $m_h = 0.99m_0$ are the effective mass for electron and hole.

Due to small quadrupole exciton radius the net shift: $\Delta E^{red} - \Delta E^{blue} = -0.226\ \mu eV$. Hence, it is much less compared to the red shift due to the heating: $-2.1\ \mu eV$. But the situation will change drastically for a 2D quantum well, as in this case the blue shift is dominated due to exchange energy.

Note that these estimations are valid for any duration of the pulses required to build up the necessary polariton density.

The oscillator strength is proportional to the gap energy of cuprous oxide [19] and so depends on the temperature also . It gets smaller with increase of the pumping power. The relative change of the oscillator strength is $\approx 1.4 \times 10^{-3}$ for $T - T_{bath} = 20K$, but because it is not a resonant term we neglect this effect later on. For the same reason I neglect the temperature dependence of the line-width [26].

Chapter 5

Evanescent quadrupole polariton

Although quadrupole excitons in cuprous oxide crystals are good candidates for BEC due to their narrow line-width and long life-time there are some factors impeding BEC [45, 25]. One of these factors is that due to small but non negligible coupling to the photon bath, one must consider BEC of the corresponding mixed light-matter states called polaritons [8]. The photon-like part of the polariton has a large group velocity and tends to escape from the crystal. Thus, the temporal coherence of the condensate is effectively broken [53]. One proposed solution to this issue is to place the crystal into a planar micro-cavity [54]. But even state-of-the-art planar micro-cavities can hold the light no longer than 10 μs.

Therefore in this chapter we propose to impede the polariton escaping by trapping it into a whispering gallery mode (WGM) of a polystyrene micro-

sphere (PMS). In the next chapter I discuss hybridization between different WGM in a linear chain of dielectric spheres. Therefore, for more details on WGM see next chapter. Here I focus my attention on the WGM - quadrupole WE resonant coupling and following consequences of the proposed light-matter interaction.

5.1 Quadrupole-WGM coupling

I assume that the PMS of radius r_0 μm is placed at a small [1] distance $\delta r_0 \ll r_0$ from the cuprous oxide crystal ($\epsilon_{Cu2O} = 6.5$). Some density of quadrupole $1S$ excitons ([QE], $\hbar\omega_{1S} = 2.05$ eV, $\lambda_{1S} = 2\pi/\omega_{1S} = 6096$ $\mathring{A}$) has been created by an external laser pulse. The corresponding polaritons move in the crystal by diffusion and can be trapped at the surface by the micro-sphere.

Because the evanescent field penetration depth ($\lambda_{1S}/2\pi\,(\epsilon_{Cu2O} - 1)^{1/2} = 414$ $\mathring{A}$) is much bigger than the QE radius ($a_B = 4.6$ $\mathring{A}$) the light-matter interaction can be considered semi-classically. For resonance coupling with a WGM its size parameter should be determined by the resonant wave vector in the cuprous oxide $k_0 = 2.62 \times 10^7$ m^{-1}. For example, if one takes a polystyrene ($\epsilon^2 = 1.59$) sphere of radius $r_0 = 10.7$ μm then $k_0 r_0 = 28.78350$ and this corresponds to the 39TE1 resonance [55].

[1] comparing to the evanescent field penetration depth

The light part of the polariton trapped inside the PMS moves as it would move in a micro-cavity of the effective modal volume $V \ll 4\pi r_0^3/3$. Consequently, it can escape through the evanescent field. This evanescent field essentially has a quantum origin and is due to tunneling through the potential caused by dielectric mismatch on the PMS surface. Therefore, I define the *evanescent* polariton (EP) as an evanescent light-matter coherent superposition.

The evanescent light has small intensity. Therefore it is not effective for the dipole allowed coupling. But it has a large gradient, so it can effectively couple through its quadrupole part.

Let us assume that the incident polariton wave vector is along the interface and runs in the z direction, the polarization of the polariton is along the x direction. Therefore, in the system of coordinates centered at the sphere, the incident polariton light part can be written as [56]:

$$\mathbf{E}_i = E_0 i^l \frac{2l+1}{l\,(l+1)} \left(\mathbf{M}_{1l} - i\mathbf{N}_{1l}\right), \tag{5.1}$$

where $\mathbf{M}_{1l}$ and $\mathbf{N}_{1l}$ are vector spherical harmonics corresponding to TE- and TM-polarized modes of angular momentum l and z component of the angular momentum is $|m| = 1$; E_0 is the amplitude of the electric field. The scattered

field is given as:

$$\mathbf{E}_s = E_0 i^l \frac{2l+1}{l\,(l+1)} \left(i a_{1l} \mathbf{N}_{1l} - b_{1l} \mathbf{M}_{1l} \right), \tag{5.2}$$

where a_{1l} and b_{1l} are scattering Mie coefficients (See the Appendix III). Keeping only the resonant term the last expression yields:

$$\mathbf{E}_s = -E_0 i^l 0.05 b_{1,39} \mathbf{M}_{1,39}, \tag{5.3}$$

While in the system of the coordinate, centered at the cuprous oxide, the plane wave is still given by the expression (5.1), the scattered field has to be changed according to the vector spherical harmonic addition theorem [57]:

$$\mathbf{M}_{1,39} = A^{ml}_{1,39} \left(r_0 + \delta r \right) \mathbf{M}_{ml} + B^{ml}_{1,39} \left(r_0 + \delta r \right) \mathbf{N}_{ml} \tag{5.4}$$

Here $A^{ml}_{1,39}$ and $B^{ml}_{1,39}$ are the translational coefficients. Their explicit expression can be found, for instance, in [58, 55] and are explicitly listed in the Appendix III.

The bulk (incident) and evanescent polaritons in cuprous oxide are formed through the quadrupole part of the light-matter interaction:

$$H_{int} = \frac{ie}{m\omega_{1S}} \mathbf{E}_{i,s} \cdot \mathbf{p}$$

Here e, m are the electron mass and charge, and $\mathbf{p}$ is the electron momentum. For the quadrupole $1S$ transition in cuprous oxide the energy of the

interaction can be written as:

$$g = \left\langle {}^3\Gamma^+_{5,xz} \left| H_{int} \right| {}^1\Gamma^+_1 \right\rangle = \left\langle {}^3\Gamma^+_{5;1,2} \left| H_{int} \right| {}^1\Gamma^+_{1;0,0} \right\rangle \tag{5.5}$$

Here I introduced the initial state of the system, which transforms as irreducible representation ${}^1\Gamma^+_1$ of the cubic centered group O_h. The final state is the ortho-exciton state which transforms as ${}^3\Gamma^+_{5,xz}$ in Cartesian system or as ${}^3\Gamma^+_{5;1,2}$ in the corresponding spherical basis.

Hence, using (5.1, 5.3, 5.4, 5.5), one can deduce that the the coupling of the spherical harmonic compared to the plane wave ($g_{1,2} = 124\ \mu eV$) is resonantly enhanced:

$$\frac{g_{1,39}}{g_{1,2}} = -i0.06 b_{1,39} \left(kr_0\right) A^{1,2}_{1,39} \left(r_0 + \delta r\right) \tag{5.6}$$

Here I utilized the fact that $B^{1,2}_{1,39} \ll A^{1,2}_{1,39}$. While the resonant enhancement is provided by the $b_{1,39}$ Mie coefficient here, the translational coefficient reduces the effect. That is why if one tries to couple the evanescent light to the dipole transition the effect is much weaker as $A^{0,1}_{1,39} \ll A^{1,2}_{1,39}$. The resulting exciton - evanescent light coupling is shown in the Fig.5.1

The coupling grows with mode number l, because the gradient of the evanescent field increases. At $l = 89$ the coupling becomes of the order of meV. The property of the scalable coupling factor can be utilized in practical applications such as non-linear optics and is the subject of my future work.

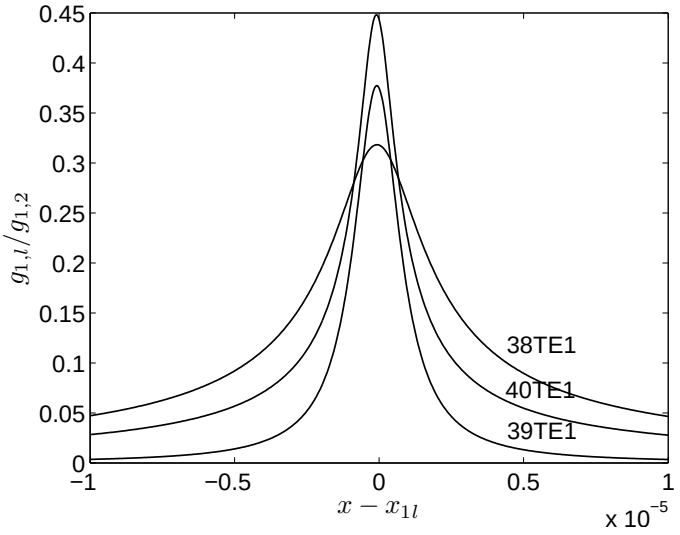

Figure 5.1: The evanescent light - $1S$ quadrupole coupling ($g_{1,l}$) scaled to the bulk exciton-photon coupling ($g_{1,2}$). The size parameter kr_0 is denoted as x and the PMS is placed directly on the cuprous oxide sample ($\delta r = 0$, See also Fig.5.2).

5.2 Numerical results and discussion

Around the resonance between WGM and the quadrupole exciton $\omega_{1l} \approx \omega_{1S}$ the EP branches are given by the eigenvalues of the following Hamiltonian:

$$H/\hbar = \omega_{1l} c_k^\dagger a_k + \omega_{1S} b_k^\dagger b_k + g_{1l} \left(c_k^\dagger b_k + c_k b_k^\dagger \right) \tag{5.7}$$

where $c_k,\ b_k$ are annihilation operators for light and the exciton, respectively. Therefore, considering that both the exciton and WGM of a single sphere are localized, the dispersion is reduced to:

$$\omega = \omega_{1S} \pm g_{1l}/\hbar \tag{5.8}$$

The excitons are trapped in the minimum of the lower branch. Hence the corresponding WGM pattern can be observed. The dispersion above is similar to the quadrupole-dipole hybrid in the organic-inorganic hetero-structures [25]. In the later case, the excited organic molecules create an evanescent field penetrating in the cuprous oxide.

The evanescent polariton provided by a single sphere gives the time coherence necessary for the observable BEC of the quadrupole exciton. But the spatial coherence is limited to a small region nearby to the sphere. To improve the spatial coherence one has to sacrifice the temporal coherence slightly by delocalizing the corresponding WGM. It can be done by using an

array of spheres aligned along the z direction and separated by the distance δr_0 (See Fig.5.2).

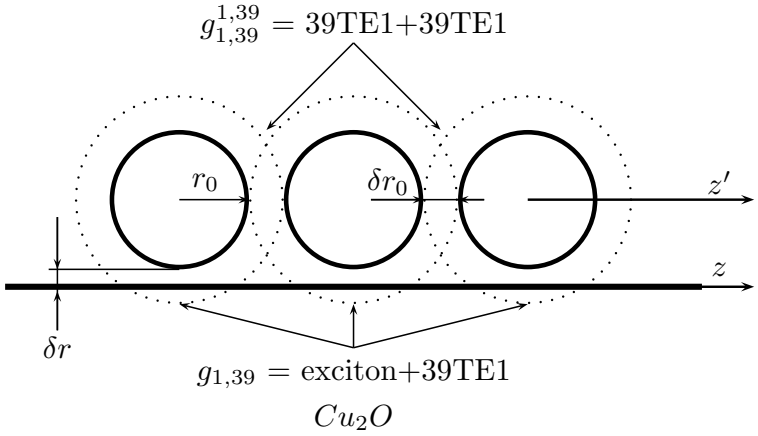

Figure 5.2: Schematic of formation of the evanescent polariton on linear chain of PMS. Actual dispersion is determined by the ratio of two coupling parameters such as exciton-WGM coupling and WGM-WGM coupling between the microspheres.

Recent experimental [5] and theoretical [59] studies have shown that the WGM can travel along the chain as "heavy photons". Therefore the WGM acquires the spatial dispersion, and the evanescent polariton has the form (See Fig.5.3):

$$2\omega = \omega_{1l,k} + \omega_{1S} \pm \sqrt{\left(\omega_{1l,k} - \omega_{1S}\right)^2 + 4|g_{1l}/\hbar|^2} \tag{5.9}$$

$$\omega_{1l,k} = \omega_{1S} + 2\left(g_{1l}^{1l}/\hbar\right) cos(x - x_{1l} + \pi/2) \tag{5.10}$$

Here $g_{1l}^{1l} = \omega_{1S} b_{1l} A_{1l}^{1l}(\delta r_1)$ is the nearest-neighbor inter-sphere coupling parameter.

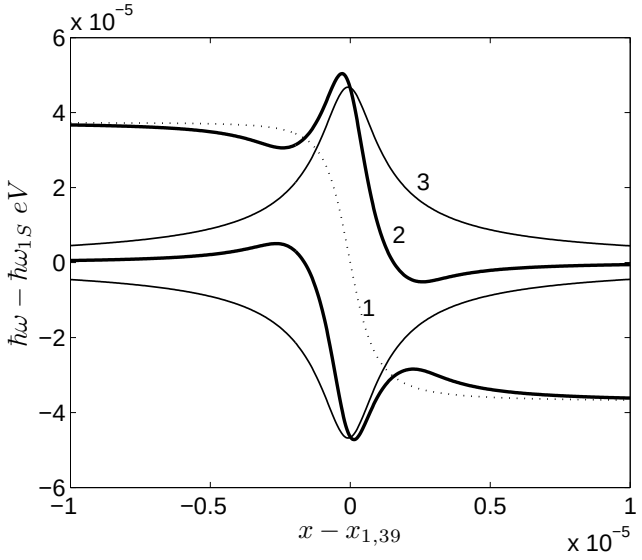

Figure 5.3: Dispersion of the evanescent polariton 39TE1. The dashed line (1) corresponds to the dispersion of the chain of spheres touching each other ($\delta r_0 = 0$). The thin solid line (3) stands for upper and lower branches of a single sphere dispersion ($\delta r_0 \gg \delta r = 0$). The thick solid curve (2) is the case of linear chain of the spheres in contact with the cuprous oxide ($\delta r_0 = \delta r = 0$).

When the coupling between spheres dominates ($\delta r \gg \delta r_0$) the minimum of the lower polariton branch disappears. Consequently, for BEC of the evanescent polariton one has to keep the desired balance between spatial and temporal coherence by adjusting experimental parameters δr and δr_0.

Both, the energy of the $1S$ quadrupole exciton and the WGM depend on the temperature. Therefore one can use a standard temperature scan to reveal the evanescent polariton dispersion [60].

In summary, I emphasize that because of high localization of the quadrupole exciton they couple "naturally" to the WGM. Although the coupling of the evanescent field to the dipole allowed excitation are less pronounced then quadrupole ($\mathbf{d} \cdot \mathbf{E}_i \ll Q_{ij} \nabla_i E_{s,j}$) it can be greatly improved by trapping the excitons in low dimensional structures such as quantum wells or quantum dots [61].

The theory developed above is applicable also for void cavities, spherical impurities and metallic droplets in bulk cuprous oxide crystal.

5.3 Appendix III

In the appendix I list explicit expression for the Mie scattering coefficient:

$$\begin{aligned} a_{ml} &= \frac{n^2 j_{ml}(nx)\left[x j_{ml}(x)\right]' - j_{ml}(x)\left[nx j_{ml}(nx)\right]'}{n^2 j_{ml}(nx)\left[x h^{(1)}_{ml}(x)\right]' - h^{(1)}_{ml}(x)\left[nx j_{ml}(nx)\right]'} \\ b_{ml} &= \frac{j_{ml}(nx)\left[x j_{ml}(x)\right]' - n^2 j_{ml}(x)\left[nx j_{ml}(nx)\right]'}{j_{ml}(nx)\left[x h^{(1)}_{ml}(x)\right]' - n^2 h^{(1)}_{ml}(x)\left[nx j_{ml}(nx)\right]'} \end{aligned}$$

Here $n = \epsilon^2$ is the refractive index of the spheres; $x = kr_0$ is the size parameter; $j_{ml},\ h_{ml}$ are the spherical Bessel and Hankel of the first kind functions respectively.

In the case of $l \gg 1$ the calculation of the translational coefficients can be significantly simplified with the help of the so-called maximum term approximation[55].

$$\begin{aligned} A^{l'}_{l} &\cong -2l(-1)^{l+1}\sqrt{\frac{l+l'}{\pi(l'+1)(l-1)}} \times \\ &\quad \frac{l^{l}(l')^{l'}}{(l'+1)^{l'+1}(l-1)^{l-1}} h^{(1)}_{l+l'}(\eta x) \\ B^{l'}_{l} &\cong i\frac{x|i-j|}{ll'} A^{l'}_{l} \end{aligned}$$

Here η defined as $\eta = |r_0 + \delta r|/r_0 \geq 1$ is a dimensionless distance between the centers of the spheres.

Chapter 6

Future work

In the future course of work I am going to proceed with investigating properties of the quadrupole hybrid excitons in cuprous oxide. Both types of the hybridization organic/inorganic and WGM/inorganic offer a great deal of space for further development. Below I just briefly highlight possible ways to go.

6.1 BEC of the QDH

The well pronounced minimum on the lower branch of the QDH suggest that search for BEC in this system may be fruitful. Therefore rigorous calculation of the life-time is necessary. The life-time of the QDH might be reduced due to increased diffusion rate in the organic [38]. Also I will have to calculate thermodynamical properties of the hybrid exciton, the critical temperature and density.

6.2 BEC of the evanescent polaritons

The WGM/inorganic hybrid is even more promising candidate for BEC search. It offers more flexible and controllable parameters of the system and at the same time also exhibits the key properties for BEC. It has long life-time and minimum on the lower dispersion branch. However in the linear chain of the PMS are not highly localized as it is the case of a single PMS. It makes possible to have large spacial coherence but may substantially decrease the life-time of the evanescent polariton. Therefore, as a next step I will try to form an evanescent polariton by coupling the quadrupole to the WGM bands of the anomalous dispersion described in the chapter 7. Such WGM bands have well pronounced minimum itself, therefore provide basis not only for substantial spacial coherence but for high localization and big lifetime of the polariton.

6.3 Collective effect of hybridization in multi-layered structure of perovskite-organic composite

Perovskite-organic composites are subject of great interest lately due to their applications as promising Optical Light Emitting Devices (OLED). There's an experimental evidence of hybrid exciton formation in this system [62]. I

propose to investigate collective properties of the hybrid excitons created in different layers. In simplest model, our estimation shows that the degeneracy of the two hybrid branches is lifted. A new hybrid band is formed. I propose to develop a complete quantum mechanical theory of the phenomena and propose concrete experiment.

6.4 Enhance light dragging effect

Following the concept of enhancing properties generic to the quadrupole WE in cuprous oxide by resonant hybridization with a suitable organic I anticipate noticeable enhancement in a singular light dragging effect [37]. This phenomena regards to "upsteram" bending of a light ray.

In conclusion I would like to notice that the resonant hybridization phenomena is applicable to many materials aside from cuprous oxide. It is new and exciting field to which I made a small contribution with my work.

Part III

Additional work

Chapter 7

WGM band mixing in PMS linear chains

Recent proposal of coupled resonator optical waveguides and optical filters [63, 64] stimulated interest in systems of optically coupled micro-spheres. It has been known for a long time that electromagnetic modes of an individual sphere (Mie resonances) with large enough values of their angular momentum can have very long radiative life-times [65].

The WHM are characterized by the concentration of the electromagnetic field along the surface of a sphere with an evanescent tail escaping outside. Such field configuration makes it possible to optically couple two spheres positioned in the proximity of one another. The same evanescent tail makes possible the WGM/exciton coupling also, as it was discussed in previous chapter. In this chapter I focus on WGM/WGM coupling and WG band /

band hybridization in a linear chain of mutually overlapping WGM [1]. Initial work on the optical coupling of the micro-spheres was concentrated on the case of just two spheres [2], where the splitting of the modes and the formation of the coupled states was observed [66, 67, 68]. Recently, however, an interest has shifted toward linear chain of many spheres, which are envisioned as building blocks of various photonic devices, such as waveguides [69] or delay lines [5].

The obvious result of optical coupling in this system is formation of collective optical excitations propagating along the chain, which I will call *supermodes* in order to distinguish them from the modes of individual spheres. The supermodes form photonic bands, which were observed by several research groups almost at the same time [70].

One of the popular tools used to analyze experimental results [5] is a simple phenomenological dispersion law of a tight-binding type (5.9). This approach, which was originally suggested in Ref. [63] to describe modes of coupled cavities, derive every photonic band from a respective single sphere WGM resonance, characterized by its angular momentum, l. Its applicability is based on the assumption that the modes of coupled spheres with different

[1] The work has been done in association with Prof. Lev Deych

[2] the arrangement is known as photonic atoms or molecules

l do not mix, which is certainly not true in the exact sense, but can be approximately valid or not valid at all depending upon the type of modes under consideration.

The admixture of WGM with different angular momentums arises already for two interacting spheres, and results from the violation of spherical symmetry in such systems. It has been realized early on that the inter-mode coupling is primary responsible for radiative decay of the coupled modes[58], and may also affect positions of the resonances in a bi-spherical structure. I will show in this paper that these effects are even more important, and in certain situations, crucial, for the supermodes of the multi-spherical chains. In these systems, instead of individual resonances, one has to consider mixing between bands of collective propagating excitations. Using analogy with solid state physics one can call this phenomenon band-mixing or band hybridization. In this chapter, I present a theory of the inter-band coupling in linear chain of spheres based on the tight-binding approach to the optical coupling. This approach was originally formulated in Ref.[71], and carefully analyzed for the case of bi-spheres in Ref.[55].

My main goal in this chapter is to extend the analysis of Ref.[55] to a linear chain of spheres, and apply it to the problem of photonic band structure

and dispersion laws of the quasi-stationary [3] collective optical excitations of the chain. Using a perturbative approach, I derive analytically dispersion equations characterizing these excitations and analyze them in several particular cases of recent experimental interest. I show, in particular, that in spite of a formal analogy between optical and electronic tight-binding models, the photonic band mixing may lead to very unusual effects, which do not have counterparts in solid state systems.

7.1 Tight-binding model

The system, which will be considered in the paper consists of a number of identical spheres with radius r_0 and refractive index n, whose centers are all aligned along the same line (see Fig.5.2) at a distance $\delta r_0 = 0$ from each other. In this chapter I assume that the coupling to the WE is negligible $\delta r \gg \delta r_0$. I will be interested in collective excitations of this chain, which in the spirit of tight-binding approach is described as a combination of WGM of individual spheres.

The collectivization of the WGM in a chain of spheres is the main focus of this chapter. As it was already was pointed out, the electric field of these modes has an evanescent character in the vicinity of the surface of

[3] long-living

their respective spheres making the tight-binding description of the optical coupling between adjacent spheres rather accurate. This description is based on generalizing the expansions for scattered wave given by Eq. (5.1) to the case of multiple spheres:

$$\mathbf{E_s} = \sum_{i,l,m} \left[\tilde{a}^i_{l,m} \mathbf{N}_{m,l}(\mathbf{r} - \mathbf{r}_i) + \tilde{b}^i_{l,m} \mathbf{M}_{m,l}(\mathbf{r} - \mathbf{r}_i) \right]. \tag{7.1}$$

Here $\mathbf{r}_i$ is the position vector of the center of i-th sphere. The problem is, however, that vector spherical harmonics (VSH) in this expansion are defined in different coordinate systems associated with the center of each sphere. In order to apply boundary conditions one need to rewrite them in a common coordinate system. This is achieved with the help of addition theorem [4], which presents VSH centered at point $\mathbf{r}_j$ in terms of VSH centered at a point $\mathbf{r}_i$:

$$\begin{aligned}
&\mathbf{N}_{l,m}(\mathbf{r} - \mathbf{r}_j) = \\
&= \sum_{l'=1}^{\infty} \sum_{m'=-l'}^{l'} \left[A^{l',m'}_{l,m}(\mathbf{r}_j - \mathbf{r}_i) \mathbf{N}_{l',m'}(\mathbf{r} - \mathbf{r}_i) + B^{l',m'}_{l,m}(\mathbf{r}_j - \mathbf{r}_i) \mathbf{M}_{l',m'}(\mathbf{r} - \mathbf{r}_i) \right] \\
&\mathbf{M}_{l,m}(\mathbf{r} - \mathbf{r}_j) = \\
&= \sum_{l'=1}^{\infty} \sum_{m'=-l'}^{l'} \left[A^{l',m'}_{l,m}(\mathbf{r}_j - \mathbf{r}_i) \mathbf{M}_{l',m'}(\mathbf{r} - \mathbf{r}_i) + B^{l',m'}_{l,m}(\mathbf{r}_j - \mathbf{r}_i) \mathbf{N}_{l',m'}(\mathbf{r} - \mathbf{r}_i) \right],
\end{aligned} \tag{7.2}$$

Using the addition theorem one can derive a system of equations for the

[4] See previous chapter for details

expansion coefficients $a^i_{l,m}$ and $b^i_{l,m}$ [58]:

$$\frac{\tilde{a}^i_{l,m}}{a_{l,m}} = \zeta_{l,m} + \sum_{j\neq i}\sum_{l',m'}\left[\tilde{a}^j_{l',m'}A^{l',m'}_{l,m}\left(\mathbf{r}_j - \mathbf{r}_i\right) + \tilde{b}^j_{l',m'}B^{l',m'}_{l,m}\left(\mathbf{r}_j - \mathbf{r}_i\right)\right] \quad (7.3)$$

$$\frac{\tilde{b}^i_{l,m}}{b_{l,m}} = \zeta_{l,m} + \sum_{j\neq i}\sum_{l',m'}\left[\tilde{b}^j_{l',m'}A^{l',m'}_{l,m}\left(\mathbf{r}_j - \mathbf{r}_i\right) + \tilde{a}^l_{l',m'}B^{l',m'}_{l,m}\left(\mathbf{r}_j - \mathbf{r}_i\right)\right] \quad (7.4)$$

Indexes i and j in these equations enumerate spheres, while l, l', m, m' correspond to different resonances of the individual spheres. The structure of these equations can be understood by noting that it is equivalent to Eq. (5.2), in which the incident field, characterized by coefficients $\zeta_{l,m=1} = \frac{2l+1}{l(l+1)}$ is replaced by its sum with the field scattered by all other spheres.

For a linear chain, in which all position vectors $\mathbf{r}_i$ can be chosen parallel to each other and to the z direction, these equations can be simplified. The translation coefficients can be shown to become $A^{l',m'}_{l,m} = A^{l'}_{l}\,\delta_{m,m'}$ and $B^{l',m'}_{l,m} = B^{l'}_{l}\,\delta_{m,m'}$. Thus, the sum over m' in Eq. (7.3) and (7.4) disappears, making the component of the angular momentum along the axis of the chain a conserving quantity.

This fact obviously reflects the axial symmetry of this system. In what follows, I shall assume that $m = 1$; results for other values of m can be obtained from my general formulas by recalculating parameters a and b as well as the translational coefficients. Thus, I can abridge my notations by dropping index m all together. At this point I also omit the term $\zeta_{l,m=1}$ describing

the external incident wave, which leaves us with a system of homogeneous linear equations and the problem of finding their normal modes instead of the problem of scattering of an external wave.

Thus, I present the equations for the scattering coefficients in the following form:

$$\frac{\tilde{a}_l^i}{a_l} = \sum_{j\neq i}\sum_{l'}\left[\tilde{a}_{l'}^j A_l^{l'}(i,j) + \tilde{b}_{l'}^l B_l^{l'}(i,j)\right] \tag{7.5}$$

$$\frac{\tilde{b}_l^i}{b_l} = \sum_{j\neq i}\sum_{l'}\left[\tilde{b}_{l'}^j A_l^{l'}(i,j) + \tilde{a}_{l'}^j B_l^{l'}(i,j)\right], \tag{7.6}$$

Here the position vectors, $\mathbf{r}_i$, of the spheres in the arguments of the translation coefficients are for shortness replaced with sphere's numbers, i.

Eq.(7.5) and (7.6) have been used by Miyazaki and Jimba in Ref.[55] for exact numerical analysis of a bi-sphere. They also developed for this system an approximate method of solution of these equations that reproduced results of the exact calculations with a good accuracy. Here I generalize this method for a system with an arbitrary, including infinite, number of spheres, where its use becomes crucial since exact numerical calculations grow increasingly more involved and expensive with the increase in the number of spheres in the chain. I will show here that using the expanded version of the tight-binding approximation I am able to derive analytically dispersion equations describing collective excitations of the chain, which can be solved numerically

with minimal computational efforts.

The reduction of Eq.(7.5) and Eq.(7.6) to an analytically tractable form is based on several important properties of the translation coefficients, $A_l^{l'}$, and $B_l^{l'}$. First of all, in the case of $l \gg 1$ the calculation of these coefficients can be significantly simplified with the help of the maximum term approximation [5]. This approximation is based upon the fact that the translation coefficients quickly decrease with the distance between the spheres. This property, which is a manifestation of the evanescent nature of the optical coupling between the spheres, allows one to keep in the sum over the spheres in Eq.(7.5) and (7.6) only terms with $j = i \pm 1$.

The resulting equations constitute the nearest neighbors approximation for the chain of the spheres. The sum over l' describes coupling between supermodes with different angular modes, which is the main subject of the present chapter. These equations also contain terms proportional to translation coefficients $B_l^{l'}$, which are responsible for coupling between supermodes with different polarizations. However, for the nearest neighbors $B_l^{l'} \ll A_l^{l'}$ for $l, l' \gg 1$.

We will see later that the main contribution to the sum over l' comes mostly from $l' \lesssim l$, and the cross-polarization coupling can, therefore, be ne-

[5] See Appendix III of the previous chapter

glected in most cases. In what follows I will also discard terms ζ_l responsible for external excitation. This leaves us with a system of homogeneous linear equations and the problem of finding their normal modes instead of the problem of scattering of an external wave. Thus, I present the final tight-binding equations describing TE and TM supermodes as:

$$\frac{\tilde{a}_l^i}{a_l} = \sum_{l'} A_l^{l'} \left(\tilde{a}_{l'}^{i-1} + \tilde{a}_{l'}^{i+1}\right) \tag{7.7}$$

$$\frac{\tilde{b}_l^i}{b_l} = \sum_{l'} A_l^{l'} \left(\tilde{b}_{l'}^{i-1} + \tilde{b}_{l'}^{i+1}\right), \tag{7.8}$$

Here the translation coefficients $A_l^{l'} = A_l^{l'}(i, i+1)$ play the role of the inter-site coupling parameters of the tight-binding approximation. They also play an important additional role of being coupling coefficients for supermodes with different l. These equations are very similar to electronic tight binding equations describing, for instance, s-p hybridization [72].

There is, however, a significant difference between optical and electronic problems caused by the non-Hermitian nature of matrix $A_l^{l'}$ describing the coupling in the optical case. We will see below that this peculiarity of optical tight-binding equations is responsible for the anomalous dispersion properties of the system under consideration. The non-Hermitian nature of the optical band coupling appears also in a multiple scattering (optical Korringa-Kohn-Rostocker) approach to this problem developed in Ref.[73].

7.2 Collective excitations of a single mode

7.2.1 Single band approximation

Neglecting terms with $l' \neq l$ in equations (7.7) and (7.8) one obtains a simple single-band nearest-neighbor interaction model describing bands of the collective supermodes originating from $lTEs$ or $lTMs$ WGM's of an individual sphere with the size parameter x_{ls}. For a TE band, for instance, one has:

$$\frac{\tilde{a}_l^i}{a_l} = A_l^l \left(\tilde{a}_l^{i-1} + \tilde{a}_l^{i+1}\right) \tag{7.9}$$

and the equation for TM bands has the same form with an obvious substitution of b_l instead of a_l. In order to isolate a single band, and convert this equation into a standard tight-binding form, I can take advantage of the fact that the expected width of the band of the l, s supermode, δx_{ls}, is rather small, $\delta x_{ls} \ll x_{ls}$. In this case one can expand the single sphere scattering parameters a_l or b_l around their respective resonance frequencies $x_{ls,TE}$ or $x_{ls,TM}$. Taking into account the resonant nature of the scattering parameters, one can write down:

$$\frac{1}{a_l} \approx \frac{(x - x_{ls} + i\gamma_{ls})}{i\Delta_{ls}}, \tag{7.10}$$

and the similar equation for the TM polarization. Parameters Δ_{ls} in Eq.(7.10) are real valued positive quantities for all l and s[55], and γ_{ls} represents the

rate of the radiative decay of the respective WGM. Taking into account that translation parameters $A_l^{l'}$ in the maximum term approximation are almost purely imaginary quantities:

$$A_l^{l'} \cong i\,(-1)^{l+1}\left|A_l^{l'}\right| \tag{7.11}$$

Calculating them at the resonance size parameter (frequency) x_{ls}, one can re-write Eq.(7.9) or similar equation for the TM polarization in the standard for the tight-binding approximation form:

$$(x - x_{ls} + i\gamma_{ls})\,\tilde{a}_l^i = (-1)^l\,\Delta_{ls}\tilde{A}_{ls}\left(\tilde{a}_l^{i-1} + \tilde{a}_l^{i+1}\right), \tag{7.12}$$

where $\tilde{A}_{ls} = \left|A_l^l\,(x_{ls})\right|$. Normal modes of this system of equations are harmonic waves:

$$\tilde{a}_l^i \propto \exp(iq_{ls}z_i) \tag{7.13}$$

Here z_i is the z coordinate of the i-th sphere, and $q_{ls}(x)$ is a Bloch wave number. It satisfies the dispersion equation of the same type as Eq.(5.9), where I can now give a microscopic expression for the phenomenological coupling parameter κ:

$$\kappa_{ls} = (-1)^l 2\Delta_{ls}\tilde{A}_{ls} \tag{7.14}$$

Dispersion equation (Eq.(5.9)) describes a band of excitations, which is symmetric with respect to the WPG frequency x_{ls}, and whose boundaries

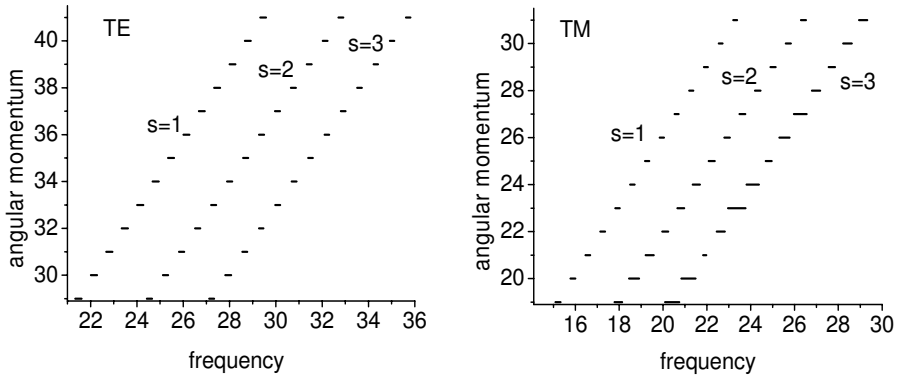

Figure 7.1: Positions and widths of several TE and TM supermodes obtained in a single band approximation.

$x_b^{\pm}$ are given by expression:

$$x_b^{\pm} = x_{ls} \pm \kappa_{ls} \tag{7.15}$$

In the case of a chain consisting of a finite number of spheres, N, the dispersion equation (5.9) can be used to find the spectrum of the respective frequencies. To this end, one has to impose obvious boundary conditions for the coefficients $\tilde{a}_l^i$, which read as $\tilde{a}_l^0 = \tilde{a}_l^{N+1} = 0$, where I assume that first sphere in the chain is assigned number $i = 1$. These boundary conditions determine the allowed values of the Bloch wave number q_{ls}: $q_{ls}\eta = \pi n/(N+1)$, where n changes from 1 to N. Applying this result to the case of only two spheres I find that there are two possible values of q_{ls}, namely $q_{ls}\eta = \pi/3$ and $q_{ls}\eta = 2\pi/3$. The respective values of frequencies $x_{ls}^{1,2} = x_{ls} \pm \kappa_{ls}/2$, repro-

duce the results of Ref.[55] obtained for the case of a bi-sphere in the single mode approximation. The radiative decay characterized by γ_{ls} makes the supermodes quasi-stationary; obviously the whole concept of the collective excitations with different q can only make sense if $\gamma_{ls} \ll \kappa_{ls}$. Calculations as well as experiments [69, 5] show that for modes with large l this inequality is well satisfied.

This simple picture could describe supermodes that do not overlap spectrally since only in this case omitting terms with $l' \neq l$ in Eq.(7.7) can be justified. The bands of collective excitations in the chain of microspheres, however, almost certainly overlap with at least one or more other bands. In Fig.7.1 I presented positions and widths of a number of supermode bands calculated in the single band approximation. It should be understood, however, that because of the inherently present radiative decay, the concept of allowed and forbidden bands is not very well defined even for modes with relatively large Q-factors. Nevertheless, I will use these terms to describe spectral regions, where the wave number q would have been purely real or purely imaginary in the absence of the decay, respectively. In reality, the wave number is a complex valued quantity at all real frequencies, and a difference between allowed and forbidden bands manifests itself only in relative magnitudes of real and imaginary parts of q: $\mathrm{Im}\, q \ll \mathrm{Re}\, q$ within the allowed

band, and $\mathrm{Im}\, q \gg \mathrm{Re}\, q$ within the forbidden bands. In the vicinity of the band boundaries, $x_b^{\pm}$, the real and imaginary parts are of the same order: $\mathrm{Im}\, q \simeq \mathrm{Re}\, q$.

7.3 Inter-band coupling

In this subsection I will take into account non-diagonal terms in Eq.(7.7) and (7.8), which are responsible for coupling between bands with different angular momentum described in the previous subsection. Since calculations for TE and TM modes are almost identical, I shall consider explicitly only TE polarization; results for TM polarization, which I will use for numerical examples, can be easily obtained with the help of obvious substitution of the parameters. A particular solution to the system of equations (7.7) can be easily found in the form of a harmonic wave: $a_l^{(i)} = a_l e^{iqz_i}$, where a_l satisfy the following algebraic equations:

$$\frac{1}{a_l}\tilde{a}_l + 2\cos(q\eta)\sum_{l'} A_l^{l'}\tilde{a}_{l'} = 0 \tag{7.16}$$

Let us consider this equation in a frequency region occupied by a single-band supermode $l_0 TE s_0$ characterized by quantum numbers $l = l_0$ and $s = s_0$. I am interested in finding corrections to the single band dispersion law for this supermode caused by its interaction with other bands. In order to develop an

approximate analytical solution for this problem one has to take into account several circumstances. First, main corrections to the diagonal approximation come from those l, which correspond to bands spectrally overlapping with l_0TEs_0.

It should be remembered, however, that the bands discussed in the previous subsection are broadened because of the radiative decay, and the term overlap should be understood with this fact in mind. One can see from Fig.7.1 that all supermodes with $l > l_0$ are spectrally well separated from l_0TEs_0, thus the respective terms in Eq.(7.7) can be considered a small perturbation despite the fact that $A^l_{l_0} > A^l_l$ for $l > l_0$.

Terms with $l < l_0$ are more important since according to Fig.7.1 respective bands can be spectrally in close proximity to l_0TEs_0, or even overlap with it. On the other hand coupling coefficients $A^l_{l_0}$ quickly decrease when l becomes smaller than l_0. Thus, the effect of coupling to these supermodes depends on an interplay between resonant enhancement due to spectral proximity, and decrease in the coupling parameter $A^l_{l_0}$.

In most practical situation, among all the bands contributing to the sum over l' there is just one, which I will label as l_1TEs_1, effecting the supermode under consideration in a most significant way. Usually the interaction with such a band is too strong to allow for a perturbative treatment. Following

the terminology of Ref.[55] I will call l_0TEs_0 and l_1TEs_1 significant supermodes, while the remaining ones are called bath or reservoir bands and can be treated perturbationally. I will show here that in the system under consideration the inter-band coupling can result in three qualitatively different types of the modifications of the dispersion laws. One, which is characteristic for weaker interaction can be called band renormalization, while the others, requiring a stronger coupling, are more appropriately called *band hybridization*. There might be two types of the hybridization, one arising, when the interacting bands are characterized by angular momentum indexes of the same parity, and the other one corresponding to the situation, when they have angular momentum indexes of different parities. I will show that the hybrid band arising in each of these cases exhibit qualitatively different dispersion properties.

I will begin by developing a general theory capable of describing all possible situations, and then consider conditions controlling a transition from one regime to the other. As it was mentioned before, the interaction between l_0TEs_0 and l_1TEs_1 should be taken into account exactly, while the contribution from all other supermodes can be treated perturbatively.

Accordingly, I present the system of Eq.(7.16) for the amplitudes of the

supermodes in the following form:

$$\begin{aligned}
&\left[\frac{1}{a_{l_0}}+2A_{l_0}^{l_0}\cos\left(q\eta\right)\right]\tilde{a}_{l_0}+2\cos\left(q\eta\right)A_{l_0}^{l_1}\tilde{a}_{l_1}+2\cos\left(q\eta\right)\sum_{l\neq l_0,l_1}A_{l_0}^{l}\tilde{a}_{l}=0\\
&\left[\frac{1}{a_{l_1}}+2A_{l_1}^{l_1}\cos\left(q\eta\right)\right]\tilde{a}_{l_1}+2\cos\left(q\eta\right)A_{l_1}^{l^0}\tilde{a}_{l^0}+2\cos\left(q\eta\right)\sum_{l\neq l_0,l_1}A_{l_1}^{l}\tilde{a}_{l}=0\\
&\left[\frac{1}{a_{l}}+2A_{l}^{l}\cos\left(q\eta\right)\right]\tilde{a}_{l}+2\cos\left(q\eta\right)\sum_{l'\neq l}A_{l}^{l'}\tilde{a}_{l'}=0.
\end{aligned}\tag{7.17}$$

Here in the first two lines I extracted from the sum over l the terms with $l=l_0$ and $l=l_1$, and wrote down the separate equations for the respective amplitudes. The last line in Eq. (7.17) represents the equation for the reservoir modes, which I solve for a_l and substitute the solution to the first two lines of this equation. In the resulting double sum over l and l', I keep only terms with $l'=l_0$ and $l'=l_1$. This procedure, which constitutes the second order perturbation theory for the reservoir bands, results in a system of equations for the amplitudes of the significant supermodes, which can be presented in the following form:

$$\begin{aligned}
&\left[\frac{1}{a_{l_0}}+2\tilde{A}_{l_0}^{l_0}\cos\left(q\eta\right)\right]\tilde{a}_{l_0}+2\cos\left(q\eta\right)\tilde{A}_{l_0}^{l_1}\tilde{a}_{l_1}=0\\
&\left[\frac{1}{a_{l_1}}+2\tilde{A}_{l_1}^{l_1}\cos\left(q\eta\right)\right]\tilde{a}_{l_1}+2\cos\left(q\eta\right)\tilde{A}_{l_1}^{l^0}\tilde{a}_{l^0}=0
\end{aligned}\tag{7.18}$$

The weak interaction with the reservoir results here in the renormalization of the coupling coefficients according to the rule:

$$A_l^{l'}\rightarrow\tilde{A}_l^{l'}=A_l^{l'}\left[1+\cos\left(q\eta\right)\sum_{\nu\neq l,l'}\frac{\Omega_{l\nu}^{l'}}{\cos\left(q\eta\right)-\cos\left(q_\nu\eta\right)}\right],\tag{7.19}$$

where

$$\Omega_{l\nu}^{l'} = \frac{A_l^\nu A_\nu^{l'}}{A_l^{l'} A_\nu^\nu} \tag{7.20}$$

is the inter-band interaction constant, and $\cos(q_\nu \eta)$ corresponds to the single band approximation for the reservoir modes defined as

$$\cos(q_\nu \eta) = -\frac{1}{2\alpha_\nu A_\nu^\nu}. \tag{7.21}$$

In contrast to Sec.7.2.1 I have omitted here subindex s in my notations for wave numbers q_ν. The reason for this is that there is no summation over s in any of the equations describing the inter-supermode coupling, such as Eq. (7.16) or (7.17), and the dependence on this index appears in an explicit form only if one expands scattering coefficients α_l around a respective WGM. Unlike in Sec.7.2.1 I cannot do this here, because I take into account contributions from bands in the frequency region, which can be relatively far away from their respective parent WGMs. Thus, the sum over ν in Eq. (7.19) contains contributions from terms for which the vicinities of $x_{l_0 s_0}$ and $x_{l_1 s_1}$ belong to the forbidden bands of respective supermodes, so that their (mostly imaginary) parameters q_ν, defined by Eq. (7.21), can no longer be associated with a particular WGM.

Eq.(7.18) describes new bands formed from the initial $l_0 TE s_0$ and $l_1 TE s_1$ bands. In order to simplify notations I will omit for now the angular mo-

mentum indices, and will label these new bands simply as q_+ and q_-. I can present dispersion equations for each of $q_\pm$ in the form:

$$\cos(q_\pm\eta) = \frac{1}{2}\left(\frac{1}{1-\tilde{\Omega}_{l_0l_1}}\right)\times$$
$$\left[\cos(\tilde{q}_{l_0}\eta)+\cos(\tilde{q}_{l_1}\eta) \pm \sqrt{\left[\cos(\tilde{q}_{l_0}\eta)-\cos(\tilde{q}_{l_1}\eta)\right]^2 + 4\tilde{\Omega}_{l_0l_1}\cos(\tilde{q}_{l_0}\eta)\cos(\tilde{q}_{l_1}\eta)}\right], \tag{7.22}$$

Here $\tilde{\Omega}_{l_0l_1}$ is defined by Eq.(7.20), in which I set $l' = l = l_0$, $\nu = l_1$, drop the upper index as duplicate, and replace the coupling coefficients with their renormalized according to Eq.(7.19) values. Similarly, $\tilde{q}_l$ are defined as in Eq.(7.21), but also with renormalized coupling coefficients.

Eq.(7.22) can be considered either as equations for wave numbers $q_\pm$ as functions of frequency x, or as equations for two frequencies $x_\pm$ as functions of wave number q. The choice depends on an experimental situation under consideration. In the transport experiments of the type carried out in Ref. [69] the frequency is fixed by an external excitation, and q is determined from the experiment. In this case I have to solve this equation for $q_\pm$ treating x as an independent real valued variable. The resulting wave numbers are complex, and their imaginary parts characterize the spatial decay of the wave along the chain. On the other hand, in the resonance experiments of Ref. [5] the wave number is fixed, and frequency is measured. In this case, I have to solve my dispersion equation for x considering q as a real quantity. The

frequencies obtained as a result contain imaginary parts, which describe the spectral width of the respective resonances. It is important to understand that because the dispersion equation is complex, the functions $Re(q_{\pm}(x))$ and $Re(x_{\pm}(q))$ obtained in these two approaches are not inverse of each other.

In this chapter I will focus on finding $q_{\pm}(x)$ because it presents greater interest from the stand point of experiment as well as applications. For two special values of frequency, Eq.(7.22) can be solved exactly. Indeed, consider $x = x_{l_0 s_0}$, where $\cos(\tilde{q}_{l_0})$ is exactly equal to zero regardless of the renormalization of the coupling coefficients. In this case the term responsible for the inter-band coupling vanishes, and I obtain that one of the $\cos q_{\pm}$ is also equal to zero. The same is obviously valid for $x = x_{l_1 s_1}$. I can conclude, thus that the centers of all bands, where $q_{\pm}\eta = \pi/2$, correspond to frequencies of the respective parent WGM resonances regardless of the presence of the inter-band coupling. In resonant experiments with finite chains [5] the admissible values of q are determined by the boundary conditions at the ends of the chain. In this situation, the center of the band is accessible only in systems with odd number of spheres. Therefore, spectra of chains with odd and even number of spheres can be distinguished from each other by, respectively, presence or absence of excitations at frequencies corresponding to single sphere whispering gallery modes. This conclusion is in complete agreement with

observations of Ref.[5].

In general case I can solve Eq.(7.22) numerically by consecutive iterations. The zero iteration corresponds to neglecting the bath-induced renormalization of the coupling coefficients, and produces two zero-order dispersion curves $q_{\pm}^{(0)}$. At the next step, $q_{\pm}^{(0)}$ are substituted to Eq. (7.19) and Eq. (7.21) producing a pair (one for $q_{+}^{(0)}$ and one for $q_{-}^{(0)}$) of new values of the coupling coefficients and "single-band" wave numbers $\tilde{q}_l$. These new values go back to Eq.(7.22), one to the "+" version of it, and the other to the "−" version. The procedure can be repeated as many times as necessary to achieve its convergence. The experience shows, however, that a good approximation for $q_{\pm}$ can already be obtained after only the first iteration.

While the contributions from the reservoir bands can be important, the main qualitative characteristics of the dispersion laws of the significant supermodes can be understood from the zero order approximation, which is presented by Eq.(7.22) without the renormalization of the coupling coefficients. Let us focus on the frequency region, where expression $\cos q_{l_0} - \cos q_{l_1}$ is small because this is where the main effects of the inter-band interaction are expected. The strongest effects occur in the vicinity of a resonance between

supermodes l_0 and l_1, when:

$$\mathrm{Re}\left[\cos\left(q_{l_0}\eta\right)\right] = \mathrm{Re}\left[\cos\left(q_{l_1}\eta\right)\right], \tag{7.23}$$

if it takes place in the frequency range covering initial l_0TEs_0 and l_1TEs_1 bands. It should be noted, however, that because of the radiative decay the band boundaries particularly for the band with larger s are not that very well defined, and the strong effects can take place even if the resonance condition is fulfilled in the forbidden band of one or even both of the modes, if the resonance point lies in proximity of a band boundary. It is important to remember also that Eq.(7.23) is not equivalent to $\mathrm{Re}(q_{l_0}) = \mathrm{Re}(q_{l_1})$, which is often accepted as a resonance condition.

The properties of the dispersion curves in the vicinity of the resonance point are determined by two circumstances: (i) the parity of single band dispersion laws, and (ii) the relation between $[\mathrm{Im}\left[\cos\left(q_{l_1}\eta\right)\right] - \mathrm{Im}\left[\cos\left(q_{l_0}\eta\right)\right]]^2$ and $\Omega_{l_0l_1}\cos(q_{l_0}\eta)\cos(q_{l_1}\eta)$, which determines if the band interaction is weak or strong. In most cases the overlapping supermodes originate from WGM with different s, and, therefore, usually, one of the imaginary parts in the expression above is significantly (orders of magnitude) larger than the other one. In this case the stronger decaying supermode determines the nature of the modification of the dispersion laws. It is quite obvious that the strong

coupling case (band hybridization) would correspond to the interaction terms prevailing over the dissipative terms, and the weak coupling regime (band modification) would take place in the opposite situation. If the resonance condition is not fulfilled in the spectral region of interest the modification of the dispersion law always belongs to the weak coupling case. What is surprising, however, is that even in this case the modification can be so strong as to render the perturbative treatment of interaction between the significant modes not very accurate.

An important peculiarity of the dispersion curves described by Eq.(7.22) distinguishing it from other cases of mode coupling [6] is the sign of the inter-band interaction parameter, $\Omega_{l_0 l_1}$. Using properties of the coupling coefficients $A_l^{l'}$ it can be shown that this parameter is always positive regardless of the parities of the angular momentum indexes l and l'. The parity of l according to Eq.(7.12) determines the sign of the slope of the respective dispersion laws in the vicinity of band boundaries. Taking into account that in the frequency region of interest $\cos(q_{l_0}\eta)$ and $\cos(q_{l_1}\eta)$ are, at least, of the same sign, I conclude that the entire interaction term $\Omega_{l_0 l_1}\cos(q_{l_0}\eta)\cos(q_{l_1}\eta)$ is always positive regardless of the interacting bands having slopes of the same or different signs. We will see in the subsequent sections that this feature of

[6] polaritons, for instance

the inter-band interaction, which results from the non-Hermitian nature of the matrix $A_l^{l'}$, is responsible for a rather unusual form of the dispersion laws describing hybridized bands.

7.4 Weak inter-band coupling

As an example of the band modification I consider dispersion curves emerging as a result of interaction between $29TM1$ and $25TM2$ supermodes. This choice is motivated by experiments of Ref.[5], where these dispersion curves have been measured. One can see from Fig.7.1 that the bands of these two supermodes slightly overlap.

However, considering $\mathrm{Re}\left[\cos\left(q_{29}\eta\right)\right]$ and $\mathrm{Re}\left[\cos\left(q_{25}\eta\right)\right]$ I find that the resonance between these two bands does not occur, thus, one should expect in this case just a modification of the dispersion laws without a significant reconstruction of the band structure.

Fig.7.2 presents the results obtained after first two iterations of numerical solutions of Eq.(7.22) for these two modes along with the respective initial bands. The second iteration takes into account all reservoir modes from $l = 1$ to $l = 40$. One can see that the effect of the reservoir modes is almost zero in the vicinity of the center of the band, but slightly increases toward the edges of the initial bands, which confirms my choice of significant and

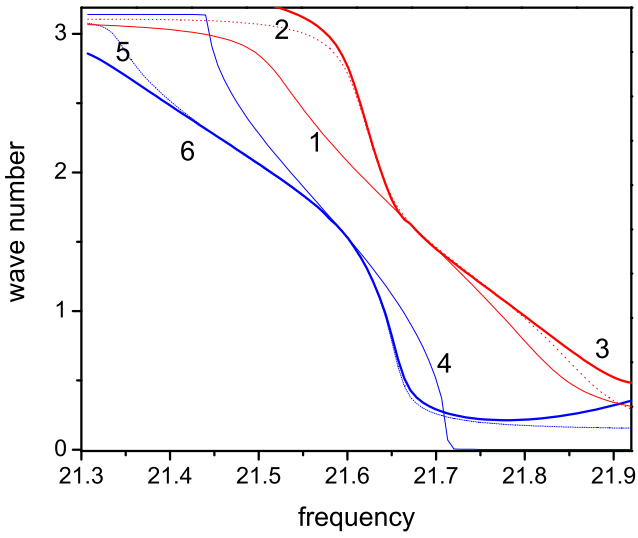

Figure 7.2: (Color on-line) Dispersion curves of $29TM1$ and $24TM2$ bands. Dash lines labeled 1 and 4 presents single-band dispersion curves, thin lines labeled 2 and 5 demonstrates dispersion curves found without reservoir modes taken into account, and finally thick lines labelled 3 and 6 show dispersion curves with reservoir modes included.

reservoir modes. However, outside of the allowed bands of the $29TM1$ and $TM24, 2$ modes designation of these modes as significant ones may no longer be valid because one can trespass to the allowed band of one or several of other modes, which I treated here as the bath. It is obvious that in those frequency regions the approximation used to obtain Fig.7.2 is no longer valid.

The shape of the modified curves can be easily understood on the basis of my general analysis of Eq.(7.22). As I explained above at $\tilde{q}_l\eta = \pi/2$ modified and initial dispersion laws coincide, but farther away from the center of the respective bands the modified dispersion laws are pushed away from the initial curves. The characteristic shape of the dispersion curves results from the fact that the corrections to the initial dispersion laws due to the inter-band coupling have different signs for $29TM1$ and $25TM2$ bands: its negative for the former and positive for the latter. The most strong modifications of both curves occur at the lower frequency boundaries of their respective bands. This modification can be described as a shift of the boundaries of the respective bands, which is more prominent for $29TM1$, whose initial band has much better defined boundaries because of the smaller decay. These boundaries are not very well defined for modified $29TM1$ band, however, which tells us about an increase in the radiative decay of this supermode caused by the admixture of $25TM2$ band. This increase, however, is not very

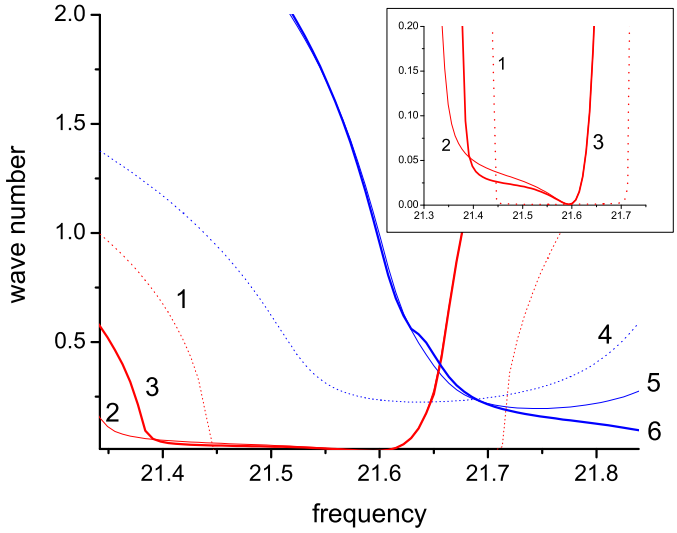

Figure 7.3: (Color on-line) Decay rates of $29TM1$ (1, 2 and 3) and $24TM2$ (4, 5, and 6) bands. The labelling of the curves is the same as in Fig.7.2. The insert shows, in a magnified form, the spectral region corresponding to 29TM1 mode. One can see a significant increase in the radiative decay rate of this mode in the vicinity of the new band boundaries, which, however, decreases to the initial WGM value at $x = x_{29,1}$

dramatic, and allows keeping the concept of allowed and forbidden bands as a convenient tool to characterize different spectral regions. The frequency dependence of the decay rates, characterized by $\mathrm{Im}\,\tilde{q}_l$ are shown in Fig.7.3, where the positions of the band boundaries characterized by an abrupt change in the decay rate are seen much clearer. Another interesting effect seen in this figure is that the frequency x_{29TM1} of the respective WGM is no longer at the center of the modified band. This is, obviously, caused by the shift of

the band boundaries, which for both low- and high-frequency edges occurs toward lower frequencies. This shift is also responsible for an asymmetry of the band, which manifests itself in the different growth of the decay rates toward left and right boundaries.

I estimate the shifts of the band boundaries for $29TM1$ and $25TM2$ supermodes if I neglect the renormalization of the coefficients $A_l^{l_1}$, and treat the inter-band interaction parameter $\Omega_{l_1 l_0}$ as a small perturbation. Then, employing the approximation for coefficients α_l given by Eq.(7.10), and neglecting the frequency dependence of the coupling coefficients one can find for new band boundaries, $\tilde{x}_b^{\pm}$, defined as frequencies at which $\mathrm{Re}[\cos(q_{\pm}\eta)] = 1$ the following expressions

$$\tilde{x}_{b_l}^{\pm} = x_{b_l}^{\pm} \mp \frac{\Omega_{l\nu}\kappa_{ls}}{1 \mp \cos\left[q_\nu\left(x_{b_l}^{\pm}\right)\eta\right]} \tag{7.24}$$

Index l in this equation refers to the band whose boundaries I am calculating, while the index ν signifies its interacting counterpart. Since $\Omega_{l\nu}$ is always positive, and κ_{ls} is negative for both participating modes, the sign of the correction is determined by the values of $\cos q$ of the ν-th band at the initial boundaries of the l-th band. Since its quite likely that these boundaries lie in the forbidden band of the ν-th band, the values of these cosines are not limited by unity. In the case of $29TM1$ supermode interacting with $25TM2$

I find that:

$$\cos\left[q_{25}(x^{+}_{29,1})\eta\right] \approx 0.18 \qquad \cos\left[q_{25}(x^{-}_{29,1})\eta\right] \approx -1.46$$

$$\cos\left[q_{29}(x^{+}_{25,2})\eta\right] \approx 2.53 \qquad \cos\left[q_{29}(x^{-}_{25,2})\eta\right] \approx -0.5174$$

These calculations show that the corrections to the upper and lower boundaries are both negative for $29TM1$ band, and both positive for $25TM2$ band in complete agreement with numerical calculations.

As it was mentioned I choose the supermodes $29TM1$ and $25TM2$ for illustration of my general results mostly because their dispersion curves were observed experimentally in Ref.[5]. However, before comparing the experimental results with my theory one should recall that the experiment in Ref.[5] was conducted in a resonance configuration, when q_l was fixed by the conditions of the experiment, and real and imaginary parts of frequency were measured via positions and widths of the respective resonances. This experimental setup is different from what was assumed in my theoretical analysis. Therefore, the comparison makes sense only away from the band boundaries, where decay rates are relatively small and the inverse of the experimentally observed quantity $x_l(q)$ is close to $q_l(x)$ studied here. Fig.7.4 demonstrates the curves $q_{29,1}(x)$ and $q_{25,2}(x)$ produced by digitizing Fig.2b from Ref.[5]. Comparing this figure with results of my calculations, Fig.7.2 one can see an

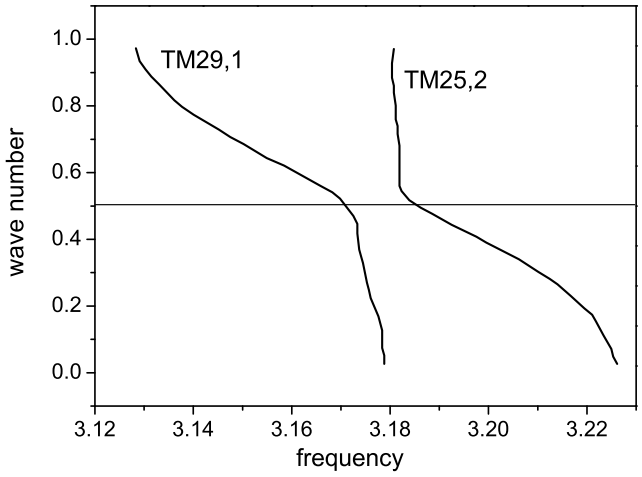

Figure 7.4: Experimental dispersion curves of $29TM1$ and $TM24,2$ bands obtained by digitizing one of the figures in Ref.[5].

excellent qualitative agreement between the theory and the experiment.

7.5 Strong inter-band coupling

In order to illustrate the effects of the strong inter-band coupling I consider the interaction between modes $39TE1$ and $34TE2$. The resonance condition (7.23) for these modes is fulfilled at frequency x_r, which is within allowed spectral region for both bands, albeit rather close to their respective band boundaries. Therefore, one should expect the manifestation of the strong coupling effects in this case. Another important feature distinguishing this pair of modes is the different parity of their angular momentum indexes.

As a result, the initial (single-band) dispersion curves of these supermodes are characterized in the vicinity of the resonance point by slopes of opposite signs. In the case of regular interacting modes such as phonon- or exciton-polaritons, one would expect in a situation like this a normal anti-crossing behavior resulting in the opening of the polariton band-gap in the spectrum of the system. This would have happened in the case considered here as well, if the interaction term in Eq.(7.22) were negative. It, however, is always positive as it was explained above and, therefore, no spectral gap arises. The shape of the dispersion curves emerging in this situation and shown in Fig.7.5 is rather unusual.

The parts of the initial dispersion curves located below the crossing point are pushed downward from it and connect in a continuous manner to form a new *hybrid band*. The remaining parts of the initial dispersion laws are pushed upward such that the wave numbers corresponding to the resultant second dispersion curve become complex valued in the entire spectral region under consideration, with its real part remaining equal to π for all considered frequencies. In other words, the spectral region covering initial $39TE1$ and $34TE2$ bands is a forbidden band for the second dispersion curve. Thus, the inter-band coupling turns two co-existing initial bands into a single hybrid band with rather unusual dispersion properties.

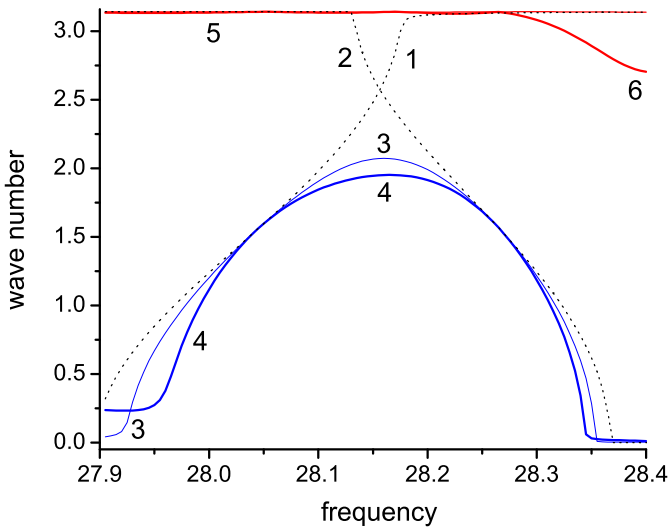

Figure 7.5: Dispersion laws describing hybridized bands arising as a result of interaction between $39TE1$ and $34TE2$ supermodes. Curves 1 and 2 represents initial unperturbed dispersion laws, 3 and 5 are dispersion curves obtained without accounting for interaction with reservoir modes, and curves 4 and 6 depict dispersion laws of two branches with reservoir modes taken into account. The upper branch is almost completely pushed to the forbidden region.

Instead of a spectral gap one has here a region of forbidden values of *wave numbers*, which extends from the maximum value of the wave number on the lower dispersion curve, q_{max}, all the way to the boundary of the Brillouin zone. This means that the states characterized by the wave numbers from the forbidden region cannot have a real valued frequency, i.e. do not correspond to stationary solutions of the respective dynamic equations. The new allowed hybrid band is a combination of the initial bands for the

two interacting supermodes and covers a spectral region previously occupied by $39TE1$ and $34TE2$. The shifts of the initial band boundaries (the low frequency boundary for $34TE2$ and higher frequency boundary for $39TE1$) can be estimated with the help of the same expression (7.24) that I obtained for the weak coupling case. This is possible because these band boundaries lie far away from the resonance point and I can use perturbation theory. Taking into account that the sign of parameters κ is now different for the two supermodes one finds that the the low frequency boundary of $34TE2$ shifts toward higher frequencies by approximately 0.025, while the higher frequency boundary of $39TE1$ supermode shifts toward lower frequencies by approximately 0.01. These numbers are in good agreement with numerical calculations shown in Fig.7.5. This figure also shows that taking into account the reservoir modes [7] does not change properties of the hybrid mode too much.

While the existence of the wave number gap is the general property of the dispersion equation (7.22) for the significant supermodes characterized by angular momentum index of different parity, the complete vanishing of the upper hybrid band is specific for the pairs of modes under consideration here. In order to understand the properties of these bands better one can estimate

[7] second iteration of my procedure

the distance between the lower and upper branches exactly at the resonance point neglecting the effects due to the reservoir modes. This distance, Σ, determines the position of the maximum q_{max} for the lower branch, and the minimum q_{min} for the upper branch. It is more convenient to work with $\cos q_{\pm}$ than with the wave numbers themselves, so I will define Σ via equation:

$$\begin{aligned} \cos(q_{max}\eta) &= \cos(q_r\eta) + \Sigma \\ \cos(q_{min}\eta) &= \cos(q_r\eta) - \Sigma \end{aligned} \tag{7.25}$$

The magnitude of Σ can be estimated from Eq.(7.22), which gives

$$\Sigma = \frac{\mathrm{Re}\left[\sqrt{4\Omega_{l_1 l_0} - \Gamma^2 - 4i\Omega_{l_1 l_0}\Gamma}\right]}{1 - \Omega_{l_1 l_0}} \tag{7.26}$$

Here I took into account that the resonance occurs close to the band boundaries, so that $\mathrm{Re}[\cos q_{l_0}] \approx \mathrm{Re}[\cos q_{l_1}] \approx -1$, and introduced $\Gamma = \mathrm{Im}[\cos q_{l_1}]$, which represents the supermode with the largest radiative decay [8]. However, the radiative decay of the $34TE2$ supermode is still so small that $\Gamma^2 \ll \Omega_{l_0 l_1}$ in this case, and Σ can be approximated as

$$\Sigma = \frac{2\sqrt{\Omega_{l_1 l_0}}}{1 - \Omega_{l_1 l_0}} \tag{7.27}$$

In the particular example of $39TE1$ and $34TE2$ bands the resonance occurs at a point, where $\cos q_r$ is so close to the boundary value of -1, that $\cos(q_{min}\eta)$ becomes less than -1 making the respective wave numbers for the entire

[8] $34TE2$ in the case under consideration

frequency region imaginary. Should the crossing point of the two interacting supermodes lie farther away from the band boundaries, the part of the upper hybrid band could also survive, but it would be restricted by the frequency region in the vicinity of the resonance frequency. The $\cos(q_{max}\eta)$ on the other hand is pushed farther away from the boundary, so that the entire lower band remains allowed, and the respective maximum allowed value of q can be estimated as $q_{max}\eta \approx q_r\eta - \sqrt{2\Sigma}$. Comparison of these estimates with numerical results shows that they give a relatively good approximation for the respective quantities in the case under consideration.

One of the consequences of having a gap for wave numbers, is that formally speaking, the group velocity of the excitation described by the hybrid dispersion law diverges at $q = q_{max}$. This form of a dispersion curve, therefore, raises a question if it is consistent with causality. This question was discussed in Ref.[74], where a similar form of the dispersion curve was found in an one-dimensional resonant photonic crystal. It was shown in that work that the wave-number gap and accompanying it infinite group velocity do not contradict causality, if attenuation of the respective excitation is properly accounted for. Similar anomalous behavior of the group velocity [9] has been known for a long time, for instance, in the case of exciton-polaritons

[9] without the wave number gap, of course

[75]. A more general statement that abnormal behavior of group velocity should be expected in the regions of resonant absorption in all dispersive dielectrics was proven in Ref.[76].

In spite of formal analogy between the anomalous dispersion law and the results of Ref.[74] these two situations significantly differ from each other. The wave number gap found in Ref.[74] is caused by the frequency dispersion of the respective dielectric medium, and coincides with regions of anomalous dispersion and resonant absorption. The origin of the gap in my case is completely different and can be traced to the combination of two factors: different signs of the slopes of the initial dispersion curves and positive value of the respective coupling constant. The latter is caused, as I already discussed, by a non-Hermitian nature of the matrix describing the inter-band coupling in the case under consideration. Accordingly, the decay rate of the photonic supermodes considered here does not show any resonant enhancement in the vicinity of the wave-number gap. I present the frequency dependence of this quantity, which remains surprisingly small in all frequency range corresponding to the allowed hybrid band, and demonstrates a weak non-monotonic dependence on frequency with a flat minimum (Fig.7.6).

I can explain this behavior qualitatively by reminding that at the centers of both initial bands the interaction between them vanishes, so the decay

rate at these two points coincides with the decay rates of the original WGM resonances. The crossing of the curves 2,3 and 4 in the insert in Fig.7.6 corresponds to the initial $34TE2$ WGM, and the second [10] minimum on curve 4 corresponds to x_{39TE1}. The first minimum on this curve appears only after the interaction with reservoir modes is taken into account and presents another peculiarity of the system under consideration. Normally, one would expect that the reservoir bands can only increase the radiative rate, while here we observe an opposite behavior. A possible qualitative explanation of this effect can be offered on the basis of the following arguments.

Let us assume, for an instance, that instead of considering the experimental situation, in which frequency is considered real and the wave number complex, I deal with the resonance type of experiment with real q and complex x. In this case it is reasonable to assume, and the results of Ref.[55] support this assumption, that the the reservoir modes would play its regular role and increase the width of the respective resonances, Δx. The transition from this description to the one used in this chapter, with complex valued q can then be approximately carried out with the help of the following expression: $\mathrm{Im}\, q \simeq (d\,\mathrm{Re}\, q/dx)\Delta x$. Thus, the frequency regions with flat dispersion curve should be characterized by decreasing imaginary part of the wave num-

[10] counting from the left

ber. In order to understand why this minimum appears only after reservoir bands are taken into account, one needs to compare respective dispersion curves.

From Fig.7.5 one can see that without the reservoir modes the maximum of the dispersion curve is relatively narrow. The reservoir modes make the maximum wider, which means that a broader frequency interval is characterized by small values of $d\,\mathrm{Re}\,q/dx$. This causes a faster decrease of the spatial decay rate when frequency shifts toward the allowed region for former $39TE1$ band, which can be seen in Fig.7.6. This tendency reverses for frequencies greater than x_r, when the group velocity starts decreasing. When, however, the frequency approaches x_{39TE1}, the decay rate decreases again resulting in a curve with two minima, one at x_r, and the other one at x_{39TE1}.

7.6 Conclusion

In this chapter I have developed a theory of the inter-band coupling in the system of dielectric spheres forming a one-dimensional chain. My objective was to obtain analytical expressions allowing one to study band structure and dispersion properties of the collective excitations of this system with inter-band mixing effects taken into account. I developed an approximation scheme generalizing an approach of Ref.[55], which was originally applied to the case

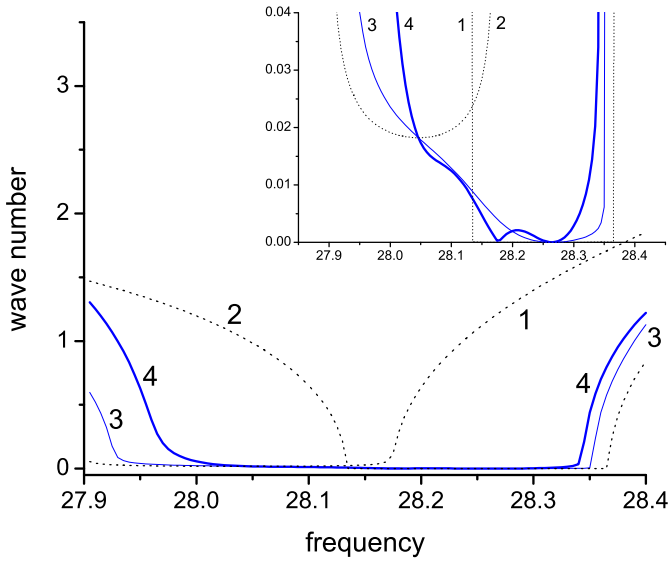

Figure 7.6: Radiative decay rates for the allowed hybridized band. The labeling of the lines is the same as in Fig.7.5. The insert magnifies the region around the center of $39TE1$ band.

of two coupled spheres and derived a general dispersion equation describing the band structure emerging as a result of the inter-band interaction. I showed that there might exist three qualitatively distinct regimes of such coupling depending upon the properties of the initial single-band dispersion curves of the interacting *supermodes*, and the strength of the interaction. My general results were applied to two particular examples illustrating two of the possible manifestations of the inter-mode coupling.

As an illustration of the regime of weak band modification I considered frequency region corresponding to initial supermodes $TE29,1$ and $25TM2$, whose initial dispersion curves do not cross each other. Nevertheless, I showed that the inter-band coupling significantly modifies the dispersion curves of these supermodes and is responsible for their characteristic shape observed in experiments of Ref.[5]. What is interesting in this example is that the modification of the dispersion laws mimics the anti-crossing behavior typical for resonantly interacting excitations. At the same time, as it was mentioned above no crossing resonance takes place in this case. I explained the shape of these curves as a result of two effects. First, I showed that the position of frequency corresponding to the center of the band, where wave number $q = \pi/(2\eta)$, where η is dimensionless period of the structure, is pinned to the frequency of the parent WGM mode corresponding to a

given band. Second, I demonstrated that the inter-band coupling shifts the boundary of the respective bands in the opposite directions. As a result, one of the dispersion curves bends upward, while the other one bends downward imitating the anti-crossing behavior. The results of the numerical calculations of these dispersion curves show very good qualitative agreement with experimental results of Ref.[5].

More interesting situation was found, however, in the spectral region corresponding to supermodes $39TE1$ and $34TE2$. These modes exhibit true crossing resonance very close to the boundaries of the both bands. It is also important that in the vicinity of the crossing point their initial dispersion curves have slopes of opposite signs. The interaction between these supermodes gives rise to a new hybrid band with a highly unusual dispersion characteristics. Instead of a standard avoiding crossing kind of behavior accompanied by opening of a gap in the frequency spectrum of the system, I found a gap in the allowed values of the *wave numbers*. More specifically, instead of two initial crossing dispersion curves, there emerges one curve characterized by a non-monotonic dependence of the wave number of frequency. The maximum value of the wave number is significantly lower than π/η, which determines traditional band boundaries. Thus, there is a range of wave numbers that do not correspond to excitations with any real val-

ued frequency. Such a band structure is not related to the presence of the radiative decay, which remains very small throughout the entire band of frequencies corresponding to this hybrid band. I traced the origin of this effect to the non-Hermitian nature of the inter-band coupling typical for electromagnetic problems. The phenomenon of the wave number band-gap could be observed experimentally in an experiment similar to one carried out in Ref.[5]. In that experiment the fluorescent spectra were observed for chains with varying number of spheres. In normal situation, adding a sphere results in appearance of an additional peak on the spectrum so that each peak can be identified with a respective wave number. The wave number gap would manifest itself in this experiment as a failure of a new peak to appear after addition of a sphere to the chain. The dependence of the fluorescence spectrum upon the number of spheres in this situation is a non-trivial problem requiring a separate consideration. Other possible experimental manifestations of the predicted band structure may include unusual behavior of a pulse propagating along the chain, and angular dependence of the radiation emitted by the chain. More detailed analysis of these effects is also outside of the scope of this paper and will be carried out in the future.

Bibliography

[1] V. Agranovich, D. Basko, G. L. Rocca, and F. Bassani. Excitons and optical nonlinearities in hybrid organicinorganic nanostructures. *J. Phys.: Condens. Matter*, 13(10):9369–9400, 1998.

[2] A. Engelmann, V. I. Yudson, and P. Reineker. Enhanced optical nonlinearity of hybrid excitons in an inorganic semiconducting quantum dot covered by an organic layer. *Phys. Rev. B*, 57(3):1784–1790, Jan 1998.

[3] Nguyen Que Huong and Joseph L. Birman. Quantum dot lattice embedded in an organic medium: Hybrid exciton state and optical response. *Physical Review B*, 61(19):13131, 2000.

[4] C. Madigan and V. Bulovic. Solid state solvation in amorphos organic thin films. *Physical review letters*, 91(24):247403, 2003.

[5] Y. Hara, T. Mukaiyama, K. Takeda, and M. Kuwata-Gonokami. Heavy Photon States in Photonic Chains of Resonantly Coupled Cavities with Supermonodispersive Microspheres. *Physical Review Letters*, 94(20):203905, 2005.

[6] F. Bassani, G. L. Rocca, D. Basko, and V. Agranovich. Excitons in hybrid organic-inorganic nanostructures. *Fizika tverdogo tela*, 41(5):778–780, 1999.

[7] V. Bulovic, R. Deshpande, ME Thompson, and SR Forrest. Tuning the color emission of thin film molecular organic light emitting devices by the solid state solvation effect. *Chemical Physics Letters*, 308(3):317–322, 1999.

[8] D. Frohlich, G. Dasbach, G. B. Hogersthal, M. Bayer, R. Kliebera, D. Sutera, and H. Stolzb. High resolution spectroscopy of yellow 1s excitons in cu2o. *Solid State Communications*, 134:139–142, 2005.

[9] R. J. Elliott. Symmetry of excitons in cu_2o. *Phys. Rev.*, 124(2):340–345, Oct 1961.

[10] E. F. Gross and N. A. Karryev. Light absorption by cuprous oxide crystal in infrared and visible spectrum. *Dokl. Akad. Nauk SSSR*, 84:261, 1952.

[11] G. Kavoulakis, Y. C. Chang, and G. Baym. Fine structure of excitons in cuprous oxide. *Phys. Rev. B*, 55(12):7593, 1997.

[12] S. A. Moskalenko and K. Tolpigo. *Zh. Eksp. Teor. Fiz.*, 36:149, 1959.

[13] H. R. Trebin, H. Z. Cummins, and J. L. Birman. Excitons in cuprous oxide under uniaxial stress. *Physical Review B*, 23(2):597, 1981.

[14] S. Jaziri. Effects of electric and magnetic fields on excitons in quantum dots. *Solid state communications*, 91(2):171–175, 1994.

[15] M. Baldo, Z. Soos, and S. Forrest. Excitons in cuprous oxide under uniaxial stress. *Chem. Phys. Lett.*, 347(2):297, 2001.

[16] L. Onsager. *J. Am. Chem. Soc.*, 58:1486, 1936.

[17] G. Bastard. *Wave mechanics Applied to Semiconductor Heterostructures*. Halsted Press New York, 1988.

[18] J.D. Jackson. *Classical Electrodynamics*. John Willey, Inc., 1975.

[19] S. A. Moskalenko and M. A. Liberman. Propagation hanle effect of quadrupole polaritons in cu2o. *Phys. Rev. B*, 65:064303, 2002.

[20] Y. Liu and D. Snoke. Resonant two-photon excitation of 1s paraexcitons in cuprous oxide. *Solid State Communications*, 134(1-2):159–164, 2005.

[21] G. M. Kavoulakis. Bose-einstein condensation of excitons in cuprous oxide. *Phys. Rev. B*, 65:035204, 2001.

[22] A.L. Ivanov and S.G. Tikhodeev. *Problems of Condensed Matter Physics*. Clarendon press, Oxford, in press 2007.

[23] VM Agranovich and G.F. Bassani. *Electronic Excitations in Organic Based Nanostructures*. Elsevier, 2003.

[24] O. Roslyak and J.L. Birman. Hybridized quadrupole-dipole exciton effects in cuprous oxide / organic heterostructure. *Physical Review B (to be published), arXiv:cond-mat/0703268*, 2006.

[25] O. Roslyak and J.L. Birman. Polaritons in cuprous oxide perturbed by la-phonons. *Physical Review B (to be published), arXiv:cond-mat/0703650*, 2007.

[26] G. Dasbach, G.B.H. von Högersthal, D. Fröhlich, H. Stolz, and M. Bayer. Bistability in the transmission of Cu_ {2} O: Optical hysteresis in the high-resolution limit. *Physical Review B*, 70(12):121202, 2004.

[27] R. Pässler. Temperature dependence of exciton peak energies in multiple quantum wells. *Journal of Applied Physics*, 83:3356, 1998.

[28] G. Weiser. Stark effect of one-dimensional wannier excitons in polydiacetylene single crystals. *Phys. Rev. B*, 45(24):14076–14085, Jun 1992.

[29] YP VARSHNI. TEMPERATURE DEPENDENCE OF THE ENERGY GAP IN SEMICONDUCTORS. *PHYSICA*, 34(1):149–154, 1967.

[30] M. Y. Shen, S. Koyama, M. Saito, T. Goto, and N. Kuroda. Second-harmonic generation resonant to the 1s orthoexciton level of cuprous oxide. *Phys. Rev. B*, 53(20):13477–13481, May 1996.

[31] S. Mukamel. *Principles of nonlinear optical spectroscopy*. Oxford University Press, New York, 1995.

[32] D. W. Snoke, J. P. Wolfe, and A. Mysyrowicz. Evidence for bose-einstein condensation of a two-component exciton gas. *Phys. Rev. Lett.*, 64(21):2543–2546, May 1990.

[33] R. Atanasov, F. Bassani, and V. M. Agranovich. Second-order nonlinear optical susceptibility of asymmetric quantum wells. *Phys. Rev. B*, 50(11):7809–7819, Sep 1994.

[34] Y. Gao, NQ Huong, JL Birman, and MJ Potasek. Large nonlinear optical properties of semiconductor quantum dot arrays embedded in an organic medium. *Journal of Applied Physics*, 96:4839, 2004.

[35] Nguyen Que Huong and Joseph L. Birman. Hybrid exciton state in a quantum dot˘dendrite system: Green functions. *Phys. Rev. B*, 67(7):075313, Feb 2003.

[36] N. Bloembergen. *Nonlinear optics*. Benjamin, New York, 1965.

[37] M. Artoni, I. Carusotto, G.C. La Rocca, and F. Bassani. *J. Opt. B.: Quantum Semiclass. Opt.*, 4:S345–S350, 2002.

[38] C. Madigan and V. Bulovic. Exciton physics in organic optoelectronics. Bringing Materials Research Together, 2004.

[39] H. Kishida, T. Hasegawa, Y. Iwasa, T. Koda, Y. Tokura, H. Tachibana, M. Matsumoto, S. Wada, T. T. Lay, and H. Tashiro. Electric-field-induced second-harmonic generation mediated by one-dimensional excitons in polysilanes. *Phys. Rev. B*, 50(11):7786–7792, Sep 1994.

[40] D. C. Haueisen and H. Mahr. Resonant second-harmonic generation in the exciton region of cucl and zno. *Phys. Rev. B*, 8(2):734–745, Jul 1973.

[41] D. W. Snoke, A. J. Shields, and M. Cardona. Phonon-absorption recombination luminescence of room-temperature excitons in cu_2o. *Phys. Rev. B*, 45(20):11693–11697, May 1992.

[42] C. Ell, A. L. Ivanov, and H. Haug. Relaxation kinetics of a low-density exciton gas in cu_2o. *Phys. Rev. B*, 57(16):9663–9673, Apr 1998.

[43] David W. Snoke and S. A. Moskalenko. *Bose-Einstein Condensation of Excitons and Biexcitons: And Coherent Nonlinear Optics with Excitons*. Cambridge University Press, Science, 2000.

[44] M. Inguscio, S. Stringari, and CE Wieman. *Bose-Einstein Condensation in Atomic Gases:: Course CXL: Varenna on Lake Come Villa Monestero, 07-17 July 1998*. IOS Press, 1999.

[45] G. M. Kavoulakis, Gordon Baym, and J. P. Wolfe. Quantum saturation and condensation of excitons in cu_2o: A theoretical study. *Phys. Rev. B*, 53(11):7227–7243, Mar 1996.

[46] A. Mysyrowicz, D. Hulin, and A. Antonetti. Long exciton lifetime in cu_2o. *Phys. Rev. Lett.*, 43(15):1123–1126, Oct 1979.

[47] Bing Shen Wang and Joseph L. Birman. Theory of phonoritons and experiments to determine phonoriton dispersion and spectrum. *Phys. Rev. B*, 42(15):9609–9621, Nov 1990.

[48] L. Hanke, D. Fröhlich, A. L. Ivanov, P. B. Littlewood, and H. Stolz. La phonoritons in cu_2o. *Phys. Rev. Lett.*, 83(21):4365–4368, Nov 1999.

[49] A. L. Ivanov and L. V. Keldysh. *Zh. Eksp. Teor. Fiz.*, 84:404, 1982.

[50] L.V. Keldysh and S.G. Tikhodeev. *Zh. Eksp. Teor. Fiz.*, 63:1086, 1986.

[51] K. Kapinska, P.V. Loosdrechta, I. Handayania, and A. Revcolevschi. Para excitons in cu2oa new approach. *Journal of Luminescence*, 112:17–20, 2005.

[52] J. Fernandez-Rossier, C. Tejedor, L. Munoz, and L. Vina. Polarized interacting exciton gas in quantum wells and bulk semiconductors. *arXiv: cond-mat./*, 1:9510138.

[53] C. Ell, A. L. Ivanov, and H. Haug. Relaxation kinetics of a low-density exciton gas in cuprous oxide. *Phys. Rev. B*, 57(16):9663, 1998.

[54] J. Kasprzak, M. Richard, S. Kundermann, A. Baas, P. Jeambrun, JM Keeling, FM Marchetti, MH Szymanska, R. Andre, JL Staehli, et al. Bose-Einstein condensation of exciton polaritons. *Nature*, 443(7110):409–14, 2006.

[55] H. Miyazaki and Y. Jimba. Ab initio tight-binding description of morphology-dependent resonance in a bisphere. *Phys. Rev. B*, 62(12):7976–7997, Sep 2000.

[56] C.F. Bohren and D.R. Huffman. *Absorption and scattering of light by small particles*. Wiley New York, 1983.

[57] S. Stein. *Q. appl. Math*, 19:15, 1961.

[58] K.A. Fuller. Optical resonances and two-sphere systems. *Appl. Opt*, 30:4716–4731, 1991.

[59] LI Deych and A. Roslyak. Photonic band mixing in linear chains of optically coupled microspheres. *Physical Review E*, 73(3):36606, 2006.

[60] E. Peter, P. Senellart, D. Martrou, A. Lemaître, J. Hours, JM Gérard, and J. Bloch. Exciton-Photon Strong-Coupling Regime for a Single Quantum Dot Embedded in a Microcavity. *Physical Review Letters*, 95(6):67401, 2005.

[61] X. Fan, S. Lacey, and H. Wang. Microcavities combining a semiconductor with a fused-silica microsphere. *Opt. Lett*, 24:771–773, 1999.

[62] D.B. Mitzi, K. Chondroudis, and C.R. Kagan. Design, Structure, and Optical Properties of Organic–Inorganic Perovskites Containing an Oligothiophene Chromophore. *Inorg. Chem*, 38(26):6246–6256, 1999.

[63] A. Yariv, Y. Xu, R.K. Lee, and A. Scherer. Coupled-resonator optical waveguide: a proposal and analysis. *Opt. Lett*, 24(11):711–713, 1999.

[64] S. Mookherjea and A. Yariv. IEEE J. Select. Top. *Quantum Electron*, 8:448, 2002.

[65] R.K. Chang, A.J. Campillo, et al. *Optical processes in microcavities*. World Scientific, 1996.

[66] S. Arnold, A. Ghaemi, P. Hendrie, and KA Fuller. Morphological resonances detected from a cluster of two microspheres. *Opt. Lett*, 19:156–158, 1994.

[67] T. Mukaiyama, K. Takeda, H. Miyazaki, Y. Jimba, and M. Kuwata-Gonokami. Tight-Binding Photonic Molecule Modes of Resonant Bispheres. *Physical Review Letters*, 82(23):4623–4626, 1999.

[68] YP Rakovich, JF Donegan, M. Gerlach, AL Bradley, TM Connolly, JJ Boland, N. Gaponik, and A. Rogach. Fine structure of coupled optical modes in photonic molecules. *Physical Review A*, 70(5):51801, 2004.

[69] B.M. Möller, U. Woggon, and M.V. Artemyev. Coupled-resonator optical waveguides doped with nanocrystals. *Optics Letters*, 30(16):2116–2118, 2005.

[70] VN Astratov. Optical coupling and transport phenomena in chains of spherical dielectric microresonators with size disorder. *Applied Physics Letters*, 85(23):5508, 2004.

[71] E. Lidorikis, MM Sigalas, EN Economou, and CM Soukoulis. Tight-Binding Parametrization for Photonic Band Gap Materials. *Physical Review Letters*, 81(7):1405–1408, 1998.

[72] W.A. Harrison. *Elementary Electronic Structure*. World Scientific, 2004.

[73] A. Moroz. Density-of-states calculations and multiple-scattering theory for photons. *Physical Review B*, 51(4):2068–2081, 1995.

[74] O. Toader and S. John. Photonic band gap enhancement in frequency-dependent dielectrics. *Physical Review E*, 70(4):46605, 2004.

[75] A. Puri and J.L. Birman. Energy-Transport, Group, and Signal Velocities near Resonance in Spatially Dispersive Media. *Physical Review Letters*, 47(3):173–177, 1981.

[76] E.L. Bolda, R.Y. Chiao, and J.C. Garrison. Two theorems for the group velocity in dispersive media. *Physical Review A*, 48(5):3890–3894, 1993.